

# Development of Computed Tomography Algorithms

Guest Editors: Hengyong Yu, Patrick J. La Riviere, and Xiangyang Tang



International Journal of Biomedical Imaging

---

# **Development of Computed Tomography Algorithms**

## **Development of Computed Tomography Algorithms**

Guest Editors: Hengyong Yu, Patrick J. La Riviere,  
and Xiangyang Tang



---

Copyright © 2006 Hindawi Publishing Corporation. All rights reserved.

This is a special issue published in volume 2006 of “International Journal of Biomedical Imaging.” All articles are open access articles distributed under the Creative Commons Attribution License, which permits unrestricted use, distribution, and reproduction in any medium, provided the original work is properly cited.

## Editor-in-Chief

Ge Wang, Virginia Polytechnic Institute and State University, USA

## Associate Editors

Haim Azhari, Israel  
Kyongtae Bae, USA  
Richard Bayford, UK  
Freek Beekman, The Netherlands  
Subhasis Chaudhuri, India  
Jyh-Cheng Chen, Taiwan  
Anne Clough, USA  
Carl Crawford, USA  
Min Gu, Australia  
Eric Hoffman, USA  
Jiang Hsieh, USA

Ming Jiang, China  
Marc Kachelrieß, Germany  
Seung Wook Lee, South Korea  
Alfred Karl Louis, Germany  
Erik Meijering, The Netherlands  
Vasilis Ntziachristos, USA  
Scott Pohlman, USA  
Erik Ritman, USA  
Jay Rubinstein, USA  
Pete Santago, USA  
Lizhi Sun, USA

Jie Tian, China  
Michael Vannier, USA  
Yue Wang, USA  
Guowei Wei, USA  
David L. Wilson, USA  
Sun Guk Yu, South Korea  
Habib Zaidi, Switzerland  
Yantian Zhang, USA  
Yibin Zheng, USA  
Tiange Zhuang, China

# Contents

**Development of Computed Tomography Algorithms**, Hengyong Yu, Patrick J. La Rivière, and Xiangyang Tang  
Volume 2006 (2006), Article ID 39397, 3 pages

**Parallel Implementation of Katsevich's FBP Algorithm**, Jiansheng Yang, Xiaohu Guo, Qiang Kong, Tie Zhou, and Ming Jiang  
Volume 2006 (2006), Article ID 17463, 8 pages

**Local ROI Reconstruction via Generalized FBP and BPF Algorithms along More Flexible Curves**, Hengyong Yu, Yangbo Ye, Shiyong Zhao, and Ge Wang  
Volume 2006 (2006), Article ID 14989, 7 pages

**An Approximate Cone Beam Reconstruction Algorithm for Gantry-Tilted CT Using Tangential Filtering**, Ming Yan, Cishen Zhang, and Hongzhu Liang  
Volume 2006 (2006), Article ID 29370, 8 pages

**FDK Half-Scan with a Heuristic Weighting Scheme on a Flat Panel Detector-Based Cone Beam CT (FDKHSCW)**, Dong Yang and Ruola Ning  
Volume 2006 (2006), Article ID 83983, 8 pages

**Analysis of Cone-Beam Artifacts in off-Centered Circular CT for Four Reconstruction Methods**, S. Valton, F. Peyrin, and D. Sappey-Marinié  
Volume 2006 (2006), Article ID 80421, 8 pages

**Extending Three-Dimensional Weighted Cone Beam Filtered Backprojection (CB-FBP) Algorithm for Image Reconstruction in Volumetric CT at Low Helical Pitches**, Xiangyang Tang, Jiang Hsieh, Roy A. Nilsen, and Scott M. McOlash  
Volume 2006 (2006), Article ID 45942, 8 pages

**Comparison of Lesion Detection and Quantification in MAP Reconstruction with Gaussian and Non-Gaussian Priors**, Jinyi Qi  
Volume 2006 (2006), Article ID 87567, 10 pages

**Comparison of Quadratic- and Median-Based Roughness Penalties for Penalized-Likelihood Sinogram Restoration in Computed Tomography**, Patrick J. La Rivière, Junguo Bian, and Phillip A. Vargas  
Volume 2006 (2006), Article ID 41380, 7 pages

**A Prospective Study on Algorithms Adapted to the Spatial Frequency in Tomography**, Vincent Israel-Jost, Philippe Choquet, and André Constantinesco  
Volume 2006 (2006), Article ID 34043, 6 pages

**Assessment of Left Ventricular Function in Cardiac MSCT Imaging by a 4D Hierarchical Surface-Volume Matching Process**, Mireille Garreau, Antoine Simon, Dominique Boulmier, Jean-Louis Coatrieux, and Hervé Le Breton  
Volume 2006 (2006), Article ID 37607, 10 pages

## Editorial

# Development of Computed Tomography Algorithms

Hengyong Yu,<sup>1</sup> Patrick J. La Rivière,<sup>2</sup> and Xiangyang Tang<sup>3</sup>

<sup>1</sup>Department of Radiology, University of Iowa, Iowa City, IA 52242, USA

<sup>2</sup>Department of Radiology, University of Chicago, Chicago, IL 60637, USA

<sup>3</sup>Applied Science Laboratory, GE Healthcare, Waukesha, WI 53188, USA

Received 31 May 2006; Accepted 31 May 2006

Copyright © 2006 Hengyong Yu et al. This is an open access article distributed under the Creative Commons Attribution License, which permits unrestricted use, distribution, and reproduction in any medium, provided the original work is properly cited.

Over the past several years, computed tomography (CT) methods have advanced significantly, yielding novel analytic and iterative solutions applicable to medical CT and micro-CT. The resulting algorithms promise to improve spatial, contrast, or temporal resolution as well as to suppress artifacts and reduce radiation dose. Significant attention has been devoted to optimizing computational performance and to balancing conflicting requirements. Both theoretically oriented and application-specific issues are also being addressed. As a snapshot of the dynamically changing field of CT, this special issue includes 10 high-quality original papers.

Because spiral cone-beam CT can be used for rapid volumetric imaging with high longitudinal resolution, the development of exact and efficient algorithms for image reconstruction from spiral cone-beam projection data has been a subject of active research in recent years. Katsevich's filtered backprojection (FBP) formula represents a significant breakthrough in this field [1]. In this special issue, Yang et al. propose a parallel implementation of Katsevich's FBP formula [2] by the one-beam cover method, in which the backprojection procedure is independently driven by cone-beam projections. Based on Katsevich's work, generalized backprojection filtration (BPF) and FBP algorithms are developed to reconstruct images from data collected along more flexible scanning trajectories [3]. Using these recently developed algorithms, Yu et al. propose a local region reconstruction scheme [4]. The principal idea is to deliver a normal radiation dose to a local region of interest (ROI) that may contain a lesion while applying a very low radiation dose to the structures outside the ROI. Both the FBP and BPF algorithms can produce excellent results with a minimal increment to the dose needed for purely local CT.

Despite important advancements in the development of exact cone-beam reconstruction, approximate algorithms remain practically and theoretically valuable. Feldkamp et al.

heuristically adapted the fan-beam FBP algorithm for approximate cone-beam reconstruction in the case of a circular scanning locus [5]. This formulation, called the FDK algorithm, is more desirable in many cases than exact cone-beam reconstruction approaches in terms of several aspects of image quality and computational implementation. Since then, many efforts have been made to extend the FDK algorithm to other scanning configurations, leading to a series of FDK-like algorithms. In this special issue, Yan et al. propose an approximate FDK-like reconstruction algorithm for tilted-gantry CT imaging [6]. The method improves the image reconstruction by filtering the projection data along a direction that is determined by CT parameters and the tilted-gantry angle. Based on the idea that there is less redundancy for the projection data away from the central scanning plane, Yang and Ning develop a heuristic cone-beam geometric dependent weighting scheme [7], which leads to a new FDK-like half-scan algorithm. For correcting cone-beam artifacts in off-centered geometry, Valton et al. compare and evaluate four different reconstruction methods [8], which are the Alpha-FDK algorithm, a shift-invariant FBP method derived from the T-FDK, an FBP method based on the Grangeat formula, and an iterative algebraic method. Tang et al. extend the 3D weighted helical CB-FBP algorithm to handle helical pitches that are lower than 1 : 1 [9]. For helical over-scan, the extended 3D weighted helical CB-FBP algorithm can significantly improve noise characteristics or dose efficiency compared to the original algorithm, while other advantages of the original algorithm, such as reconstruction accuracy and computational efficiency, can be maintained.

In addition to the exact and approximate CBCT algorithms, iterative algorithms are important technologies in medical X-ray CT. It is well known that a major weakness of the noniterative algorithms, either exact or approximate, is that projection data are implicitly assumed to be

noise-free. However, noise is an inherent aspect of projection data, especially for low-dose scans. Iterative algorithms are well suited to deal with image artifacts caused by photon noise or other physical effects. Qi compares maximum a posteriori (MAP) reconstructions with Gaussian and non-Gaussian priors [10]. After evaluating three representative priors: the Gaussian prior, the Huber prior, and the Geman-McClure prior, Qi concludes that the Gaussian prior is as effective as the more complex non-Gaussian priors for lesion detection and quantification tasks. Rather than performing full-blown iterative reconstruction involving projecting and reprojecting the image, La Riviere et al. explore iterative approaches to sinogram restoration followed by analytic reconstruction. Here they compare the use of quadratic- and median-based roughness penalties [11], and they find that the two approaches produce similar resolution-variance tradeoffs to each other, which suggests that the particular choice of penalty may be less important than the decision to use a penalty at all. Israel-Jost et al. propose build frequency-adapted (FA) algorithms based on a condition of incomplete backprojection [12], leading to an FA-simultaneous algebraic reconstruction technique (FA-SART) algorithm. The results obtained with the FA-SART algorithm on a highly detailed phantom demonstrate a very fast convergence compared to the original SART algorithm.

The recent advances in X-ray technology provide high-contrast and spatiotemporal resolution, which offer new potential for evaluation of cardiac kinetics with 4D dynamic sequences. In this special issue, Garreau et al. propose a new method for cardiac motion extraction in multislice CT based on a 4D hierarchical surface-volume matching process [13]. Their aim is to detect the left heart cavities along the acquired sequence and estimate their 3D surface velocity fields. A Markov random field model is defined to find, according to topological descriptors, the best correspondences between a 3D mesh describing the left endocardium at one time-point and the 3D acquired volume at the following time-point. The global optimization of the correspondences is realized with a multiresolution process.

In closing this introduction to the special issue, we would like to express our appreciation to all the authors and reviewers for the tremendous efforts that have made the timely completion of our assignment successful and pleasant. Hope this special issue would attract a major attention of the peers and inspire more creative research ideas in the CT field.

Hengyong Yu  
Patrick J. La Riviere  
Xiangyang Tang

## REFERENCES

- [1] A. Katsevich, "An improved exact filtered backprojection algorithm for spiral computed tomography," *Advances in Applied Mathematics*, vol. 32, no. 4, pp. 681–697, 2004.
- [2] J. Yang, X. Guo, Q. Kong, T. Zhou, and M. Jiang, "Parallel implementation of the Katsevich's FBP algorithm," *International Journal of Biomedical Imaging*, vol. 2006, Article ID 17463, pp. 8 pages, 2006.
- [3] S. Zhao, H. Yu, and G. Wang, "A unified framework for exact cone-beam reconstruction formulas," *Medical Physics*, vol. 32, no. 6, pp. 1712–1721, 2005.
- [4] H. Yu, Y. Ye, S. Zhao, and G. Wang, "Local ROI reconstruction via generalized FBP and BPF algorithms along more flexible curves," *International Journal of Biomedical Imaging*, vol. 2006, Article ID 14989, pp. 7 pages, 2006.
- [5] L. A. Feldkamp, L. C. Davis, and J. W. Kress, "Practical cone-beam algorithm," *Journal of the Optical Society of America A*, vol. 1, no. 6, pp. 612–619, 1984.
- [6] M. Yan, C. Zhang, and H. Liang, "An approximate cone beam reconstruction algorithm for gantry-tilted CT using tangential filtering," *International Journal of Biomedical Imaging*, vol. 2006, Article ID 29370, pp. 8 pages, 2006.
- [7] D. Yang and R. Ning, "FDK half-scan with a heuristic weighting scheme on a flat panel detector-based cone beam CT (FD-KHSCW)," to appear in *International Journal of Biomedical Imaging*.
- [8] X. Tang, J. Hsieh, R. A. Nilsen, and S. M. McOlash, "Analysis of cone beam artifacts in off-centered circular CT for four reconstruction methods," to appear in *International Journal of Biomedical Imaging*.
- [9] S. M. McOlash, R. A. Nilsen, J. Hsieh, and X. Tang, "Extending three-dimensional weighted cone beam filtered backprojection (CB-FBP) algorithm for image reconstruction in volumetric CT at low helical pitches," to appear in *International Journal of Biomedical Imaging*.
- [10] J. Qi, "Comparison of lesion detection and quantification in MAP reconstruction with Gaussian and non-Gaussian priors," *International Journal of Biomedical Imaging*, vol. 2006, Article ID 87567, pp. 10 pages, 2006.
- [11] P. J. La Riviere, J. Bian, and P. A. Vargas, "Comparison of quadratic- and median-based roughness penalties for penalized-likelihood sinogram restoration in computed tomography," *International Journal of Biomedical Imaging*, vol. 2006, Article ID 41380, pp. 7 pages, 2006.
- [12] V. Israel-Jost, P. Choquet, and A. Constantinesco, "A prospective study on algorithms adapted to the spatial frequency in tomography," *International Journal of Biomedical Imaging*, vol. 2006, Article ID 34043, pp. 6 pages, 2006.
- [13] M. Garreau, A. Simon, D. Boulmier, J.-L. Coatrieux, and H. Le Breton, "Assessment of left ventricular function in cardiac MSCT imaging by a 4D hierarchical surface-volume matching process," *International Journal of Biomedical Imaging*, vol. 2006, Article ID 37607, pp. 10 pages, 2006.

**Hengyong Yu** received his B.S. degree in information science and technology and Ph.D. degree in information and communication engineering from Xi'an Jiaotong University, Xi'an, Shaanxi, China, in July 1998 and June 2003, respectively. He was an Instructor and Associate Professor with the College of Communication Engineering, Hangzhou Dianzi University, Hangzhou, Zhejiang, China, from July 2003 to September 2004. Currently, he is an Associate Research Scientist, Associate Director of the CT/Micro-CT lab, Department of Radiology, University of Iowa, Iowa City, USA. His interests include computed tomography and medical image processing. He has authored or coauthored more than 30 peer-reviewed papers. He is a Senior Member



of the IEEE. He was honored for an outstanding doctoral dissertation by Xi'an Jiaotong University, and received the First Prize for a Best Natural Science Paper from the Association of Sci. & Tech. of Zhejiang Province.

**Patrick J. La Riviere** received the A.B. degree in physics from Harvard University in 1994 and the Ph.D. degree from the Graduate Programs in Medical Physics in the Department of Radiology at the University of Chicago in 2000. In between, he studied the history and philosophy of physics while on the Lionel de Jersey-Harvard Scholarship to Cambridge University. He is currently an Assistant Professor in the Department of



Radiology at the University of Chicago, where his research interests include tomographic reconstruction in computed tomography, X-ray fluorescence computed tomography, and optoacoustic tomography.

**Xiangyang Tang** is currently with the Applied Science Laboratory of GE Healthcare Technologies as a Senior Scientist. With a focus on the development of image reconstruction algorithms for cone beam (CB) volumetric computed tomography (VCT) in diagnostic imaging, he has been working in the field of CB-VCT for almost 10 years, covering system analysis and design, development of algorithms for system cali-



bration, artifacts suppression, digital image/video processing, and CT cardiac imaging applications. In the recent 5 years, as an active Researcher in the field of medical imaging, he published more than 50 papers or book chapters in scientific journals and conference proceedings, and filed more than 10 US patent applications. Meanwhile, he also served as Guest Editor or Reviewer for a number of prestigious scientific journals in the field of medical imaging.

# Parallel Implementation of Katsevich's FBP Algorithm

Jiansheng Yang, Xiaohu Guo, Qiang Kong, Tie Zhou, and Ming Jiang

*LMAM, School of Mathematical Sciences, Peking University, Beijing 100871, China*

Received 30 September 2005; Revised 17 January 2006; Accepted 17 February 2006

For spiral cone-beam CT, parallel computing is an effective approach to resolving the problem of heavy computation burden. It is well known that the major computation time is spent in the backprojection step for either filtered-backprojection (FBP) or backprojected-filtration (BPF) algorithms. By the cone-beam cover method [1], the backprojection procedure is driven by cone-beam projections, and every cone-beam projection can be backprojected independently. Basing on this fact, we develop a parallel implementation of Katsevich's FBP algorithm. We do all the numerical experiments on a Linux cluster. In one typical experiment, the sequential reconstruction time is 781.3 seconds, while the parallel reconstruction time is 25.7 seconds with 32 processors.

Copyright © 2006 Jiansheng Yang et al. This is an open access article distributed under the Creative Commons Attribution License, which permits unrestricted use, distribution, and reproduction in any medium, provided the original work is properly cited.

## 1. INTRODUCTION

Spiral cone-beam CT can be used for rapid volumetric imaging with high longitudinal resolution and for efficient utilization of X-ray source. Katsevich's filtered-backprojection (FBP) inversion formula represents a significant breakthrough in this area [2–4]. However, sequential implementation of this formula demands more intensive computation and hardware resources [2, 3]. Parallel computation technique provides an effective solution to this issue.

Parallel computation technique was previously applied to 2D CT. Nowinski [5] investigated four forms of parallelism in 2D CT: pixel, projection, ray, and operation parallelisms. Using the data-parallel programming style, Roerdink and Westenberg [6] studied parallel implementation for two standard 2D reconstruction algorithms: FBP and direct Fourier reconstruction. There were also some results on parallel implementations of 3D CT image reconstructions for parallel-beam and fan-beam geometries [7, 8]. For cone-beam CT, parallel implementations of the Feldkamp algorithm on Beowulf clusters were reported, typically based on smart communication schemes [9, 10]. In [9], a master node does all the weighting and filtering of the projections, while the other nodes perform the backprojection for their assigned image subvolumes, respectively. In [10], each node weights and filters the projection data assigned to it, and then accomplishes the backprojection for its assigned image subvolume in a send-receive mode.

For image reconstruction from cone-beam projections, the backprojection step is extremely time-consuming. In [1], the authors proposed the cone-beam cover method for the backprojection. This method is different from the conven-

tional methods based on PI line, and provides an alternative efficient implementation scheme for Katsevich's FBP formula and its kind. In the cone-beam cover method, any filtered cone-beam projection can be backprojected independently. On the ground of this independence, we present a parallel implementation for Katsevich's exact reconstruction formula in this manuscript. Numerical simulations demonstrate the high performance of the proposed parallel scheme with remarkable runtime reduction. For the 3D Shepp-Logan phantom [11] with  $256 \times 256 \times 256$  voxels,  $3 \times 600$  source points (600 points per turn) and  $100 \times 500$  cone-beam projection at every source point, the sequential cone-beam cover algorithm takes 781.3 seconds to reconstruct the volume image, while the proposed parallel implementation only needs 25.7 seconds with 32 processors on the same Linux cluster.

The structure of this manuscript is as follows. Section 2 introduces briefly Katsevich's inversion formula and the cone-beam cover method. Section 3 describes the proposed parallel implementation of Katsevich's inversion formula. Section 4 provides experiment results and details of the computing environment. Section 5 discusses relevant issues. Finally, Section 6 concludes the paper.

## 2. THE CONE-BEAM COVER METHOD

As shown in Figure 1, let  $C$  be a spiral defined by

$$C := \left\{ y \in R^3 : y_1 = R \cos(s), y_2 = R \sin(s), \right. \\ \left. y_3 = s \left( \frac{h}{2\pi} \right), s \in I \right\}, \quad (1)$$

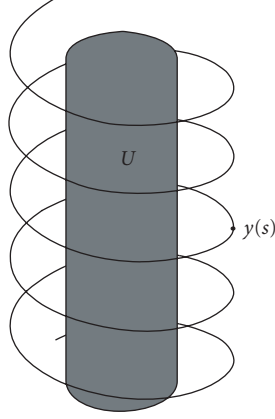


FIGURE 1: The spiral and image space  $U$ .

where  $s$  is the angular parameter,  $h > 0$  is the spiral pitch and  $I := [a, b]$ ,  $b > a$ . Let  $U$  be the image space defined by

$$U := \left\{ x \in \mathbb{R}^3 : x_1^2 + x_2^2 < r^2, c \left( \frac{h}{2\pi} \right) < x_3 < d \left( \frac{h}{2\pi} \right) \right\}, \quad (2)$$

where  $0 < r < R$ ,  $c < d$ ,  $a = c - s_\Delta$ ,  $b = d + s_\Delta$ ,  $s_\Delta$  is the necessary offset of the angular parameter [1–4]. It is assumed that an object  $f(x)$  is centered at the coordinate origin and supported by  $U$ , that is,  $f(x) = 0$  if  $x \notin U$ . The cone-beam (at vertex  $y$ ) projection of  $f$  is defined by

$$D_f(y, \beta) := \int_0^\infty f(y + t\beta) dt, \quad \beta \in S^2. \quad (3)$$

Katsevich's FBP inversion formula [3] can be represented as

$$f(x) = -\frac{1}{2\pi^2} \int_{I_{PI}(x)} \frac{1}{|x - y(s)|} \times \int_0^{2\pi} \frac{\partial}{\partial q} D_f(y(q), \Theta(s, x, y)) \Big|_{q=s} \frac{dy}{\sin \gamma} ds, \quad (4)$$

where  $I_{PI}(x) := [s_b(x), s_t(x)]$  is the PI parametric interval which is determined by the PI line  $L_{PI}(x)$  passing through  $x$  [12], see Figure 2.

This formula can be rewritten as

$$f(x) := -\frac{1}{2\pi^2} \int_{I_{PI}(x)} \frac{1}{|x - y(s)|} \Psi(s, \beta(s, x)) ds, \quad (5)$$

where

$$\beta(s, x) = \frac{x - y(s)}{|x - y(s)|}, \quad (6)$$

$$\Psi(s, \beta) := \int_0^{2\pi} \frac{\partial}{\partial q} D_f(y(q), \cos(\gamma)\beta + \sin(\gamma)e(s, \beta)) \Big|_{q=s} \frac{1}{\sin \gamma} d\gamma, \quad (7)$$

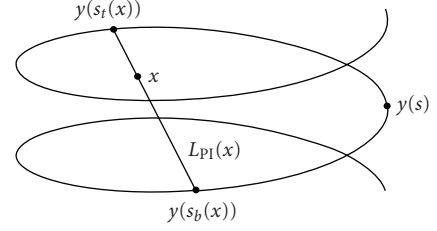


FIGURE 2: PI-line and PI parametric interval. A PI-line is a line segment, the endpoints of which are separated by less than one turn in the spiral. Any  $x \in U$  belongs to one and only one PI-line, denoted as  $L_{PI}(x)$ . Endpoints of  $L_{PI}(x)$  are denoted as  $y(s_b(x))$  and  $y(s_t(x))$ , where  $s_b(x)$  and  $s_t(x)$  are angular parameters of the endpoints and  $s_b(x) < s_t(x)$ . The interval  $I_{PI}(x) := [s_b(x), s_t(x)]$  is called PI parametric interval. The section of the spiral between  $y(s_b(x))$  and  $y(s_t(x))$  is called PI arc, denoted as  $C_{PI}(x)$ .

for the unit vector  $\beta$  along which X-ray emitted from  $y(s)$  will reach the Tam-Danielsson window [13, 14], see Figure 3.

Equations (5) and (7) imply that the inversion formula is of the filtered-backprojection type. One first computes the shift-invariant filtering of derivative of cone-beam projection using (7) [3, 15, 16]. Then one performs the backprojection according to (5). Here, for every  $x \in U$ , the backprojection is performed along PI arc  $C_{PI}(x)$  (the PI line method).

In [1], we introduce the cone-beam cover method to perform backprojection in a way different from the PI line method.

*Definition 1.* Let  $W(s_0)$  be the Tam-Danielsson window at source point  $y(s_0)$  ( $s_0 \in I$ ), we call

$$V(s_0) := \{x \in U : \hat{x} \in W(s_0)\} \quad (8)$$

cone-beam cover at source point  $y(s_0)$ , where  $\hat{x}$  is the projection of  $x$  onto the detector plane, see Figure 4.

The following theorem on the cone-beam cover was proved in [1]. It is the footstone of the cone-beam cover method.

**Theorem 1.** For  $x \in U$ , one has

$$x \in V(s_0) \quad \text{iff} \quad s_0 \in I_{PI}(x). \quad (9)$$

Applying Theorem 1 to the discrete form of (5):

$$f(x) = -\frac{1}{2\pi^2} \sum_{s \in I_{PI}(x)} \frac{\Psi(s, \beta(s, x)) \Delta s}{|x - y(s)|}, \quad (10)$$

we obtain the following equation

$$f(x) = -\frac{1}{2\pi^2} \sum_{\{s: x \in V(s)\}} \frac{\Psi(s, \beta(s, x)) \Delta s}{|x - y(s)|}. \quad (11)$$

Equation (11) implies that the filtered cone-beam projection at any source point  $y(s)$  contributes only to the reconstruction of voxels in  $V(s)$ . Based on this fact, the cone-beam cover

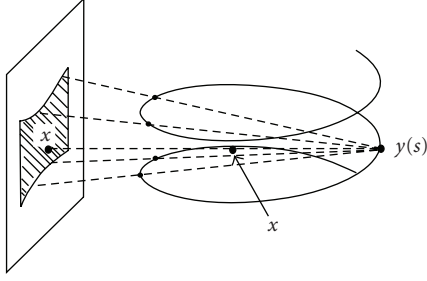


FIGURE 3: Tam-Danielsson window. The Tam-Danielsson window is a region on the detector plane. It is bounded by the cone-beam projection of the upper and lower turns of the spiral onto the detector plane.

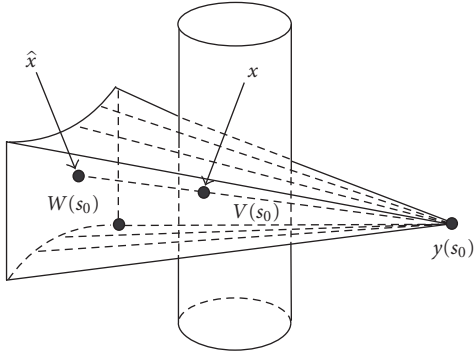


FIGURE 4: Cone-beam cover  $V(s_0)$ . Let  $\tilde{V}(s_0)$  be the cone with vertex  $y(s_0)$  and base  $W(s_0)$ , then  $V(s_0) = \tilde{V}(s_0) \cap U$ .

method provides an approach to performing backprojection. The key point is as follows.

At any source point  $y(s)$ , the cone-beam projection

$$D_f(y(s), \beta) := \int_0^\infty f(y(s) + t\beta) dt \quad (12)$$

is truncated by those unit vector  $\beta$  along which X-rays emitted from  $y(s)$  will reach a region slightly larger than Tam-Danielsson window  $W(s)$  on the detector plane [3]. As shown in Figure 5, the region is bounded by the parallelogram. Dealing with this cone-beam projection, one first computes the shift-invariant filtering of derivative of the cone-beam projection using (7) along the lines  $L(s_2)$  (see Figure 5), as discussed elsewhere [3, 16]. Then one performs the backprojection according to (11). Here with the filtered cone-beam projection at source point  $y(s)$  the backprojection is performed only for  $x \in V(s)$ .

Note that using the above strategy, both filtering and backprojecting on a single cone-beam projection can be performed independently. This property of the strategy leads to the sequential and parallel algorithms we will describe later.

A sequential implementation of Katsevich's FBP formula is stated in Algorithm 1. More details and experiment results about this implementation can be found in [1].

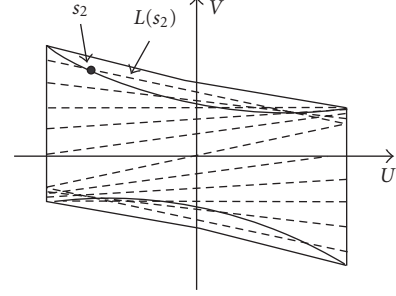


FIGURE 5: The family of lines  $L(s_2)$ . The filtering is performed along lines  $L(s_2)$ .

```

Step 1. for each voxel  $x$  of image space, set  $f(x) = 0$ .
Step 2. for each source point  $y(s)$ ,  $s \in I$ 
do
  (1) Filtering of derivative of the cone-beam
  projection, get  $\Psi(s, \beta(s, x))$ .
  (2) Backprojecting for  $x \in V(s)$ 

$$f(x) = f(x) + \left(-\frac{1}{2\pi^2}\right) \left(\frac{1}{|x - y(s)|}\right) \times \Psi(s, \beta(s, x)) \Delta s.$$

end
    
```

ALGORITHM 1: Sequential implementation of Katsevich's FBP inversion formula.

### 3. PARALLEL IMPLEMENTATION

We parallelize the above sequential implementation by partitioning the source points set. Let  $\bar{I}$  be a discretization of  $I$  (angular parameter interval),  $p$  be the number of processors. If  $\bar{I}$  is partitioned into  $p$  subsets

$$\bar{I} = \bigcup_{j=1}^p I_j, \quad (13)$$

then a parallel implementation of Katsevich's FBP formula can be pseudocoded Algorithm 2.

In Algorithm 2, each processor  $j$  just operates on its assigned cone-beam projections and gets  $f_j(x)$ , and no communication between different processors is needed during the processing.

### 4. EXPERIMENTS

We do all computations on the Beowulf cluster CCSE-HP at Peking University. The cluster consists of 1 master node, 2 login nodes, 4 I/O nodes, and 128 computing nodes. All the nodes are on a Gigabit Ethernet. The computing nodes are also connected by 4 X InfiniBand (10 Gbps). The system configuration is listed in Table 1.

TABLE 1: System configuration.

Computing node	HP ProLiant DL360 G4 server, Dual 64-bit 3.2 GHz Xeon™ DP, 1 MB L2 cache, 4 GB DDR333 RAM, 73 GB Ultra320 SCSI disk, Voltaire HCA 400 PCI-X dual-port 4X InfiniBand (10 Gbps) host channel adapter
I/O node	HP ProLiant DL380 G4 server, Dual 64-bit 3.2 GHz Xeon™ DP, 1 MB L2 cache, 4 GB DDR333 RAM, Gigabit Ethernet adapter, HP Smart Array 6402/128M SCSI controller
Master node	Same as the computing node, except that the RAM is 2 GB
Login node	Same as the computing node, except the InfiniBand host interface
InfiniBand switch	Voltaire ISR 9288
Gigabit Ethernet switch	HP ProCurve Switch 2848
Storage	HP StorageWorks Modular Smart Array 30, 7TB (RAID5)
Operating system	Red Hat EL WS 3.0
Compilers	Intel 64-bit Compiler 9.0.021 (c/c++)
Parallel Environment	mpich 1.2.6-ib

```

Step 1. for each voxel  $x$  of image space, set  $f(x) = 0$ .
Step 2. for each processor  $j$  ( $j = 1, \dots, P$ ),
do
  for each voxel  $x$  of image space, set  $f_j(x) = 0$ .
  for each source point  $y(s), s \in I_j$ 
  do
    (1) Filtering of derivative of the
        cone-beam projection, get  $\Psi(s, \beta(s, x))$ .
    (2) Backprojecting for  $x \in V(s)$ 

$$f_j(x) = f_j(x) + \left(-\frac{1}{2\pi^2}\right) \left(\frac{1}{|x - y(s)|}\right) \times \Psi(s, \beta(s, x)) \Delta s.$$

  end
  set  $f(x) = f(x) + f_j(x)$ .
end

```

ALGORITHM 2: Parallel implementation of Katsevich's FBP inversion formula.

The parameters of the data collection protocol are given in Table 2.

We use the 3D Shepp-Logan phantom [11] to test our parallel algorithm. The phantom consists of 10 ellipsoids as specified in Table 3.

Figure 6 shows the reconstructed images from sequential and parallel implementations at slices of  $x_3 = -0.255$ ,  $x_2 = -0.067$ , and  $x_1 = -0.067$ , respectively. We use the gray scale window [1.01, 1.03] to make low contrast features visible.

In terms of runtime, speedup  $S$  is defined as the ratio of the time taken to solve a problem on a single processor to the time required to solve the same problem on a parallel

TABLE 2: Parameters of the data collection protocol.

$R$ (radius of the spiral)	3
$h$ (pitch of the spiral)	1
$r$ (radius of the object)	1
$[c, d]$	$[-2\pi, 2\pi]$
$s_\Delta$	2.26
$[a, b]$	$[-2\pi - 2.26, 2\pi + 2.26]$
Sampling number of source points per tun	600
Detector array size	$100 \times 500$
Image volume	$256 \times 256 \times 256$

computer with  $P$  identical processors. Efficiency  $E$  is defined as the ratio of speedup to the number of processors:

$$S = \frac{T_1}{T_P}, \quad E = \frac{S}{P}, \quad (14)$$

where  $T_1$  and  $T_P$  represent the computing time for one processor and  $P$  processors respectively [17]. Figures 7 and 8 display the speedup and efficiency of Algorithm 2, respectively.

## 5. DISCUSSIONS

Since the computation of image reconstruction in Algorithm 2 is mathematically equivalent to that in Algorithm 1, the image reconstructed by Algorithm 2 is the same as that done by Algorithm 1.

Figures 7(a) and 8(a) depict the algorithm's speedup and efficiency with the uniform partition of  $\bar{I}$ . We can see that the speedup increases from 1.0 to 22.9 while the efficiency decreases from 100.0% to 71.5% when the number of processors varies from 1 to 32. Obviously, the efficiency is not satisfactory with four or more processors. Figure 9 displays

TABLE 3: Parameters of the low-contrast Shepp-Logan phantom.

No.	$a$	$b$	$c$	$x_{10}$	$x_{20}$	$x_{30}$	$\phi$	$A$
1	0.6900	0.920	0.900	0.00	0.000	0.000	0	2.00
2	0.6624	0.874	0.880	0.00	0.000	0.000	0	-0.98
3	0.4100	0.160	0.210	-0.22	0.000	-0.250	108	-0.02
4	0.3100	0.110	0.220	0.22	0.000	-0.250	72	-0.02
5	0.2100	0.250	0.500	0.00	0.350	-0.250	0	0.02
6	0.0460	0.046	0.046	0.00	0.100	-0.250	0	0.02
7	0.0460	0.023	0.020	-0.08	-0.650	-0.250	0	0.01
8	0.0460	0.023	0.020	0.06	-0.650	-0.250	90	0.01
9	0.0560	0.040	0.100	0.06	-0.105	0.625	90	0.02
10	0.0560	0.056	0.100	0.00	0.100	0.625	0	-0.02

\*  $a, b, c$  are the lengths of half-axes of ellipsoid.  $x_{10}, x_{20}, x_{30}$  are the coordinates of the center.  $\phi$  is the rotation angle around  $x_3$ -axis,  $A$  is the incremental density.

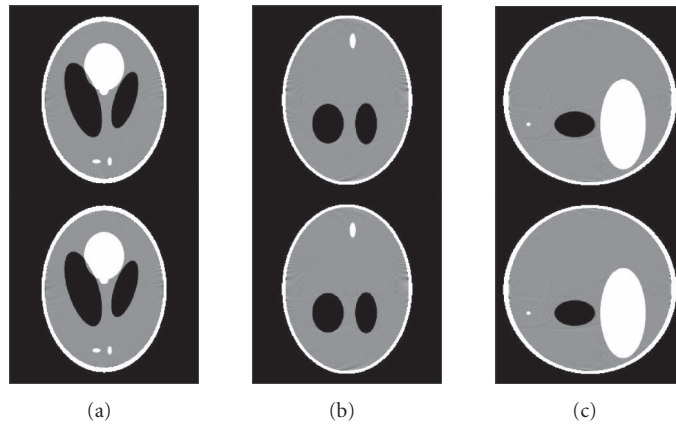


FIGURE 6: (a) Slice:  $x_3 = -0.255$ ; (b) slice:  $x_2 = -0.067$ ; (c) slice:  $x_1 = -0.067$ . Top: reconstructed image by Algorithm 1; bottom: reconstructed image by Algorithm 2. Since the computation of image reconstruction in Algorithm 2 is same as that in Algorithm 1, the images reconstructed by Algorithm 2 are same as those by Algorithm 1.

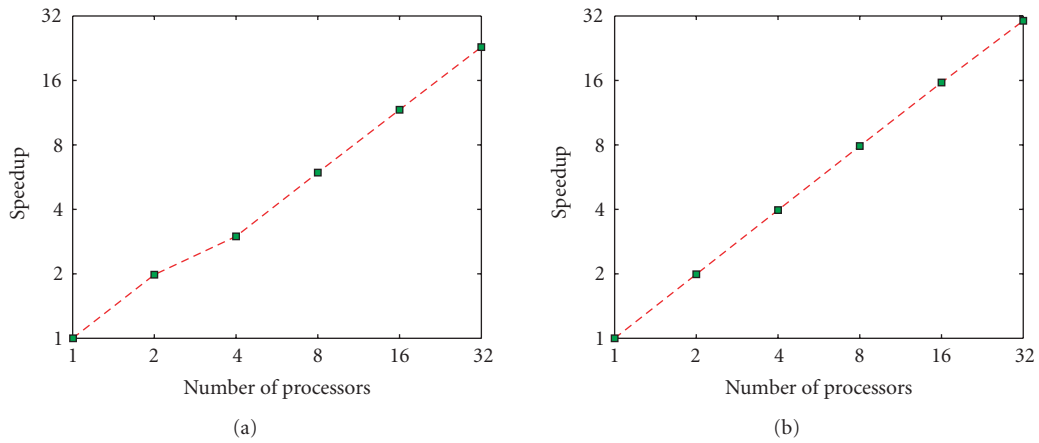


FIGURE 7: (a) Speedup with the uniform partition of  $\bar{I}$ ; (b) speedup with the nonuniform partition of  $\bar{I}$ . The speedup with the nonuniform partition of  $\bar{I}$  is better than that with the uniform partition of  $\bar{I}$ .

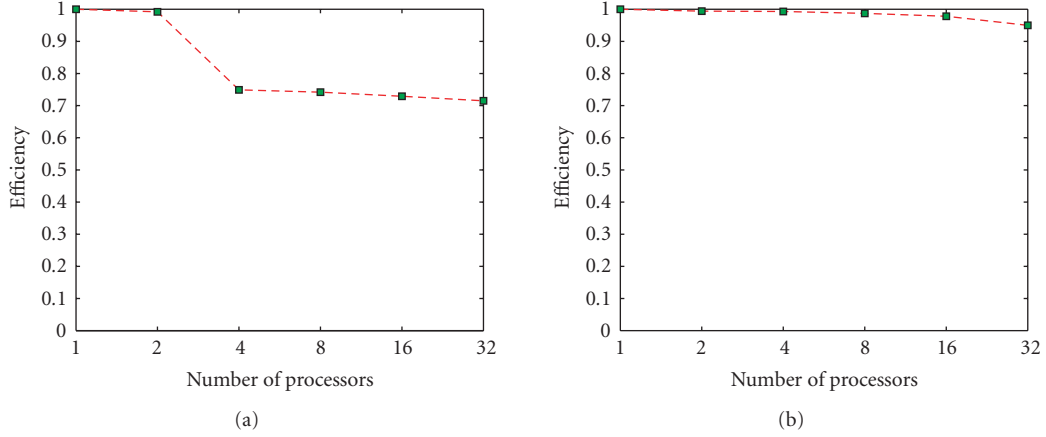


FIGURE 8: (a) Efficiency with the uniform partition of  $\bar{I}$ ; (b) efficiency with the nonuniform partition of  $\bar{I}$ . The efficiency with nonuniform partition of  $\bar{I}$  is better than that with the uniform partition of  $\bar{I}$ .

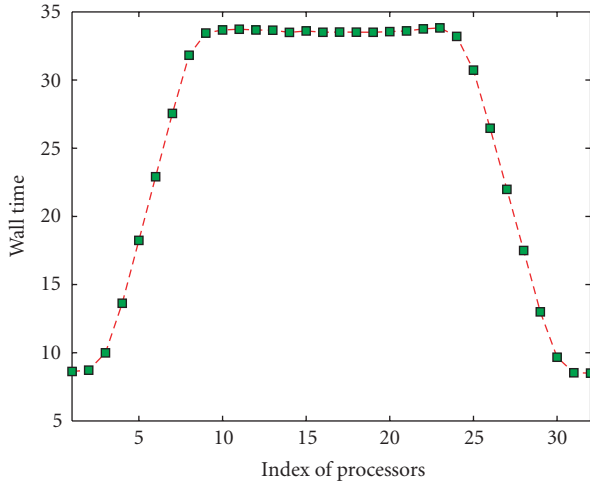


FIGURE 9: Wall time of each processor with the uniform partition of  $\bar{I}$ . The graph looks like a trapezoid, exhibiting a problem of load imbalance. The processors in the middle bear higher load, while those on the two sides bear lower load.

the wall time<sup>1</sup> for each processor. The graph looks like a trapezoid, exhibiting a problem of load imbalance. The processors in the middle bear higher load, while those on the two sides bear lower load.

The reason is as follows. When the X-ray source point goes near the bottom or top of the image space, the cone-beam cover becomes smaller and smaller, making the load of the corresponding processors lower and lower. Nonuniform partition of  $\bar{I}$  can overcome the load imbalance. The following describes a scheme of nonuniform partition of  $\bar{I}$ .

<sup>1</sup> “Real world” time (what the clock on the wall shows), as opposed to the system clock’s idea of time. <http://computing-dictionary.thefreedictionary.com/wall%20time>.

Recall that  $I = [a, b]$  is the angular parameter interval of the spiral, the interval  $[c, d]$  expresses the axial position of image space  $U$ . Let  $s_\Delta$  be the maximal axial-direction distance of points in the cone-beam cover from the source point  $y(s)$ . Then  $a = c - s_\Delta$ ,  $b = d + s_\Delta$ . Figure 10 illustrates computation time for the filtering and backprojecting at source point  $y(s)$ .

We divide  $[a, a + 2s_\Delta]$ ,  $[a + 2s_\Delta, b - 2s_\Delta]$ ,  $[b - 2s_\Delta, b]$  into  $p$  uniform subintervals, respectively, as

$$\begin{aligned}
 [a, a + 2s_\Delta] &= \bigcup_{j=1}^p I_{1,j}, & [a + 2s_\Delta, b - 2s_\Delta] &= \bigcup_{j=1}^p I_{2,j}, \\
 [b - 2s_\Delta, b] &= \bigcup_{j=1}^p I_{3,j},
 \end{aligned} \tag{15}$$

and let

$$I_j = I_{1,j} \cup I_{2,j} \cup I_{3,j}, \quad j = 1, \dots, p, \tag{16}$$

then

$$[a, b] = \bigcup_{j=1}^p I_j \tag{17}$$

determines a nonuniform partition of  $\bar{I}$ .

Figures 7(b) and 8(b) display the algorithm’s speedup and efficiency with the above nonuniform partition of  $\bar{I}$ . We can see that the speedup increases from 1.0 to 30.4 and the efficiency decreases from 100% to 95% when the number of processors varies from 1 to 32. The speedup and the efficiency with the nonuniform partition of  $\bar{I}$  are apparently better than those with the uniform partition of  $\bar{I}$ . The algorithm’s speedup and efficiency maintain a higher level with larger image sizes. The algorithm’s speedup and efficiency with the image volume  $512 \times 512 \times 512$  are displayed in Figure 11.

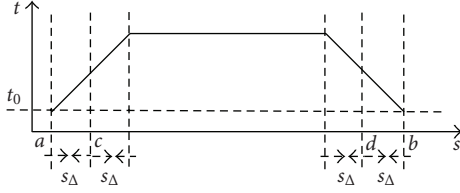
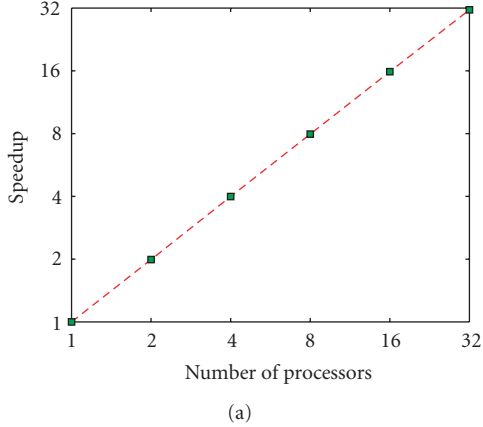
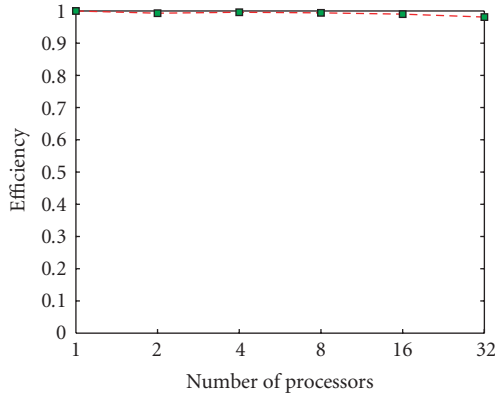


FIGURE 10: Computation time for the filtering and backprojecting at source point  $y(s)$ . The time of the filtering is same at all source points and denoted by  $t_0$ .



(a)



(b)

FIGURE 11: The illustration of the algorithm’s speedup and efficiency with the image volume  $512 \times 512 \times 512$ .

The idea of the cone-beam cover is a key point for us to design the parallel implementation of Katsevich’s inversion formula. From the perspective of the cone-beam cover, backprojecting any filtered cone-beam projection can be performed independently. Therefore a partition of cone-beam projections gives a parallel implementation of image reconstruction. The presented results demonstrate the high performance of the proposed parallel algorithm. The cone-beam cover method can also be employed to establish parallel schemes for other reconstruction algorithms, such as Feldkamp-type algorithms [11, 18], Zou and Pan’s algorithm [19, 20]. In addition, parallel implementation of the

Katsevich’s FBP algorithm based on PI line method would be an important topic of future research.

## 6. CONCLUSIONS

For spiral cone-beam CT, parallel computing is an effective approach to improving the reconstruction efficiency. Basing on the cone-beam cover method, we have proposed an efficient parallel implementation of Katsevich’s FBP algorithm and demonstrated its high performance with numerical simulations. Further work is under active investigation.

## ACKNOWLEDGMENTS

This work is supported in part by the National Basic Research Program of China under Grant 2003CB716101, National Science Foundation of China under Grant 60325101, 60532080, 60372024, the key project of Chinese Ministry of Education under Grant 306017, Engineering Research Institute of Peking University. We would like to thank Professor Linbo Zhang from the State Key Laboratory of Scientific and Engineering Computing, Chinese Academy of Sciences for valuable discussions. We would also like to thank the Center for Computational Science and Engineering of Peking University for providing computing facility.

## REFERENCES

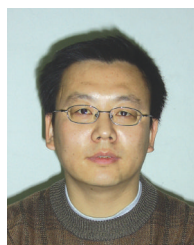
- [1] J. Yang, Q. Kong, T. Zhou, and M. Jiang, “Cone-beam cover method: an approach to performing backprojection in Katsevich’s exact algorithm for spiral cone-beam CT,” *Journal of X-Ray Science and Technology*, vol. 12, pp. 199–214, 2004.
- [2] A. Katsevich, “Theoretically exact filtered backprojection-type inversion algorithm for spiral CT,” *SIAM Journal on Applied Mathematics*, vol. 62, pp. 2012–2026, 2002.
- [3] A. Katsevich, “Improved exact FBP algorithm for spiral CT,” *Advances in Applied Mathematics*, vol. 32, pp. 681–697, 2004.
- [4] A. Katsevich, “Analysis of an exact inversion algorithm for spiral cone-beam CT,” *Physics in Medicine and Biology*, vol. 47, pp. 2583–2597, 2002.
- [5] W. L. Nowinski, “Parallel implementation of the convolution method in image reconstruction,” in *CONPAR 90-VAPP IV*, H. Elurkhardt, Ed., vol. 457 of *Lecture Notes in Computer Science*, pp. 355–364, Zurich, Switzerland, September 1990.
- [6] J. B. T. M. Roerdink and M. A. Westenberg, “Data-parallel tomographic reconstruction: a comparison of filtered backprojection and direct Fourier reconstruction,” *Parallel Computing*, vol. 24, pp. 2129–2142, 1998.
- [7] C. M. Chen, S. Y. Lee, and Z. H. Cho, “A parallel implementation of 3D CT image reconstruction on hypercube multiprocessor,” *IEEE Transactions on Nuclear Science*, vol. 37, no. 3, pp. 1333–1346, 1990.
- [8] Z. Cho, C. Chen, and S.-Y. Lee, “Incremental algorithm: a new fast backprojection scheme for parallel beam geometries,” *IEEE Transactions on Medical Imaging*, vol. 9, no. 2, pp. 207–217, 1990.
- [9] D. Reimann, C. Chaudhary, M. J. Flynn, and I. Sethi, “Cone beam tomography using MPI on heterogeneous workstation clusters,” in *Proceedings of the 2nd MPI Developer’s Conference*, pp. 142–148, Notre Dame, Ind, USA, 1996.

- [10] C. Laurent, F. Peyrin, J. M. Chassery, and M. Amiel, "Parallel image reconstruction on MIMD computers for three-dimensional cone beam tomography," *Parallel Computing*, vol. 24, pp. 1461–1479, 1998.
- [11] G. Wang, T. H. Lin, P. C. Cheng, and D. M. Shinozaki, "A general cone-beam reconstruction algorithm," *IEEE Transactions on Medical Imaging*, vol. 12, no. 3, pp. 486–496, 1993.
- [12] M. Defrise, F. Noo, and H. Kudo, "A solution to the long-object problem in helical cone-beam tomography," *Physics in Medicine and Biology*, vol. 45, pp. 623–643, 2000.
- [13] K. C. Tam, S. Smarasekela, and F. Sauer, "Exact cone-beam CT with a spiral scan," *Physics in Medicine and Biology*, vol. 43, pp. 1015–1024, 1998.
- [14] P. E. Danielsson, P. Edholm, and M. Seger, "Towards exact 3D-reconstruction for helical cone-beam scanning of long objects: a new detector arrangement and a new completeness condition," in *Proceedings of International Meeting on Fully Three-Dimensional Image Reconstruction in Radiology and Nuclear Medicine*, D. W. Townsend and P. E. Kinahan, Eds., pp. 141–144, Pittsburgh, Pa, USA, 1997.
- [15] F. Noo, J. Pack, and D. Heuscher, "Exact helical reconstruction using native cone-beam geometries," *Physics in Medicine and Biology*, vol. 48, pp. 3787–3818, 2003.
- [16] H. Yu and G. Wang, "Studies on implementation of the Katsevich algorithm for spiral cone-beam CT," *Journal of X-Ray Science and Technology*, vol. 12, pp. 97–116, 2004.
- [17] A. Grama, G. Karypis, V. Kumar, and A. Gupta, *Introduction to Parallel Computing: Design and Analysis of Algorithms*, Addison Wesley, Reading, Mass, USA, 2nd edition, 2003.
- [18] L. A. Feldkamp, L. C. Davis, and J. W. Kress, "Practical cone-beam algorithm," *Journal of the Optical Society of America A: Optics and Image Science, and Vision*, vol. 1, no. 6, pp. 612–619, 1984.
- [19] Y. Zou and X. Pan, "Exact image reconstruction on PI-lines from minimum data in helical cone-beam CT," *Physics in Medicine and Biology*, vol. 49, pp. 941–959, 2004.
- [20] Y. Zou and X. Pan, "Image reconstruction on PI-lines by use of filtered backprojection in helical cone-beam CT," *Physics in Medicine and Biology*, vol. 49, pp. 2717–2731, 2004.

**Jiansheng Yang** is a Lecturer in School of Mathematical Science, Department of Information Science, Peking University. He received his B.S. (1988) and M.S. (1991) degrees in mathematics from Peking University. He obtained his Ph.D. (1994) degree in applied mathematics from Peking University. His research interests include image reconstruction and wavelet.



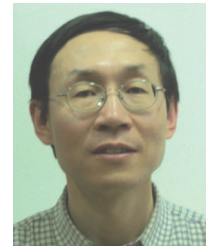
**Xiaohu Guo** is now a Postdoctor in School of Mathematical Science, Department of Information Science, Peking University. He obtained his Ph.D. degree in parallel computing from Institute of Computational Mathematics and Scientific/Engineering Computing of CAS, Beijing, China in 2004, and obtained his B.S. and M.S. degrees in computing mathematics from Department of Mathematics, Ningxia University, China in 1997 and 2000, respectively. His interests are parallel computing, image processing and reconstruction, CFD.



**Qiang Kong** received his B.S. degree in applied mathematics from Peking University, China in 2003. He is currently pursuing his M.S. degree in Peking University. His research interests include image reconstruction and parallel computing.



**Tie Zhou** is an Associate Professor of computational mathematics at Peking University. He received his Ph.D. degree in mathematics from Peking University (1994). He received his M.S. degree in mathematics from Peking University in 1990. He received his B.A. degree in mathematics from Peking University in 1985. His research interests include biomedical imaging, numerical partial differential equations, computational fluid dynamics.



**Ming Jiang** is a Professor with the School of Mathematical Science, Department of Information Science, Peking University. He obtained his B.S. and Ph.D. degrees in nonlinear analysis from Peking University in 1984 and 1989, respectively. He was Associate Professor with Department of Applied Mathematics, Beijing Institute of Technology from 1989 to 1995; Postdoctoral Fellow with Microprocessor Laboratory, International Centre for Theoretical Physics, Italy, from 1996 to 1997; Visiting Professor and Associate Director of CT/Micro-CT Laboratory, Department of Radiology, University of Iowa, USA, from 2000 to 2002. His interests are image reconstruction, restoration, and analysis.



# Local ROI Reconstruction via Generalized FBP and BPF Algorithms along More Flexible Curves

Hengyong Yu,<sup>1</sup> Yangbo Ye,<sup>1,2</sup> Shiyong Zhao,<sup>1</sup> and Ge Wang<sup>1,2</sup>

<sup>1</sup>CT/Micro-CT Laboratory, Department of Radiology, University of Iowa, Iowa City, IA 52242, USA

<sup>2</sup>Department of Mathematics, University of Iowa, Iowa City, IA 52242, USA

Received 12 October 2005; Accepted 20 December 2005

We study the local region-of-interest (ROI) reconstruction problem, also referred to as the local CT problem. Our scheme includes two steps: (a) the local truncated normal-dose projections are extended to global dataset by combining a few global low-dose projections; (b) the ROI are reconstructed by either the generalized filtered backprojection (FBP) or backprojection-filtration (BPF) algorithms. The simulation results show that both the FBP and BPF algorithms can reconstruct satisfactory results with image quality in the ROI comparable to that of the corresponding global CT reconstruction.

Copyright © 2006 Hengyong Yu et al. This is an open access article distributed under the Creative Commons Attribution License, which permits unrestricted use, distribution, and reproduction in any medium, provided the original work is properly cited.

## 1. INTRODUCTION

It is well known that the primary disadvantage of X-ray CT is ionizing radiation which may induce cancers and cause genetic damages with a probability related to the radiation dose. Thus, reducing the dose as low as possible is a general rule for practical medical applications. One effective way is to reduce the region or volume to be imaged. For example, reconstruction from truncated projections, which is also referred to as local region reconstruction, has been extensively studied. The existent algorithms can be categorized into three categories: (1) iterative methods [1, 2] which reconstruct the local ROI by minimizing I-divergence or maximizing statistical likelihood; (2) analytic methods such as those based on wavelet-based multi-resolution analyses [3, 4]; and (3) lambda tomography methods [5–7] which recover a gradient-like function of an object function.

To reconstruct a long object such as a patient, Katsevich proposed an exact and efficient FBP reconstruction algorithm [8, 9] for a standard cone-beam helical scanning trajectory. Zou and Pan derived a BPF algorithm [10]. Later, several groups independent generalized both the FBP [11, 12] and BPF [13–18] algorithms to more general scanning loci. These results offer a new opportunity to reconstruct the local ROI from truncated data. Based on the idea of combining global and local data for improved ROI reconstruction [3, 19–21], here we propose a local region reconstruction scheme which is novel in terms of the reconstruction methods, that is, the utilization of the recently developed generalized FBP and BPF algorithms. The major characteristic is to

deliver a normal radiation dose to a local ROI that may contain the cancerous tissue while applying a very low radiation dose to the structures outside the ROI.

In the following, the generalized FBP and BPF algorithms are briefly reviewed in Section 2. The ROI reconstruction scheme is described in Section 3. Simulated results and analysis are presented in Section 4. Finally, in Section 5 we conclude this paper.

## 2. REVIEW OF GENERALIZED FBP AND BPF ALGORITHMS

Based on Katsevich's FBP formula [9] for standard helical cone-beam CT, Ye and Wang derived a generalized FBP formula for exact image reconstruction from cone-beam data collected along a flexible three-dimensional (3D) curve [12]. The key step is to choose a filtering direction based on the general condition (see [12, equation 3.25]). A natural choice is the direction of the generalized PI-segment, also referred as a chord. As a result, the generalized FBP method does not require the uniqueness of the chord. In fact, it can be used to reconstruct images on any chord as long as a scanning curve runs from one endpoint of the chord to the other endpoint. We implemented this generalized formula and applied it to reconstruct images from data collected along a nonstandard saddle curve [22].

By interchanging the order of the Hilbert filtering and backprojection operation in Katsevich's FBP formula [9], Zou and Pan obtained a BPF formula for a standard helical

cone-beam CT [10], which reconstructs an object only from the minimum data in the Tam-Danielsson window. Our group contributed the first proof of the general validity of the BPF formula in the case of nonstandard spirals as well as other more general curves [14, 15, 22, 23]. Independent work on exact cone-beam reconstruction in the case of a general scanning curve was also independently reported by several groups [11, 13, 17, 18]. Although there are several schemes for constructing cone-beam inversion algorithms in a general case [24–27] before these recent publications, the generalized exact cone-beam reconstruction algorithms are explicit and straightforward. Note that earlier than our SPIE paper [14], Palamodov once formulated a general inverse formula [28]. Unfortunately, his formula is not theoretically exact [29]. Since a 2D locus can be regarded as a special class of 3D curves, we can readily obtain the corresponding generalized fan-beam reconstruction formulas [30]. Therefore, in this paper, we will discuss the reconstruction of a local ROI from truncated fan-beam and cone-beam data collected along flexible 2D/3D loci.

### 3. RECONSTRUCTION SCHEME

It is well known that a reconstructed 2D ROI from local truncated projection data suffers from image cupping and intensity shifting artifacts since the local CT problem is not uniquely solvable [31]. Based on the fact that the artifacts mainly distribute in low frequencies, the local ROI reconstruction can be improved by combining the truncated local projections and very few noisy global projections. Therefore, we can deliver a normal radiation dose to the local ROI that may contain the cancerous tissue while applying a very low radiation dose to the structures outside the ROI. As shown in Figure 1, there are two types of detectors: one is a local detector (solid thick line) which collects truncated local projections at a normal radiation dose rate, and the other is a global detector (dotted thin line) which collects global projections with very low radiation dose. For practical applications, the two types of detectors can be combined into one. As illustrated in Figure 1(a), this can be physically implemented by adding some lead filters in the current pre-patient collimator. Compared to the local normal-dose projections, the global low-dose projections can be obtained in two ways: (a) reducing the number of photons for each detector aperture; (b) shortening the scanning time by reducing the number of projections. The global data and local data can be acquired in two scans [21] or the same scan with an ROI beam filtering technique [20].

If the global and local data are acquired in two scans, an interpolation procedure is required to combine the two datasets. Assume that both the local and global detectors have the same scanning geometry. The local normal-dose projections  $P_{\text{local}}$  are finely sampled, while the global low-dose projections  $P_{\text{global}}$  are coarsely sampled. The two datasets can be combined as

$$P_{\text{global}}^c = \begin{cases} P_{\text{local}} & \text{if } P_{\text{local}} \text{ is defined,} \\ P_{\text{global}}^i & \text{otherwise,} \end{cases} \quad (1)$$

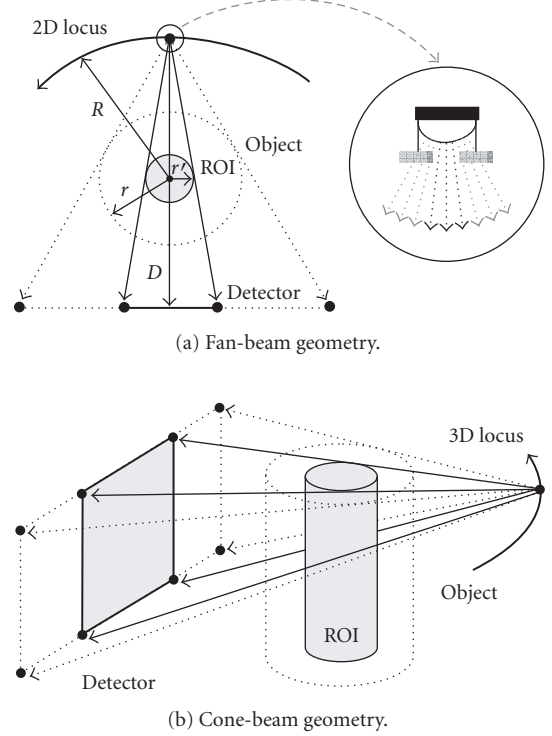


FIGURE 1: Configuration of the local region reconstruction from truncated local normal-dose data and global low-dose data. The dotted thin line represents the detector for global data while the solid thick line represents the detector for local data.

where  $P_{\text{global}}^i$  denotes the linear interpolation of  $P_{\text{global}}$  on the fine grid of  $P_{\text{local}}$ . The whole interpolation procedure is illustrated in Figure 2 for fan-beam geometry. Once the combined global dataset  $P_{\text{global}}^c$  is obtained, the local ROI can be reconstructed by either the generalized FBP or BPF method. For the implementation details of the reconstruction algorithms, please refer to our previous papers [22, 23, 30]. It is pointed out that the global dataset  $P_{\text{global}}^c$  can be directly acquired using an ROI beam filtering technique [20].

### 4. SIMULATION RESULTS

According to the analysis of our CMCT system [19], the organ dose, DOSE, is proportional to the total photons flux  $\Phi$ . Assume that there are  $N$  photons emitted from the X-ray source to each detector aperture, the number of detectors is  $S$ , and the number of projections is  $P$ ,  $\Phi$  will be proportional to  $N \times S \times P$ , that is,

$$\text{DOSE} \propto \Phi \propto N \times S \times P. \quad (2)$$

Hence, the ratio between the dose from global projections and that from local truncated data roughly is

$$\text{DOSE}_{\text{ratio}} = \frac{\text{DOSE}_{\text{global}}}{\text{DOSE}_{\text{local}}} = \frac{N_{\text{global}}}{N_{\text{local}}} \times \frac{S_{\text{global}}}{S_{\text{local}}} \times \frac{P_{\text{global}}}{P_{\text{local}}}, \quad (3)$$

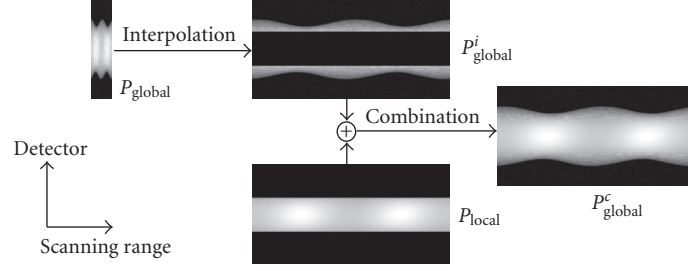


FIGURE 2: Illustration of combining local normal-dose data and global low-dose data in fan-beam geometry.

where the subscribes “global” and “local” indicate the global and local datasets, respectively.

Assume that among the  $N$  photons emitted by the X-ray source only  $\hat{N}$  photons arrive at the detector aperture due to attenuation in the object, and that the number of photons  $\hat{N}$  obeys a Poisson distribution. Since the dose level as described by noise variance is inversely proportional to the number of the detected photons  $\hat{N}$ , we can simulate projections at different dose levels in terms of Poisson random variables as a function of the number of the detected photons (see the appendix). To demonstrate the performance of the proposed algorithms, we implemented an X-ray projection simulator, and the generalized FBP and BPF algorithms in Matlab on a PC with all the computational intensive part coded in C++ language.

As shown in Figure 1(a), in our first set of numerical tests, a 2D differentiable Shepp-Logan phantom (DSLIP) [32] was confined in a disk of radius  $r = 10$  cm, and centered at the origin of the natural coordinate system. The X-ray source was rotated along a circular locus of radius  $R = 50$  cm. Collinear local and global detectors were combined with the local detector arranged in the middle of the global detector. The distance between the detector and the X-ray source was  $D = 100$  cm. Along a 40.82 cm length, 500 detector elements were distributed for global data, while 250 detector elements were spanned over 20.41 cm for local data. The local detectors covered all the projections of an ROI of radius  $r' = 5.08$  cm. In our simulation, 720 local truncated normal dose and 36 global low dose projections were equiangularly acquired in two scans. We set  $N = 1.0 \times 10^8$  per detector element for collection of local data at the normal dose. For different low-dose levels, global data were acquired, and the local ROI reconstructed by both the FBP and BPF methods, as shown in Figure 3. Furthermore, Table 1 includes the dose ratios and signal-to-noise ratio (SNR) in the ROI.

As the baseline, the last column of Table 1 gives the case when the global dataset was obtained using the same dose level and projection number as for the local dataset. From Table 1 and Figure 3, it can be observed that (a) there were some low-frequency artifacts at the edges of the ROI reconstructed by the FBP method; (b) there were some strip artifacts along the PI-segments all over the ROI reconstructed by the BPF method; (c) the FBP method offered better image quality in terms of SNR than the BPF method; (d) both the

FBP and BPF methods reconstructed satisfactory results by incorporating some low-dose global projections, at an additional cost of less than 1% purely local CT dose.

To demonstrate the flexible of the proposed scheme, our second set of numerical tests were to reconstruct a 3D local ROI from truncated cone-beam data along a nonstandard saddle curve. These tests were based on the experiments in [22]. All parameters are the same as those in [22] except the following: (a) the reconstructed object was a 3D DSLIP [32]; (b) the global detector array contained  $518 \times 592$  elements while the local detector array had  $256 \times 592$  elements; (c) 1200 local projections and 120 global projections were acquired in two scans. The numbers of photons for local normal-dose and global low-dose scans were  $N = 10^8$  and  $N = 10^4$  per detector element, respectively. The dose ratio was estimated as  $2.02 \times 10^{-5}$ . The SNRs in the local ROI reconstructed by the FBP and BPF algorithms were 49.94 dB and 49.32 dB, respectively. Figure 4 presents representative reconstructed images.

## 5. DISCUSSION AND CONCLUSION

Since the exact FBP and BPF algorithms are utilized, the proposed scheme is different from the existent ROI beam filtering technique [20] in which the approximate Feldkamp algorithm is used. Although our interpolation method (1) appears similar to the multi-resolution analysis method (MRAM) [3, 4, 21], we emphasize that the former is different from the latter in terms of the radiation dose. Both the global and local data are typically at the same dose level (noise level) in the MRAM, while here the dose level of the global data is far lower than that of the local data. Therefore, the contribution of this paper is to combine a normal-dose local ROI scan [3, 19–21] with a low-dose global scan, and apply the exact FBP and BPF reconstruction algorithms such as those described in [12, 15].

In conclusion, we have evaluated a new local ROI reconstruction scheme from data collected along scanning curves. By combining normal-dose local projections with some low-dose global projections, we have enhanced a local normal-dose dataset to a global dataset. Both the generalized FBP and BPF algorithms have been tested to reconstruct a local ROI. The simulation results have shown that both the FBP and BPF algorithms can produce excellent results with a minimal increment to the dose needed for purely local CT.

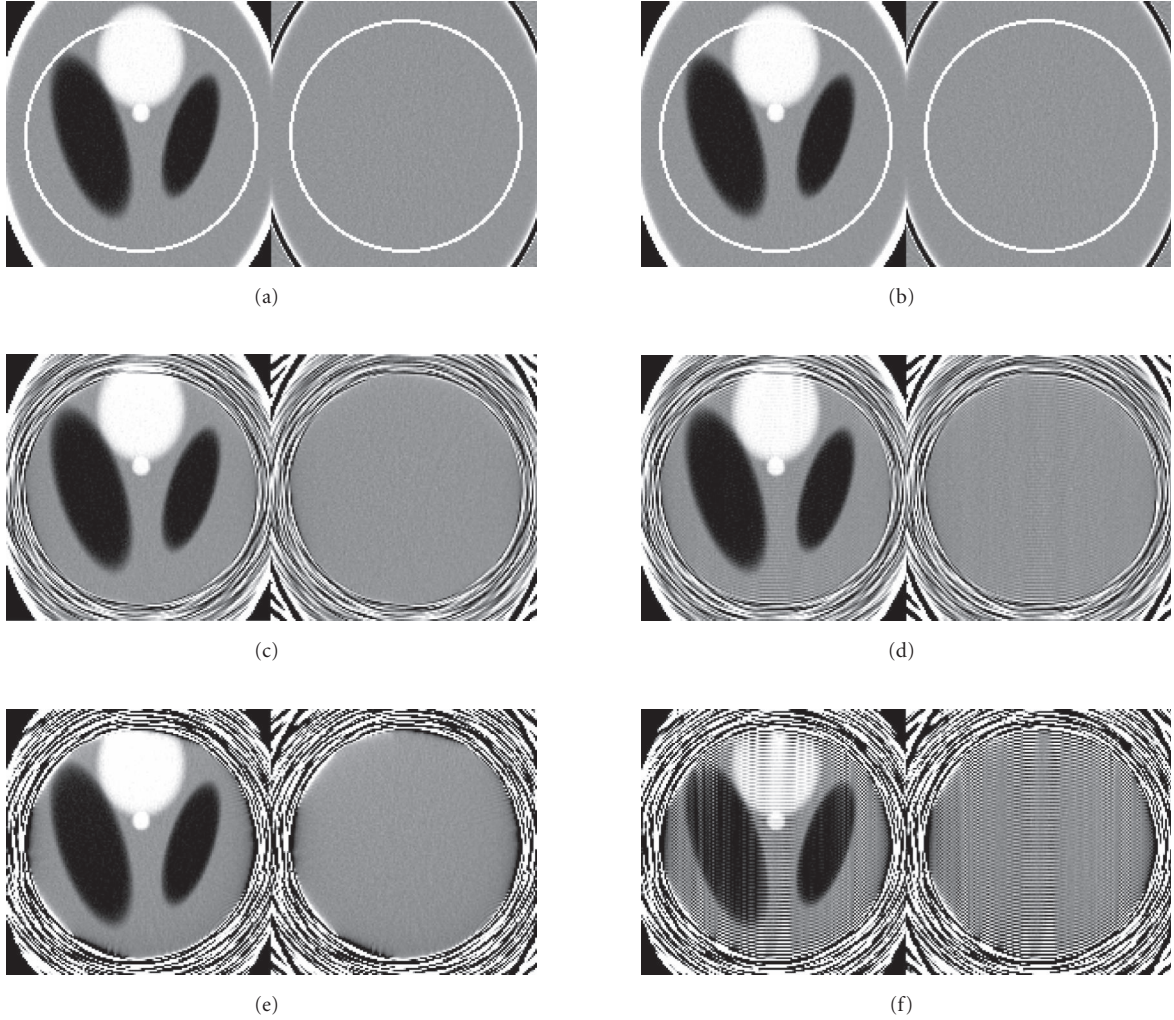


FIGURE 3: Reconstructed local ROI images of the DSLP with different low-dose levels for global projections. The left column was reconstructed by the FBP method while the right column by the BPF method. Each image includes a reconstructed image with a display window  $[1.0, 1.04]$  and a difference image against the real image with a display window  $[-0.02, 0.02]$ . The global projections for the first row were collected with the same  $N$  and  $P$  as that for the local projections. The white circle indicates the ROI.  $N$  for global data with the second and third rows were  $10^5$ ,  $10^3$ , respectively.

TABLE 1: Dose ratios and SNRs for different low-dose levels.

$N$	$10^7$	$10^6$	$10^5$	$10^4$	$10^3$	$10^2$	
$\text{DOSE}_{\text{ratio}}$	$10^{-2}$	$10^{-3}$	$10^{-4}$	$10^{-5}$	$10^{-6}$	$10^{-7}$	2.0
SNR with FBP (dB)	61.29	61.12	60.95	58.06	49.75	31.00	61.70
SNR with BPF (dB)	61.03	59.78	55.65	46.89	37.76	25.86	61.72

## APPENDIX

### Simulation of Poisson noise

When a material is bombarded by high-speed electrons, the X-ray photons are produced. After their interactions (photoelectric, Compton, and coherent scattering) with the material, some photons are absorbed or scattered. In other words, they are attenuated when they go through the material. The

attenuation process can be described by the Lambert-Beer law in the case of single energy photons. As a result, the number of the transmitted photons is a random variable obeying the Poisson distribution [33].

Assume that  $N$  photons are emitted from the X-ray source towards each detector aperture, we can simulate the Poisson noise inherent with projection data from the mathematical phantom as follows.

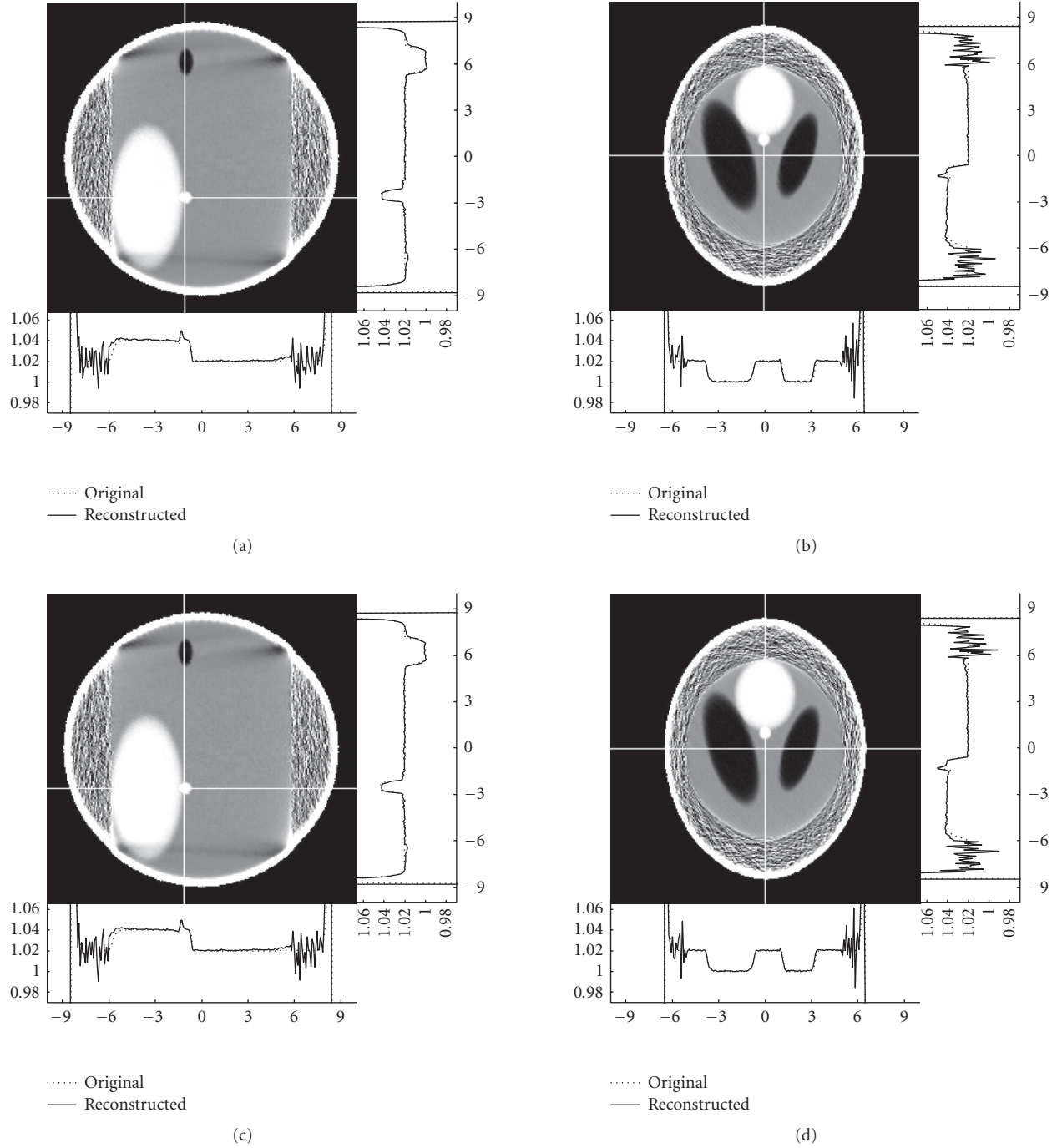


FIGURE 4: Typical reconstructed images of the DSLP from data collected along a nonstandard saddle curve with a display window  $[1.0, 1.04]$ . The top slices were reconstructed by the FBP method, while the bottom slices were reconstructed by the BPF method. The left and right slices are at  $X = 0$  cm and  $Z = -2.5$  cm, respectively. The two profiles along the white lines are plotted for each slice. The dotted and solid curves represent the original and reconstructed profiles.

*Step 1.* Compute the projection data  $p$  by linear integration.

*Step 2.* Compute the expected photon number arriving at the detector, according to the Lambert-Beer law  $\bar{N} = N \exp(-\mu_w p)$ , where  $\mu_w$  is the X-ray linear attenuation coefficient for water.

*Step 3.* Generate a Poisson random variable  $\hat{N}$ , with the mean and variance being equal to  $\bar{N}$ .

*Step 4.* Compute noisy projection data  $\tilde{p} = (1/\mu_w) \ln(N/\hat{N})$ .

Note that X-ray projection data  $p$  computed in Step 1 are based on the relative linear attenuation coefficients that have

been normalized with respect to the linear attenuation coefficient for water  $\mu_w$  [32]. Hence, in Step 2 the normalized projection data  $p$  must be converted to have realistic magnitudes by multiplying the normalized data  $p$  with the water coefficient  $\mu_w$ . Hence, with the formula  $\bar{N} = N \exp(-\mu_w p)$ , we can mimic the real X-ray attenuation process through the human head.

## ACKNOWLEDGMENT

This work is partially supported by the NIH/NIBIB Grants EB002667 and EB004287.

## REFERENCES

- [1] G. Wang, D. L. Snyder, and M. W. Vannier, "Local computed tomography via iterative deblurring," *Scanning*, vol. 18, no. 8, pp. 582–588, 1996.
- [2] G. Wang, M. W. Vannier, and P.-C. Cheng, "Iterative X-ray cone-beam tomography for metal artifact reduction and local region reconstruction," *Microscopy and Microanalysis*, vol. 5, no. 1, pp. 58–65, 1999.
- [3] T. Olson and J. DeStefano, "Wavelet localization of the Radon transform," *IEEE Transactions on Signal Processing*, vol. 42, no. 8, pp. 2055–2067, 1994.
- [4] S. Zhao and G. Wang, "Feldkamp-type cone-beam tomography in the wavelet framework," *IEEE Transactions on Medical Imaging*, vol. 19, no. 9, pp. 922–929, 2000.
- [5] M. A. Anastasio, D. Shi, X. Pan, C. Pelizzari, and P. Munro, "A preliminary investigation of local tomography for megavoltage CT imaging," *Medical Physics*, vol. 30, no. 11, pp. 2969–2980, 2003.
- [6] A. Faridani, E. L. Ritman, and K. T. Smith, "Local tomography," *SIAM Journal on Applied Mathematics*, vol. 52, no. 2, pp. 459–484, 1992.
- [7] A. Katsevich, "Cone beam local tomography," *SIAM Journal on Applied Mathematics*, vol. 59, no. 6, pp. 2224–2246, 1999.
- [8] A. Katsevich, "Theoretically exact filtered backprojection-type inversion algorithm for spiral CT," *SIAM Journal on Applied Mathematics*, vol. 62, no. 6, pp. 2012–2026, 2002.
- [9] A. Katsevich, "An improved exact filtered backprojection algorithm for spiral computed tomography," *Advances in Applied Mathematics*, vol. 32, no. 4, pp. 681–697, 2004.
- [10] Y. Zou and X. C. Pan, "Exact image reconstruction on PI-lines from minimum data in helical cone-beam CT," *Physics in Medicine and Biology*, vol. 49, no. 6, pp. 941–959, 2004.
- [11] J. D. Pack and F. Noo, "Cone-beam reconstruction using 1D filtering along the projection of M-lines," *Inverse Problems*, vol. 21, no. 3, pp. 1105–1120, 2005.
- [12] Y. B. Ye and G. Wang, "Filtered backprojection formula for exact image reconstruction from cone-beam data along a general scanning curve," *Medical Physics*, vol. 32, no. 1, pp. 42–48, 2005.
- [13] J. D. Pack, F. Noo, and R. Clackdoyle, "Cone-beam reconstruction using the backprojection of locally filtered projections," *IEEE Transactions on Medical Imaging*, vol. 24, no. 1, pp. 70–85, 2005.
- [14] Y. B. Ye, S. Zhao, H. Y. Yu, and G. Wang, "Exact reconstruction for cone-beam scanning along nonstandard spirals and other curves," in *Developments in X-Ray Tomography IV*, vol. 5535 of *Proceedings of SPIE*, pp. 293–300, Denver, Colo, USA, August 2004.
- [15] Y. B. Ye, S. Zhao, H. Y. Yu, and G. Wang, "A general exact reconstruction for cone-beam CT via backprojection-filtration," *IEEE Transactions on Medical Imaging*, vol. 24, no. 9, pp. 1190–1198, 2005.
- [16] S. Zhao, H. Y. Yu, and G. Wang, "A unified framework for exact cone-beam reconstruction formulas," *Medical Physics*, vol. 32, no. 6, pp. 1712–1721, 2005.
- [17] T. L. Zhuang, S. Leng, B. E. Nett, and G.-H. Chen, "Fan-beam and cone-beam image reconstruction via filtering the back-projection image of differentiated projection data," *Physics in Medicine and Biology*, vol. 49, no. 24, pp. 5489–5503, 2004.
- [18] Y. Zou and X. C. Pan, "An extended data function and its generalized backprojection for image reconstruction in helical cone-beam CT," *Physics in Medicine and Biology*, vol. 49, no. 22, pp. N383–N387, 2004.
- [19] G. Wang, S. Zhao, H. Y. Yu, et al., "Design, analysis and simulation for development of the first clinical micro-CT scanner," *Academic Radiology*, vol. 12, no. 4, pp. 511–525, 2005.
- [20] R. N. Chityala, K. R. Hoffmann, D. R. Bednarek, and S. Rudin, "Region of interest (ROI) computed tomography," in *Medical Imaging 2004: Physics of Medical Imaging*, vol. 5368 of *Proceedings of SPIE*, pp. 534–541, San Diego, Calif, USA, February 2004.
- [21] S. Azevedo, P. Rizo, and P. Grangeat, "Region-of-interest cone-beam computed tomography," in *Proceedings of the International Meeting on Fully Three-Dimensional Image Reconstruction in Radiology and Nuclear Medicine (3D '95)*, pp. 381–385, Aix les Bains, France, July 1995.
- [22] H. Y. Yu, S. Zhao, Y. B. Ye, and G. Wang, "Exact BPF and FBP algorithms for nonstandard saddle curves," *Medical Physics*, vol. 32, no. 11, pp. 3305–3312, 2005.
- [23] H. Y. Yu, Y. B. Ye, S. Zhao, and G. Wang, "A backprojection-filtration algorithm for nonstandard spiral cone-beam CT with an  $n$ -PI-window," *Physics in Medicine and Biology*, vol. 50, no. 9, pp. 2099–2111, 2005.
- [24] P. Grangeat, "Mathematical framework of cone beam 3D reconstruction via the first derivative of the Radon transform," in *Mathematical Methods in Tomography*, G. T. Herman, A. K. Louis, and F. Natterer, Eds., pp. 66–97, Springer, New York, NY, USA, 1991.
- [25] A. Katsevich, "A general scheme for constructing inversion algorithms for cone beam CT," *International Journal of Mathematics and Mathematical Sciences*, vol. 2003, no. 21, pp. 1305–1321, 2003.
- [26] B. D. Smith, "Image reconstruction from cone-beam projections: necessary and sufficient conditions and reconstruction methods," *IEEE Transactions on Medical Imaging*, vol. 4, no. 1, pp. 14–25, 1985.
- [27] H. K. Tuy, "An inversion formula for cone-beam reconstruction," *SIAM Journal on Applied Mathematics*, vol. 43, no. 3, pp. 546–552, 1983.
- [28] V. P. Palamodov, "Reconstruction from ray integrals with sources on a curve," *Inverse Problems*, vol. 20, no. 1, pp. 239–242, 2004.
- [29] H. Y. Yu, Y. B. Ye, S. Y. Zhao, and G. Wang, "Studies on Palamodov's algorithm for cone-beam CT along a general curve," to appear in *Inverse Problems*.
- [30] H. Y. Yu, et al., "Fan-beam reconstruction with compensation for in-plane motion based on data consistency," *IEEE Transactions on Medical Imaging*, under review.
- [31] F. Natterer, *The Mathematics of Computerized Tomography*, John Wiley & Sons, New York, NY, USA, 1986.
- [32] H. Y. Yu, S. Zhao, and G. Wang, "A differentiable Shepp-Logan phantom and its applications in exact cone-beam CT," *Physics in Medicine and Biology*, vol. 50, no. 23, pp. 5583–5595, 2005.

- [33] A. C. Kak and M. Slaney, *Principles of Computerized Tomographic Imaging*, SIAM, Philadelphia, Pa, USA, 2nd edition, 2001.

**Hengyong Yu** received his B.S. degree in information science and technology and his Ph.D. degree in information and communication engineering from Xi'an Jiaotong University, Xi'an, Shaanxi, China, in July 1998 and June 2003, respectively. He was an Instructor and Associate Professor with the College of Communication Engineering, Hangzhou Dianzi University, Hangzhou, Zhejiang, China, from July 2003 to September 2004. Currently, he is a Research Fellow with the CT/Micro-CT Laboratory, Department of Radiology, University of Iowa, Iowa City, USA. His interests include computed tomography and medical image processing. He has authored or coauthored more than 30 peer-reviewed papers. He serves as a Guest Editor of the International Journal of Biomedical Imaging for the special issue entitled *Development of Computed Tomography Algorithms*. He is a Member of the IEEE and the Chinese Institute of Electronics. He was honored for an outstanding doctoral dissertation by Xi'an Jiaotong University, and received the first prize for a best natural science paper from the Association of Science and Technology of Zhejiang Province.



in 1992–1996. He was an Associate Professor with the University of Iowa from 1997 to 2002. Currently, he is a Professor with the Departments of Radiology, Biomedical Engineering, Civil Engineering, and Mathematics, and the Director of the Center for X-ray and Optical Tomography, University of Iowa. His interests include computed tomography, bioluminescence tomography, and systems biomedicine. He has authored or coauthored over 300 journal articles and conference papers, including the first paper on spiral/helical cone-beam CT and the first paper on bioluminescence tomography. He is the Editor-in-Chief for the International Journal of Biomedical Imaging, and the Associate Editor for the IEEE Transactions on Medical Imaging and Medical Physics. He is an IEEE Fellow and an AIMBE Fellow. He is also recognized by a number of awards for academic achievements.

**Yangbo Ye** is a Professor of Mathematics and Professor of Radiology at the University of Iowa. In medical imaging, his research is focused on reconstruction formulas and algorithms. His recent research work includes proofs of exact reconstruction of cone-beam data scanned along an arbitrary locus in the filtered backprojection and backprojection filtration framework.



**Shiyong Zhao** received his B.A. degree in mechanical engineering from University of Science and Technology of China in 1982, M.S. degree in mechanical engineering from Shanghai Jiao Tong University, China, in 1985, and Ph.D. degree in mathematics from University of South Carolina, Columbia, South Carolina, in 1991. Currently, he is an Associate Professor with Department of Mathematics and Computer Science, University of Missouri - St. Louis. His research interests include X-ray tomography, wavelet analysis, and imaging processing.



**Ge Wang** received his B.E. degree in electrical engineering from Xidian University, Xi'an, China, in 1982, his M.S. degree in remote sensing from the Graduate School of Academia Sinica, Beijing, China, in 1985, and his M.S. and Ph.D. degrees in electrical and computer engineering from the State University of New York, Buffalo, in 1991 and 1992. He was the Instructor and Assistant Professor with the Department of Electrical Engineering, Graduate School of Academia Sinica in 1984–1988, the Instructor and Assistant Professor with Mallinckrodt Institute of Radiology, Washington University, St. Louis, Missouri,



# An Approximate Cone Beam Reconstruction Algorithm for Gantry-Tilted CT Using Tangential Filtering

Ming Yan,<sup>1</sup> Cishen Zhang,<sup>1,2</sup> and Hongzhu Liang<sup>1</sup>

<sup>1</sup> School of Electrical and Electronic Engineering, Nanyang Technological University, Singapore 639798

<sup>2</sup> School of Chemical and Biomedical Engineering, Nanyang Technological University, Singapore 639798

Received 30 November 2005; Revised 8 March 2006; Accepted 6 April 2006

FDK algorithm is a well-known 3D (three-dimensional) approximate algorithm for CT (computed tomography) image reconstruction and is also known to suffer from considerable artifacts when the scanning cone angle is large. Recently, it has been improved by performing the ramp filtering along the tangential direction of the X-ray source helix for dealing with the large cone angle problem. In this paper, we present an FDK-type approximate reconstruction algorithm for gantry-tilted CT imaging. The proposed method improves the image reconstruction by filtering the projection data along a proper direction which is determined by CT parameters and gantry-tilted angle. As a result, the proposed algorithm for gantry-tilted CT reconstruction can provide more scanning flexibilities in clinical CT scanning and is efficient in computation. The performance of the proposed algorithm is evaluated with turbell clock phantom and thorax phantom and compared with FDK algorithm and a popular 2D (two-dimensional) approximate algorithm. The results show that the proposed algorithm can achieve better image quality for gantry-tilted CT image reconstruction.

Copyright © 2006 Ming Yan et al. This is an open access article distributed under the Creative Commons Attribution License, which permits unrestricted use, distribution, and reproduction in any medium, provided the original work is properly cited.

## 1. INTRODUCTION

In some applications of clinical CT scanning, it is required that the CT gantry be tilted. For example, in order to avoid exposure of eyes to X-rays, gantry is tilted during the head scanning procedure. To meet such special requirements, a number of algorithms have been developed for gantry-tilted helical MSCT (multislice computed tomography) image reconstruction [1–4]. Among these algorithms, Kacherließ et al. [2] developed a gantry-tilted reconstruction algorithm based on the earlier developed 2D algorithm ASSR [5]. Hein et al. [3] developed a gantry-tilted reconstruction algorithm based on the 3D FDK algorithm [6, 7]. In the gantry-tilted FDK algorithm in [3], the reconstruction plane is perpendicular to the rotating axis of the CT scanning. Thus the scanning cone angle increases with the pitch value and slice number which can lead to unavoidable artifacts. Recently, Noo et al. [4] developed a general framework which can be applied to the gantry-tilted CT for exact [8, 9] and approximate image reconstruction.

The FDK-type algorithms for the approximate reconstruction using the projection data filtering in the horizontal direction suffer from considerable artifacts due to the large

scanning cone angle for both normal and gantry-tilted helical MSCT imaging. Recently, some of the improvements have been made for the FDK-type algorithms. The tilted plane technique is combined with the FDK algorithm to reduce the cone angle and further reduce artifacts caused by the large cone angle [10]. Several methods reduce the artifacts by filtering projection data along the tangential direction of the helix [11–13]. Such a technique was earlier proposed by Yan and Leahy [11] and further improved by Sourbelle and Kalender [12] for short scan FDK-type algorithms. The improved FDK-type algorithm can achieve better image quality than that of the conventional FDK algorithm.

Motivated by the observation that artifacts for FDK-type algorithms can be effectively reduced by filtering projection data along the helix tangential direction, this paper extends the existing tangential filtering technique to present a 3D FDK-type approximation algorithm for gantry-tilted helical MSCT. Taking into account the gantry-tilted geometry, we provide a general formula for gantry-tilted CT reconstruction for different gantry-tilted angles. As a special case, the reconstruction formula reduces to the standard tangential filtering for conventional CT with zero gantry-tilted angle.

To deal with the complicated gantry-tilted geometry and large scanning cone angle, our proposed algorithm first ap-

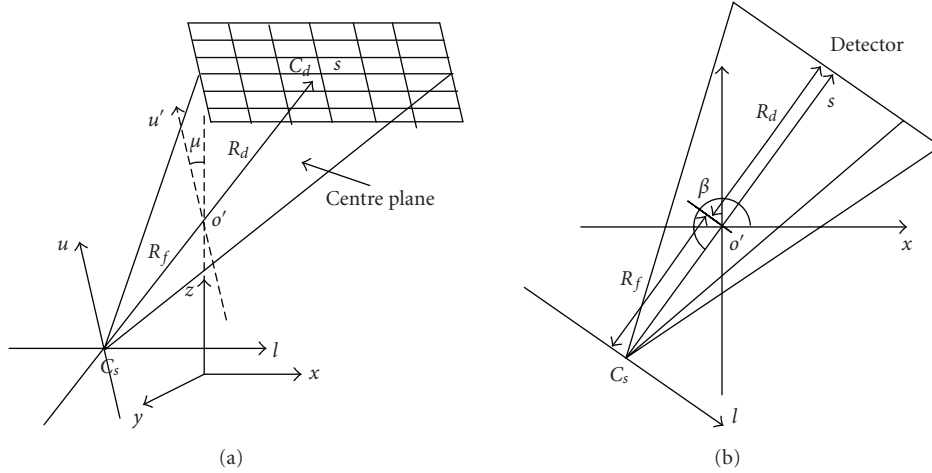


FIGURE 1: Geometry for gantry-tilted multislice CT scanner.

plies the ramp filtering to reconstruct a sequence of image planes and these planes are perpendicular to the rotating axis. The final horizontal image planes are then obtained by interpolating the tilted image planes. We present simulation results to show that the proposed gantry-tilted algorithm can provide considerably improved imaging for large scanning cone angle.

The key technique of the proposed algorithm is to reconstruct images on planes perpendicular to the rotation axis using the ramp filtering along the helix tangential direction. This is essentially different from the tilted plane reconstruction technique, such as that in [10], which is based on geometrically optimized reconstruction plane for reducing the effective cone angle.

It is noted that the tangential filtering technique can be implemented as a special case of the general framework for gantry-tilted CT proposed by Noo et al. [4]. Following its procedure, the gantry-tilted geometry is first transformed into a conventional CT scanning geometry with zero gantry-tilted angle and a projection data set of the transformed scanning geometry is formed. Then the tangential filtering technique can be applied on the data set for the image reconstruction. The procedure of the proposed algorithm in this paper is different from Noo et al.'s general framework in that it computes the helix tangential direction and applies the filtering directly without rebinning the projection data set for the transformed scanning geometry. This leads to more efficient computing and image reconstruction.

The rest of this paper is organized as follows. Section 2 presents the geometric scheme of the gantry-tilted CT. Section 3 is on the projection data set formation for tangential filtering. The proposed approximate reconstruction algorithm presented in Sections 4 and 5 is on simulation and evaluation of the proposed algorithm.

## 2. GEOMETRY FOR GANTRY-TILTED HELICAL MSCT

The helical MSCT scanning set up consists of an X-ray source and a detector array forming a source-detector framework.

The geometry of the source-detector framework in a global cartesian coordinate system  $x - y - z$  is shown in Figure 1(a), where  $C_s$  denotes the X-ray source, the detector array is a rectangular surface with a geometric centre  $C_d$ . The source-detector framework defines a rotating cartesian coordinate system  $s - l - u$  with the X-ray source  $C_s$  as the origin, the straight line  $C_s - C_d$  being the  $s$  axis, the  $l$  axis being parallel to the horizontal lines, and the  $u$  axis being parallel to the vertical lines of the rectangular detector surface.

The  $s - l$  plane containing  $C_s$  and  $C_d$  is called the centre plane and its geometry is shown in Figure 1(b), where  $\beta$  is the projection angle, the distances from the rotating centre point  $o'$  to the detector and the X-ray source are  $R_d$  and  $R_f$ , respectively. In the gantry-tilted scanning process, the source-detector framework rotates around the axis  $u'$  which is parallel to the  $u$  axis and intersects the  $z$  axis at  $o'$  as shown in Figure 1(a). The gantry-tilted angle is represented by  $\mu$  between the  $z$  and  $u'$  axes. And the projection angle  $\beta$  is defined in the  $s - l$  plane as shown in Figure 1(b).

For gantry-tilted CT, the X-ray source trajectory can be considered as a combination of two movements: the X-ray source rotates on the tilted circular trajectory with a radius  $R_f$  and the centre of the circle moves straightforward along the table feeding direction. As a result, the X-ray source trajectory is the sum of the circular rotation trajectory on the centre plane and the linear translation in the  $z$  direction in the following:

$$\begin{aligned}
 C_s(\beta) &= \begin{pmatrix} x_s \\ y_s \\ z_s \end{pmatrix} = \begin{pmatrix} 1 & 0 & 0 \\ 0 & \cos \mu & -\sin \mu \\ 0 & \sin \mu & \cos \mu \end{pmatrix} \begin{pmatrix} R_f \cos \beta \\ R_f \sin \beta \\ 0 \end{pmatrix} \\
 &+ \begin{pmatrix} 0 \\ 0 \\ z_0 + \frac{pSM}{2\pi}(\beta - \beta_0) \end{pmatrix} \\
 &= \begin{pmatrix} R_f \cos \beta \\ R_f \cos \mu \sin \beta \\ z_0 + \frac{pSM}{2\pi}(\beta - \beta_0) + R_f \sin \mu \sin \beta \end{pmatrix}, \tag{1}
 \end{aligned}$$

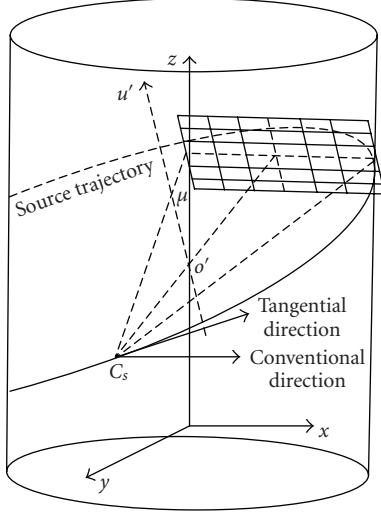


FIGURE 2: Illustration of conventional filter direction and tangential filter direction.

where  $\beta_0$  is the initial projection angle,  $z_0$  is the initial  $z$  position of the centre of the gantry,  $p$  is the pitch value of the helical cone beam scanning,  $S$  is the slice thickness, and  $M$  is the number of detector slice.

With the X-ray source trajectory given in (1), we take the derivative with respect to  $\beta$  to obtain its tangential direction at  $C_s$  in the global coordinate system represented in the following form:

$$\begin{pmatrix} x_t \\ y_t \\ z_t \end{pmatrix} = \frac{dC_s(\beta)}{d\beta} = \begin{pmatrix} -R_f \sin \beta \\ R_f \cos \mu \cos \beta \\ h + R_f \sin \mu \cos \beta \end{pmatrix}, \quad (2)$$

where  $h = pSM/2\pi$ . The X-ray source trajectory and its tangential direction at  $C_s$  are shown in Figure 2.

It follows from the geometric relation between the global  $x - y - z$  and the rotating  $s - l - u$  coordinate system, as shown in Figures 1(a) and 1(b), that the transformation of the tangential direction  $(x_t, y_t, z_t)^T$  as given in (2) to the rotating  $s - l - u$  coordinate system can be obtained by first rotating this vector by an angle  $\mu$  around the  $x$  axis followed a rotation angle of  $\beta - \pi$  around the  $u$  axis. This results in the trajectory tangential direction in the rotating  $s - l - u$  coordinate system, denoted by  $(s_t, l_t, u_t)^T$ , in the following:

$$\begin{aligned} \begin{pmatrix} s_t \\ l_t \\ u_t \end{pmatrix} &= \begin{pmatrix} \cos(\beta - \pi) & \sin(\beta - \pi) & 0 \\ -\sin(\beta - \pi) & \cos(\beta - \pi) & 0 \\ 0 & 0 & 1 \end{pmatrix} \\ &\times \begin{pmatrix} 1 & 0 & 0 \\ 0 & \cos \mu & \sin \mu \\ 0 & -\sin \mu & \cos \mu \end{pmatrix} \begin{pmatrix} -R_f \sin \beta \\ R_f \cos \mu \cos \beta \\ h + R_f \sin \mu \cos \beta \end{pmatrix} \quad (3) \\ &= \begin{pmatrix} -h \sin \beta \sin \mu \\ R_f + h \sin \mu \cos \beta \\ h \cos \mu \end{pmatrix}. \end{aligned}$$

To implement the tangential filtering for the gantry-tilted

scanning projection data, we further use the tangential direction  $(s_t, l_t, u_t)^T$  to set up a tangential cartesian coordinate system  $\xi - \eta - \zeta$ . The origin of this coordinate system is the X-ray source  $C_s$ , the  $\eta$  axis is defined by the tangential direction of the X-ray source trajectory at  $C_s$ , as given in (3), the  $\zeta$  axis is parallel to the detector plane, and the  $\xi - \zeta$  plane is orthogonal to the  $\eta$  axis.

Using the tangential direction  $(s_t, l_t, u_t)^T$  in (3), we introduce two angular quantities  $\sigma$  and  $\gamma$  as follows:

$$\sigma = \arcsin \left( \frac{s_t}{\sqrt{s_t^2 + l_t^2}} \right) \quad (4)$$

$$= \arcsin \left( \frac{-h \sin \mu \sin \beta}{\sqrt{R_f^2 + 2hR_f \sin \mu \cos \beta + h^2 \sin^2 \mu}} \right),$$

$$\gamma = \arctan \left( \frac{u_t}{\sqrt{s_t^2 + l_t^2}} \right) \quad (5)$$

$$= \arctan \left( \frac{h \cos \mu}{\sqrt{R_f^2 + 2hR_f \sin \mu \cos \beta + h^2 \sin^2 \mu}} \right).$$

Following from its definition, the  $\xi - \eta - \zeta$  coordinate system can be obtained by first rotating the  $s - l - u$  coordinate system around the  $u$  axis by an angle  $\sigma$  to obtain an intermediate coordinate system  $\xi - \tilde{\eta} - u$  followed by rotating the  $\xi - \tilde{\eta} - u$  coordinate system around the  $\xi$  axis by an angle  $\gamma$ . Such coordinate rotations and transformation are illustrated in Figure 3. It follows that the transformation between the  $s - l - u$  and  $\xi - \eta - \zeta$  coordinate systems is given by

$$\begin{pmatrix} \xi \\ \eta \\ \zeta \end{pmatrix} = T \begin{pmatrix} s \\ l \\ u \end{pmatrix}, \quad (6)$$

where the transformation matrix  $T$  is

$$\begin{aligned} T &= \begin{pmatrix} 1 & 0 & 0 \\ 0 & \cos \gamma & \sin \gamma \\ 0 & -\sin \gamma & \cos \gamma \end{pmatrix} \begin{pmatrix} \cos \sigma & \sin \sigma & 0 \\ -\sin \sigma & \cos \sigma & 0 \\ 0 & 0 & 1 \end{pmatrix} \quad (7) \\ &= \begin{pmatrix} \cos \sigma & \sin \sigma & 0 \\ -\sin \sigma \cos \gamma & \cos \sigma \cos \gamma & \sin \gamma \\ \sin \sigma \sin \gamma & -\cos \sigma \sin \gamma & \cos \gamma \end{pmatrix}. \end{aligned}$$

### 3. DATA REFORMATION FOR TANGENTIAL FILTERING

In conventional FDK-type algorithms, the ramp filtering is performed on detector rows and the filtering direction is parallel to the  $l$  axis on the detector surface. Motivated by the tangential filtering technique for CT without gantry tilting, we propose in this paper that the ramp filtering is performed in the tangential direction of the X-ray source trajectory of the gantry-tilted CT as shown in Figure 2. For this purpose, the projection data are reformed such that rows of the reformed projection data set are parallel to the tangential direction of the X-ray source trajectory. The reformed projection data set enables the tangential filtering technique for the conventional CT reconstruction being applied.

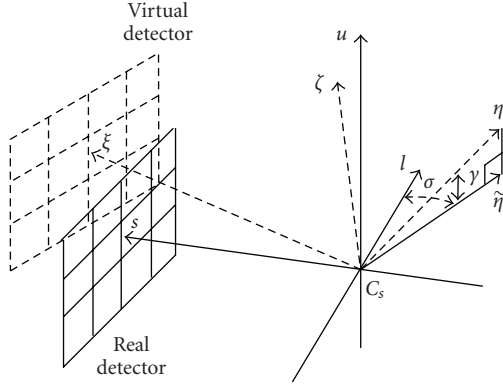


FIGURE 3: Illustration of rotation angles between  $s-l-u$  and  $\xi-\eta-\zeta$ .

The reformed data set is built up by introducing a virtual detector array surface in the tangential coordinate system  $\xi - \eta - \zeta$  and transforming the projection data from the real detector array surface in the rotating  $s - l - u$  coordinate system to the virtual detector array surface. The virtual detector array surface is placed on the plane  $\xi = (R_f + R_d)$ , as shown in Figure 4, with the rows being parallel to the  $\eta$  axis.

As shown in Figure 4, each projection ray radiates on the real detector array at the point  $((R_f + R_d), l_p, u_p)^T$  in the  $s-l-u$  coordinate also radiates on a point  $((R_f + R_d), \eta_p, \zeta_p)^T$  on the virtual detector array. Let the  $\xi - \eta - \zeta$  coordinate of the point  $((R_f + R_d), l_p, u_p)^T$  on the real detector array surface be  $(\bar{\xi}_p, \bar{\eta}_p, \bar{\zeta}_p)^T$ . The transformation from  $((R_f + R_d), l_p, u_p)^T$  to  $(\bar{\xi}_p, \bar{\eta}_p, \bar{\zeta}_p)^T$  is determined by the coordinate transformation matrix  $T$  in (7), that is,

$$\begin{pmatrix} \bar{\xi}_p \\ \bar{\eta}_p \\ \bar{\zeta}_p \end{pmatrix} = T \begin{pmatrix} (R_f + R_d) \\ l_p \\ u_p \end{pmatrix}. \quad (8)$$

In view of Figure 4, the coordinate  $(\eta_p, \zeta_p)^T$  of the virtual detector cell can be expressed, in terms of that of the real detector cell in the  $\xi - \eta - \zeta$  coordinate system, as

$$\eta_p = \frac{R_f + R_d}{\bar{\xi}_p} \bar{\eta}_p, \quad \zeta_p = \frac{R_f + R_d}{\bar{\xi}_p} \bar{\zeta}_p. \quad (9)$$

This, together with (8), can determine the coordinate of the virtual detector cell  $(\eta_p, \zeta_p)^T$  in the tangential coordinate system  $\xi - \eta - \zeta$  from a given real detector cell at  $((R_f + R_d), l_p, u_p)^T$  in the rotating coordinate system.

Let the projection datum collected from the real detector cell at  $((R_f + R_d), l_p, u_p)^T$  in the  $s - l - u$  coordinate at the projection angle  $\beta$  be denoted by  $D(\beta, l_p, u_p)$  and the corresponding projection datum on the virtual detector cell at  $((R_f + R_d), \eta_p, \zeta_p)^T$  in the  $\xi - \eta - \zeta$  coordinate by the same projection ray be denoted by  $D_v(\beta, \eta_p, \zeta_p)$ . Since  $D(\beta, l_p, u_p)$  and  $D_v(\beta, \eta_p, \zeta_p)$  are due to the same projection ray, we have

$$D_v(\beta, \eta_p, \zeta_p) = D(\beta, l_p, u_p). \quad (10)$$

This can be used to obtain the reformed projection data set following from the coordinate transform from each real

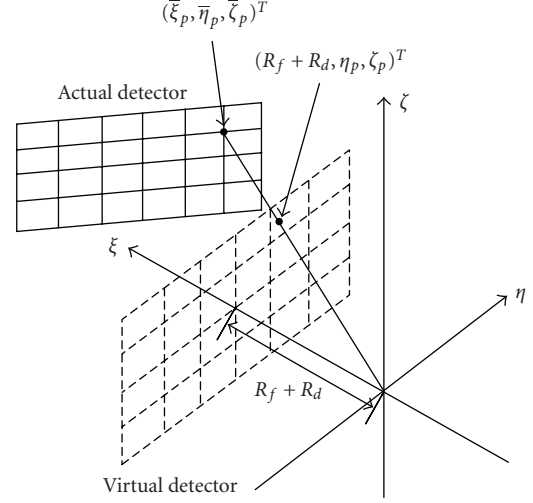


FIGURE 4: Illustration of the relationship between  $(\bar{\zeta}_p, \bar{\eta}_p, \bar{\xi}_p)^T$  and  $(R_f + R_d, \eta_p, \zeta_p)^T$  in coordinate system  $(\zeta, \eta, \xi)$ .

detector cell at  $((R_f + R_d), l_p, u_p)^T$  in the rotating coordinate system to the corresponding virtual detector cell at  $((R_f + R_d), \eta_p, \zeta_p)^T$  in the tangential coordinate system.

#### 4. RECONSTRUCTION AND INTERPOLATION

Because the gantry is tilted and final images should be on horizontal planes in the global  $x - y - z$  coordinate system, we first reconstruct images on a sequences of intermediate planes parallel to the centre plane and then interpolate them to obtain the horizontal images. The introduction of the intermediate planes effectively reduces the projection cone angle in comparison with constructing directly the horizontal planes. Let  $\psi = \{P_i : i = 1, 2, 3, \dots, n\}$  be the set of the intermediate planes and let the intersection of each tilted plane  $P_i$  and the  $z$ -axis be at point  $o_i = (0, 0, z_i)^T$ , with  $z_i = z_0 + i\Delta z$ ,  $i = 1, 2, 3, \dots, n$ , and  $\Delta z > 0$ . The projection angle for the X-ray source being at  $z_i$  in the  $z$  direction is

$$\beta_i = \beta_0 + \frac{2\pi i \Delta z}{pSM}. \quad (11)$$

And the equation for the intermediate plane  $P_i$  is

$$z = z_i + y \tan \mu. \quad (12)$$

The ramp filtering is along the  $\eta$  direction which is defined as the tangential direction of the source trajectory. Let  $g(\cdot)$  denote the ramp filter. Applying it to the reformed data set on the virtual detector array in the tangential direction of the source trajectory and performing standard cone beam weighting yields

$$\tilde{D}(\beta, \eta', \zeta) = \int \frac{R_f D_v(\beta, \eta, \zeta)}{\sqrt{\eta'^2 + R_f^2 + \zeta^2}} g(\eta' - \eta) d\eta. \quad (13)$$

Then the reconstruction formula is derived from Yan and

TABLE 1: Parameters of the clock phantom (mm).

No.	Centre	No.	Centre	No.	Centre	No.	Centre
1	(0,200,0)	7	(0,-200,-12)	13	(0,100,0)	19	(0,-100,-12)
2	(100,173.2,-2)	8	(-100,-173.2,-14)	14	(50,86.6,-2)	20	(-50,-86.6,-14)
3	(173.2,100,-4)	9	(-173.2,-100,-16)	15	(86.6,50,-4)	21	(-86.6,-50,-16)
4	(200,0,-6)	10	(-200,0,-18)	16	(100,0,-6)	22	(-100,0,-18)
5	(173.2,-100,-8)	11	(-173.2,100,-20)	17	(86.6,-50,-8)	23	(-86.6,50,-20)
6	(100,-173.2,-10)	12	(-100,173.2,-22)	18	(50,-86.6,-10)	24	(-50,86.6,-22)

Leahy's [11] paper for tangential filtering reconstruction.

$$\begin{aligned}
f_i(x, y, z) &= \frac{1}{2} \int_{\beta_i - \beta_m/2}^{\beta_i + \beta_m/2} \frac{R_f \|dC_s(\beta)/d\beta\| \tilde{D}(\beta, \eta'(\beta), \zeta(\beta))}{(x \cos \beta + y \sin \beta - R_f)^2} d\beta \\
&= \frac{1}{2} \int_{\beta_i - \beta_m/2}^{\beta_i + \beta_m/2} \frac{R_f \sqrt{R_f^2 + 2hR_f \sin \mu \cos \beta + h^2} \tilde{D}(\beta, \eta'(\beta), \zeta(\beta))}{(x \cos \beta + y \sin \beta - R_f)^2} d\beta,
\end{aligned} \tag{14}$$

where  $\|\cdot\|$  denotes Euclidean norm and  $\beta_m$  is the the length of the projection angle interval.

Given the reconstructed images of the tilted planes  $P_i$ , for  $i = 1, 2, 3, \dots, n$ , and a point  $(x, y, z)^T$  on a plane parallel to the  $x - y$  plane where the image is to be obtained by interpolation, the  $z$ -positions of the intermediate planes  $P_i$ ,  $i = 1, 2, 3, \dots, n$ , at  $(x, y)^T$  and denoted by  $z_{P_i}(x, y)$  can be determined by (12). Thus there exist two points  $(x, y, z_{P_j})^T$  and  $(x, y, z_{P_k})^T$  on two tilted planes  $P_j$  and  $P_k$ , respectively, at the upper and lower sides of  $(x, y, z)^T$ , respectively, which are closest to  $(x, y, z)^T$ . Using the obtained attenuation functions  $f_j(x, y, z_{P_j})$  and  $f_k(x, y, z_{P_k})$  for planes  $P_j$  and  $P_k$ , respectively, the interpolated attenuation function can be obtained using the following interpolation formula:

$$\begin{aligned}
f(x, y, z) &= \frac{f_j(x, y, z_{P_j}(x, y))(z_{P_k} - z)}{z_{P_k} - z_{P_j}} \\
&\quad + \frac{f_k(x, y, z_{P_k}(x, y))(z - z_{P_j})}{z_{P_k} - z_{P_j}}.
\end{aligned} \tag{15}$$

We can now summarise the proposed reconstruction procedure in the following.

- (1) Determine the  $z$  position  $z_i$ , centre of the optimal plane  $P_i$ , its centre projection angle  $\beta_i$ , and obtain the reconstruction plane using (12). For half-scan,  $\beta_m = \pi + \theta_{fan}$ .
- (2) Obtain the reformed projection data set on the virtual detector array using (9).
- (3) Reconstruct the image on the intermediate planes  $P_i$  using (14).
- (4) Obtain the horizontal images by interpolating the intermediate images.

## 5. SIMULATION

We use Turbell clock phantom and thorax phantom to evaluate the performance of the proposed algorithm. Parameters of the simulation are set to  $R_f = 570$  mm,  $R_d = 560$  mm,  $S = 1$  mm,  $p = 1.0$ , projection number per rotation  $N_p = 1024$ , number of detector cells for each row  $N_f = 800$ , detector cell width 1.5 mm, gantry-tilted angle  $\mu = 10^\circ$ . The simulated performance of the proposed algorithm is compared with two existing approximate gantry-tilted CT reconstruction algorithms, which are the gantry-tilted FDK algorithm in [3] by Hein et al. in 2003 and the gantry-tilted ASSR [2] by Kachelreiß et al in 2001.

The Turbell clock phantom is used to evaluate the proposed algorithm. The Turbell clock phantom is composed with a cylinder and two group balls. The radius of the cylinder is 240 mm and its centre is (0,0,0) and its length is 100 mm and its value is 0.4. The radius of the outer group balls is 22 mm and their values are 1.0. The radius of inner group balls is 12 mm and their values are 1.0. The positions of these balls are listed in Table 1. Results obtained from the simulation of Turbell clock phantom are shown in Figure 5, the left column is reconstructed images and the right column is the centre vertical line for reconstructed images. In Figure 5, Figure 5(a) is the image reconstructed by our proposed algorithm, Figure 5(c) is reconstructed by the gantry-tilted FDK algorithm and Figure 5(e) shows the image reconstructed by the gantry-tilted ASSR. The results demonstrate that the image reconstructed by our proposed algorithm contains fewer artifacts than that of the other two existing algorithms for gantry-tilted CT.

In the simulation of Turbell clock phantom, the centre vertical lines ( $y = 0$  mm) for the reconstructed images are also constructed and displayed by the proposed algorithm (Figure 5(b)), gantry-tilted FDK algorithm (Figure 5(d)), and gantry-tilted ASSR (Figure 5(f)), respectively. In Figure 5, dashed lines represent the original image and solid lines represent reconstructed profiles. The results show that the profile of the proposed algorithm as shown in Figure 5(b) has smaller variance than the other two results.

A thorax phantom is further simulated which is designed by referring to human thorax consisting of many important organs and often scanned in CT examination. These organs include lungs, heart, aorta, ribs, spine, sternum, and shoulders. The phantom definitions are obtained from a world phantom database FORBILD. The simulation results

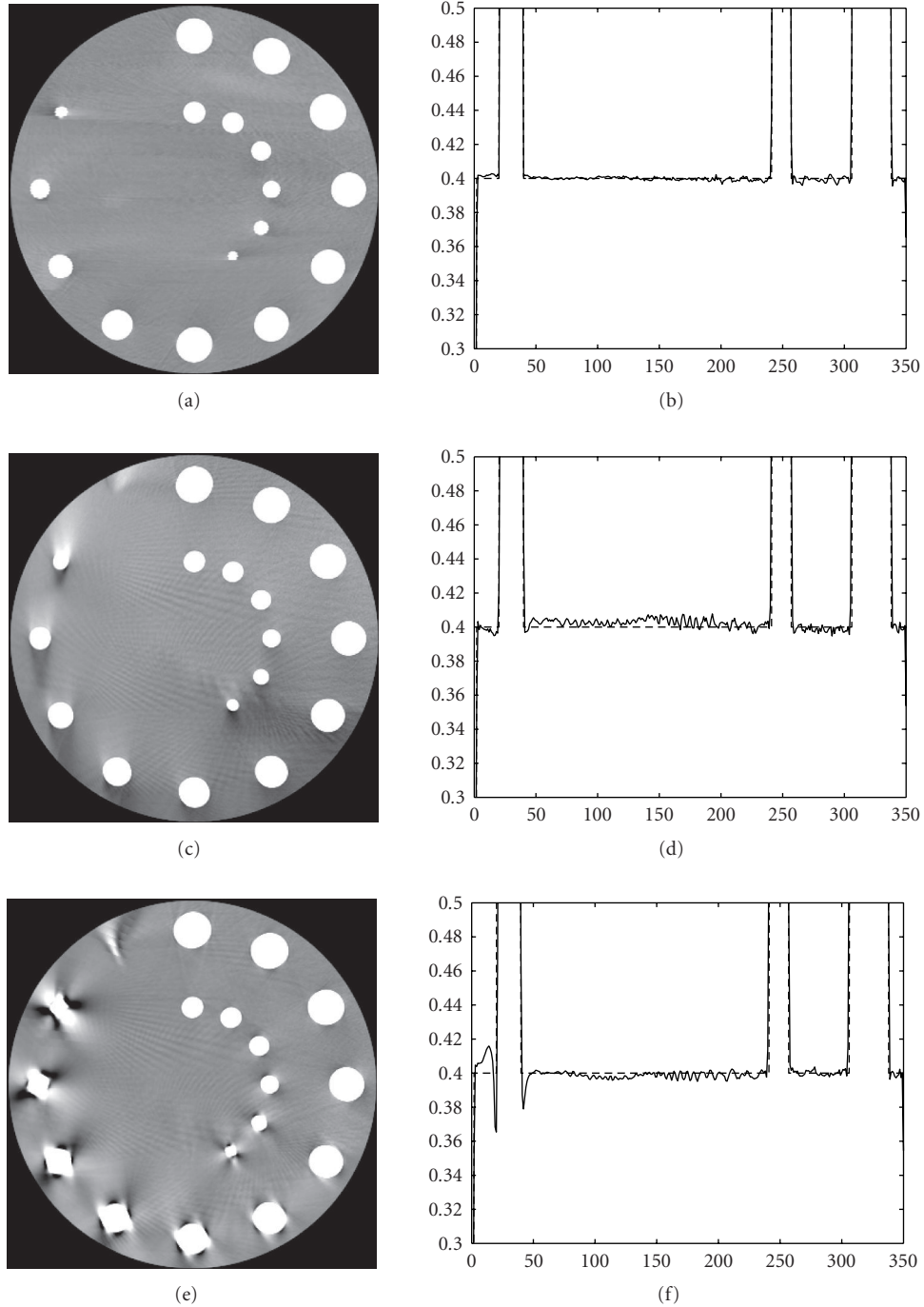


FIGURE 5: Images for the plane  $z = 0$  mm of clock phantom generated with the proposed algorithm, gantry-tilted FDK, and gantry-tilted ASSR with  $S = 1$  mm,  $p = 1.0$ ,  $M = 96$  (0.35 – 0.45).

are shown in Figure 6, where Figure 6(a) is the original thorax phantom, Figure 6(b) shows the image reconstructed by the proposed algorithm, Figure 6(c) is the image reconstructed by the gantry-tilted FDK algorithm, and Figure 6(d) is reconstructed by the gantry-tilted ASSR algorithm. The right-hand column shows zoomed reconstruction images. It is shown that there are obvious artifacts around ribs in the images reconstructed by conventional FDK algorithm and

ASSR algorithm. In contrast, the proposed algorithm provides better image quality and more accurate reconstruction.

## 6. CONCLUSION

This paper presents an approximate algorithm for gantry-tilted helical MSCT image reconstruction. It is based on the idea of filtering the 3D projection data and the filtering di-

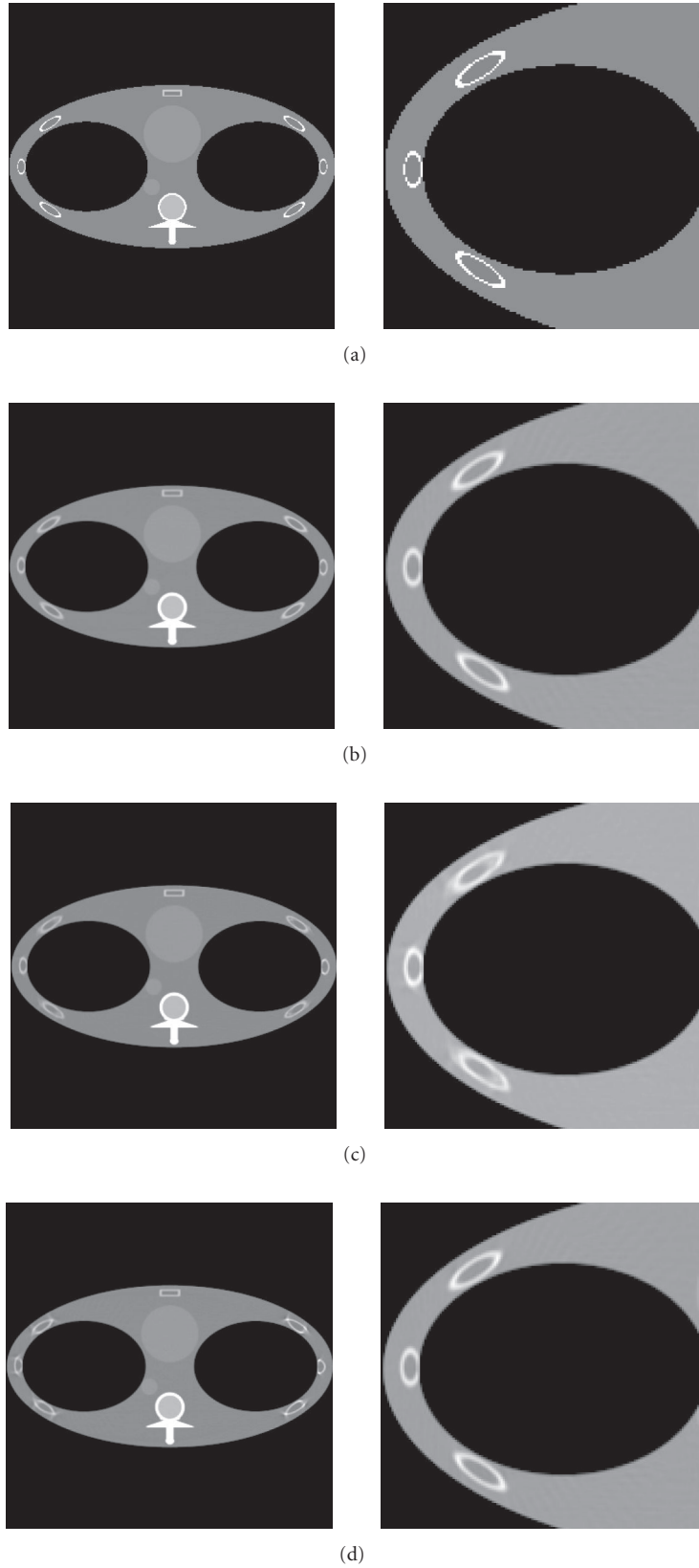


FIGURE 6: Images for the plane  $z = 0$  mm of thorax phantom generated with the proposed algorithm, gantry-tilted FDK algorithm, and gantry-tilted ASSR algorithm with  $M = 96$  (0.62-1.212).

reconstruction is varying and dependent on the CT parameters and the gantry-tilted angle. As a result, the proposed gantry-tilted reconstruction algorithm can provide more scanning flexibility in clinical CT scanning and is efficient in computation. In comparison with the existing 2D and 3D algorithms for gantry-tilted CT image reconstruction, our proposed algorithm can provide improved image quality. The performance of the proposed algorithm is evaluated with Turbell clock phantom and thorax phantom in comparison with the recent gantry-tilted FDK algorithm and gantry-tilted ASSR algorithm. The improved performance and image quality of the proposed algorithm have been shown.

## REFERENCES

- [1] J. Hsieh, "Tomographic reconstruction for tilted helical multislice CT," *IEEE Transactions on Medical Imaging*, vol. 19, no. 9, pp. 864–872, 2000.
- [2] M. Kachelrieß, T. Fuchs, S. Schaller, and W. A. Kalender, "Advanced single-slice rebinning for tilted spiral cone-beam CT," *Medical Physics*, vol. 28, no. 6, pp. 1033–1041, 2001.
- [3] I. Hein, K. Taguchi, M. D. Silver, M. Kazama, and I. Mori, "Feldkamp-based cone-beam reconstruction for gantry-tilted helical multislice CT," *Medical Physics*, vol. 30, no. 12, pp. 3233–3242, 2003.
- [4] F. Noo, M. Defrise, and H. Kudo, "General reconstruction theory for multislice X-ray computed tomography with a gantry tilt," *IEEE Transactions on Medical Imaging*, vol. 23, no. 9, pp. 1109–1116, 2004.
- [5] M. Kachelrieß, S. Schaller, and W. A. Kalender, "Advanced single-slice rebinning in cone-beam spiral CT," *Medical Physics*, vol. 27, no. 4, pp. 754–772, 2000.
- [6] I. A. Feldkamp, L. C. Davis, and J. W. Kress, "Practical cone-beam algorithm," *Journal of the Optical Society of America A*, vol. 1, no. 6, pp. 612–619, 1984.
- [7] G. Wang, T.-H. Lin, P.-C. Cheng, and D. M. Shinozaki, "General cone-beam reconstruction algorithm," *IEEE Transactions on Medical Imaging*, vol. 12, no. 3, pp. 486–496, 1993.
- [8] A. I. Katsevich, "Theoretically exact filtered backprojection-type inversion algorithm for spiral CT," *SIAM Journal on Applied Mathematics*, vol. 62, no. 6, pp. 2012–2026, 2002.
- [9] P. Grangeat, "Mathematical framework of cone beam 3D reconstruction via the first derivative of the Radon transform," in *Mathematical Methods in Tomography*, vol. 1497 of *Lecture Notes in Mathematics*, pp. 66–97, Springer, Berlin, Germany, 1992.
- [10] M. Yan and C. Zhang, "Tilted plane feldkamp type reconstruction algorithm for spiral cone beam CT," *Medical Physics*, vol. 32, no. 11, pp. 3455–3467, 2005.
- [11] X. Yan and R. M. Leahy, "Cone beam tomography with circular, elliptical and spiral orbits," *Physics in Medicine and Biology*, vol. 37, no. 3, pp. 493–506, 1992.
- [12] K. Sourbelle and W. A. Kalender, "Generalisation of Feldkamp reconstruction for clinical spiral cone beam CT," in *Proceedings of the 7th International Conference on Fully 3D Reconstruction in Radiology and Nuclear Medicine*, Saint-Malo, France, June–July 2003.
- [13] M. Kachelrieß, M. Knaup, and W. A. Kalender, "Extended parallel backprojection for standard three-dimensional and phase-correlated four-dimensional axial and spiral cone-beam CT with arbitrary pitch, arbitrary cone-angle, and 100% dose usage," *Medical Physics*, vol. 31, no. 6, pp. 1623–1641, 2004.

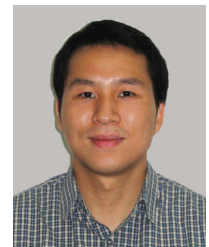
**Ming Yan** received the B.Eng. degree and the M.S. degree in automation, both from Tsinghua University, China, in 2000 and 2003, respectively. Since 2003, he has been pursuing the Ph.D. degree at the Nanyang Technological University, Singapore. His research interests include computed tomography reconstruction algorithms and medical imaging.



**Cishen Zhang** received the B.Eng. degree from Tsinghua University, China, in 1982 and the Ph.D. degree in electrical engineering from Newcastle University, Australia, in 1990. Between 1971 and 1978, he was an Electrician with Changxindian (February Seven) Locomotive manufactory, Beijing, China. He carried out research work on control systems at Delft University of Technology, The Netherlands, from 1983 to 1985. After his Ph.D. study from 1986 to 1989 at Newcastle University, he was with the Department of Electrical and Electronic Engineering at the University of Melbourne, Australia, as a Lecturer, Senior Lecturer, and Associate Professor and Reader till October 2002. He is currently with the School of Electrical and Electronic Engineering and School of Chemical and Biomedical Engineering at Nanyang Technological University, Singapore. His research interests include signal processing, medical imaging and control.



**Hongzhu Liang** received the B.Eng. degree in Xi'an Jiaotong University, China, in 2000, and the M.Eng. degree in Huazhong University of Science and Technology, China, in 2003. Since 2003 he has been with School of Electrical and Electronic Engineering, Nanyang Technological University, Singapore, as a research student pursuing the Ph.D. degree.



# FDK Half-Scan with a Heuristic Weighting Scheme on a Flat Panel Detector-Based Cone Beam CT (FDKHSCW)

Dong Yang and Ruola Ning

*Department of Imaging Sciences and Electrical & Computer Engineering, University of Rochester Medical Center, Rochester, NY 14642, USA*

Received 1 December 2005; Revised 13 June 2006; Accepted 17 June 2006

A cone beam circular half-scan scheme is becoming an attractive imaging method in cone beam CT since it improves the temporal resolution. Traditionally, the redundant data in the circular half-scan range is weighted by a central scanning plane-dependent weighting function; FDK algorithm is then applied on the weighted projection data for reconstruction. However, this scheme still suffers the attenuation coefficient drop inherited with FDK when the cone angle becomes large. A new heuristic cone beam geometry-dependent weighting scheme is proposed based on the idea that there exists less redundancy for the projection data away from the central scanning plane. The performance of FDKHSCW scheme is evaluated by comparing it to the FDK full-scan (FDKFS) scheme and the traditional FDK half-scan scheme with Parker's fan beam weighting function (FDKHSEFW). Computer simulation is employed and conducted on a 3D Shepp-Logan phantom. The result illustrates a correction of FDKHSCW to the attenuation coefficient drop in the off-scanning plane associated with FDKFS and FDKHSEFW while maintaining the same spatial resolution.

Copyright © 2006 D. Yang and R. Ning. This is an open access article distributed under the Creative Commons Attribution License, which permits unrestricted use, distribution, and reproduction in any medium, provided the original work is properly cited.

## 1. INTRODUCTION

The use of the half-scan method in cone beam CT has been a hot topic in the recent years owing to the resultant improvement in temporal resolution [1, 2]. There are currently several different types of cone beam half-scan schemes, such as FDK-based [3–5], cone beam filtered-backprojection-based (CBFBP) [6], and Grangeat-based [7]. Each scheme uses planar scanning trajectories (circular or noncircular) to conduct the half-scan scheme. Theoretically, a circular half scan can acquire approximately the same information in the radon domain as a circular full scan in terms of the first derivative radial data, as long as the reconstructed object is within a certain size based on the derivation of the Grangeat formula [8]. Even in the circular half-scanning range, redundancy still exists. The Grangeat-type half scan (GHS) maps the spatial projection data into the first derivative radial data and weights them in the radon domain. After adding missing data through linear interpolation/extrapolation in the shadow zone of the radon domain where a circular scan cannot access, a 3D radon inverse formula is used to get the reconstructed image.

Current FDK-type half-scan (FDKHSEFW) schemes for cone beam CT use Parker's [9] or other weighting coefficients

based on fan beam geometry, where same weighting coefficients are applied to all detector rows. The CBFBP algorithm manipulates the redundant projection data in the radon domain; does the half-scan reconstruction in the structure of filtered backprojection (FBP) and achieves almost the same performance as FDKHSEFW. The Grangeat-type half-scan scheme outperforms the FDK-type half-scan scheme in the correction of the off-scanning plane attenuation coefficient drop when the shadow zone is filled with the linear interpolated data. However, the spatial resolution of the reconstructed images from GHS is inferior to that of FDKHSEFW because data interpolation is less involved in FDK than in GHS [10]. Furthermore, GHS cannot handle the truncated data in the longitudinal direction. The CBFBP-related half-scan and FDKHSEFW showed obvious attenuation coefficient drop artifacts in the position of the reconstructed image farthest away from  $Z = 0$ , where  $Z$  is the rotation axis. This artifact is undesirable in practice.

In order to correct this drop problem to a certain degree as well as to maintain spatial resolution, we propose an FDK half-scan scheme with a new weighting function that fits the cone beam geometry (FDKHSCW), where the weighting function is cone beam geometry dependent. In Section 2, the FDK half-scan algorithm with the new cone beam weighting



the same redundancy.  $\omega(\beta, np)$  is the discrete weighting coefficient, calculated based on the scanning plane geometry, and can be represented by Parker's weighting function or any other weighting function as long as it can make a smooth transition between the doubly and singly sampled regions to avoid discontinuities at the borders of these regions. Undoubtedly, FDKHSFW holds all the properties that the FDK full-scan scheme does.

For cone beam projection data off the scanning plane, however, it is impossible to obtain completely doubly sam-

pled projections for a single circular orbit acquisition, even if projections are sampled over  $360^\circ$  [5]. In other words, the projection redundancy becomes less and less when projection rows get further away from the scanning plane. If the FDK algorithm had been directly applied to unweighted half-scan projection data, the reconstructed images would unavoidably have artifacts. One way to handle the weighting on the less redundancy projection row data away from scanning plane is proposed as follows:

$$\omega(\beta', np) = \begin{cases} \sin^2 \left( \frac{\pi}{4} \frac{\beta'}{\Delta' - \tan^{-1}(np/so')} \right), & 0 \leq \beta' \leq 2\Delta' - 2 \tan^{-1} \left( \frac{np}{so'} \right), \\ 1, & 2\Delta' - 2 \tan^{-1} \left( \frac{np}{so'} \right) \leq \beta' \leq \pi - 2 \tan^{-1} \left( \frac{np}{so'} \right), \\ \sin^2 \left( \frac{\pi}{4} \frac{\pi + 2\Delta' - \beta'}{\Delta' + \tan^{-1}(np/so')} \right), & \pi - 2 \tan^{-1} \left( \frac{np}{so'} \right) \leq \beta' \leq \pi + 2\Delta', \end{cases} \quad (4)$$

where

$$\begin{aligned} \beta' &= \beta \cdot \frac{1}{\sqrt{1 + m^2 \xi^2 / so^2}}, \\ so' &= \sqrt{so^2 + m^2 \xi^2}, \\ \Delta' &= \tan^{-1} \left( \frac{MO}{so'} \right). \end{aligned} \quad (5)$$

$\beta'$  is the cone-weighting angle which will be described in the next section.  $\beta'$  is dependent on the position of the row projection data in the  $Z$  direction (rotation axis).  $\Delta'$  is half of the titled fan angle that is adopted from Gullberg and Zeng [5]. Notice that when  $m$  is zero, this weighting function is actually the Parker's weighting function for fan-beam.

By incorporating the cone-beam weighting function with FDK, FDKHSCW is obtained as follows:

$$\begin{aligned} f(x, y, z) &= \int_0^{\pi+2\Delta} \frac{so^2}{(so-s)^2} \\ &\cdot \left[ \left[ \omega(\beta', np) \cdot R_\beta(np, m\xi) \right. \right. \\ &\quad \left. \left. \cdot \frac{so}{\sqrt{so^2 + m^2 \xi^2 + n^2 p^2}} \right] * h(np) \right] d\beta, \\ s &= -x \sin \beta + y \cos \beta. \end{aligned} \quad (6)$$

Please note that the projection data must be weighted prior to being filtered. Since FDKHSFW is the commonly acknowledged scheme for half-scan reconstruction, the re-

quirement for FDKHSCW is that it should produce no more artifacts than FDKHSFW.

## 2.2. Further investigation of half-scan cone beam weighting

In a circular fan-beam half-scan, there are two redundant regions in the scanning plane in terms of the projection angle  $\beta$ . Figure 2 shows that the projecting ray data acquired in region I will have a conjugate ray data in region II. In these two regions, the projection ray data is wholly or partly redundant. If half of the full fan angle is  $\Delta$  degrees, the half-scan range in terms of projection angle defined in the scanning plane is from  $0^\circ$  to  $180^\circ + 2\Delta$ . The first and second redundant region is from  $0^\circ$  to  $4\Delta$  and from  $180^\circ - 2\Delta$  to  $180^\circ + 2\Delta$ , respectively. In the traditional FDK cone-beam half-scan scheme, all the row projection data are weighted by the same set of coefficients defined in the scanning plane because the row projection data away from the scanning plane are expected to have the same redundancy as those in the scanning plane.

The proposal of the circular cone beam half-scan weighting scheme is based on the idea that the weighting coefficients should be different for projection data in different rows, and for the row projection data furthest away from the scanning plane, it should be weighted less. As of this date, we have not seen any literature discussing this issue. We found that if we use  $\beta' = \beta(1/\sqrt{1 + m^2 \xi^2 / so^2})$  as the weighting angle for different row projection data, then, the weighting coefficients in the first redundant region away from the scanning plane are not much different from those calculated in the scanning plane; the biggest difference is below 0.2 percent if  $\Delta = 15^\circ$  and the half cone angle is also  $15^\circ$ . On the other hand, when  $\beta'$  is used as the weighting

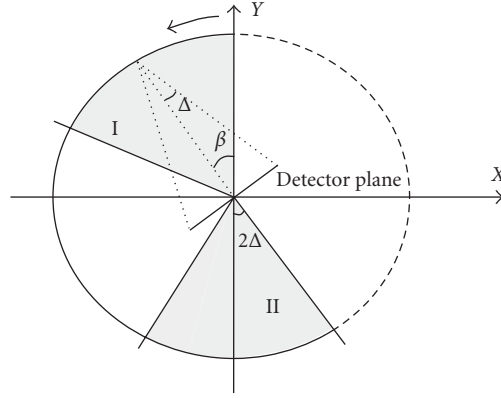


FIGURE 2: Illustration of redundant region in terms of projection angle in circular fan beam half scan.

angle in the second redundant region, the weighting coefficients away from the scanning plane behave obviously differently from those in the scanning plane and different from each other at the different rows, thus resulting in the compensation for the density drop in the place away from the scanning plane in the reconstruction image. The weighting angle  $\beta'$  has two characteristics: first, it has row position dependence that is reflected by  $m\xi$ , indirectly connected to the cone angle information; second, it has less difference from  $\beta$  when  $\beta$  is in the first redundant region than when  $\beta$  is in the second redundant region. Thus, it is beneficial to construct the cone angle dependent weighting coefficients in the second redundant region to achieve our scheme.

### 3. COMPUTER SIMULATION AND EVALUATION

In order to make computer simulation closer to the practical CBCT configuration, geometric parameters are set in terms of physical length (millimeter) rather than normalized units. The distances from the X-ray source to the iso-center of the reconstruction and to the detector are 780 mm and 1109 mm respectively. The full fan and cone angles are 30 degrees. The detector area is  $595 \times 595 \text{ mm}^2$  and has a 512 by 512 matrix size. The voxel size is  $0.816 \text{ mm}^3$ . Cartesian coordinate  $(X, Y, Z)$  is used to define the object, where  $Z$  is the rotation axis. The sampling rate of projection angle is  $0.8^\circ$  with the total number of projection images of 450 for full scan and 262 for half scan. The low contrast Shepp-Logan phantom was used (see [7] for geometrical parameters), all of its geometrical parameters are multiplied by 200 to simulate the physical length (millimeter) of the phantom.

#### 3.1. The weighting coefficients distribution comparison of FDKHSCW and FDKHSFW

Based on the scanning geometrical parameters defined above, weighting coefficient distributions associated with FDKHSFW and FDKHSCW are compared by picking up

$\beta = 46^\circ$  in the redundant region I and  $\beta = 192^\circ$ , as Figure 3 illustrates, in the redundant region II as described in Section 2.2.

#### 3.2. Reconstruction comparison of FDKHSFW and FDKHSCW

Figure 4 shows the reconstructed sagittal image from different FDK schemes at  $X = 0 \text{ mm}$  with the display window [1.005 1.05] and the profile comparison along the solid white lines in the phantom image (d). The ramp filter was used on the noise-free weighted projection data before back-projection.

#### 3.3. Simulation on quantum noise contaminated projection data

In order to test the performance of this new scheme over the quantum noise that is commonly encountered in practical CBCT data acquisition, we generated quantum noise contaminated data. X-ray with 100 kVp was selected which corresponds to an effective photon fluence of  $2.9972 \times 10^7 \text{ photons/cm}^2 \cdot \text{mR}$  [12]. The exposure level per projection was set to 4 mR, the total exposure levels for FDKFS and FDKHSCW are 1800 mR and 1048 mR, respectively. Figure 5 shows the reconstructed results under different noise levels and profile comparisons. Hamming window is used during filtering to suppress the noise.

### 4. DISCUSSIONS AND CONCLUSION

A new cone beam weighting scheme has been heuristically proposed for the FDK-based circular half-scan reconstruction (FDKHSCW) to correct the density drop artifact to a certain degree along the rotation axis inherited with original FDK algorithm for large cone angle. Computer simulation on the Shepp-Logan phantom with and without noise showed an improvement when using FDKHSCW over FDKFS and FDKHSFW in terms of the attenuation

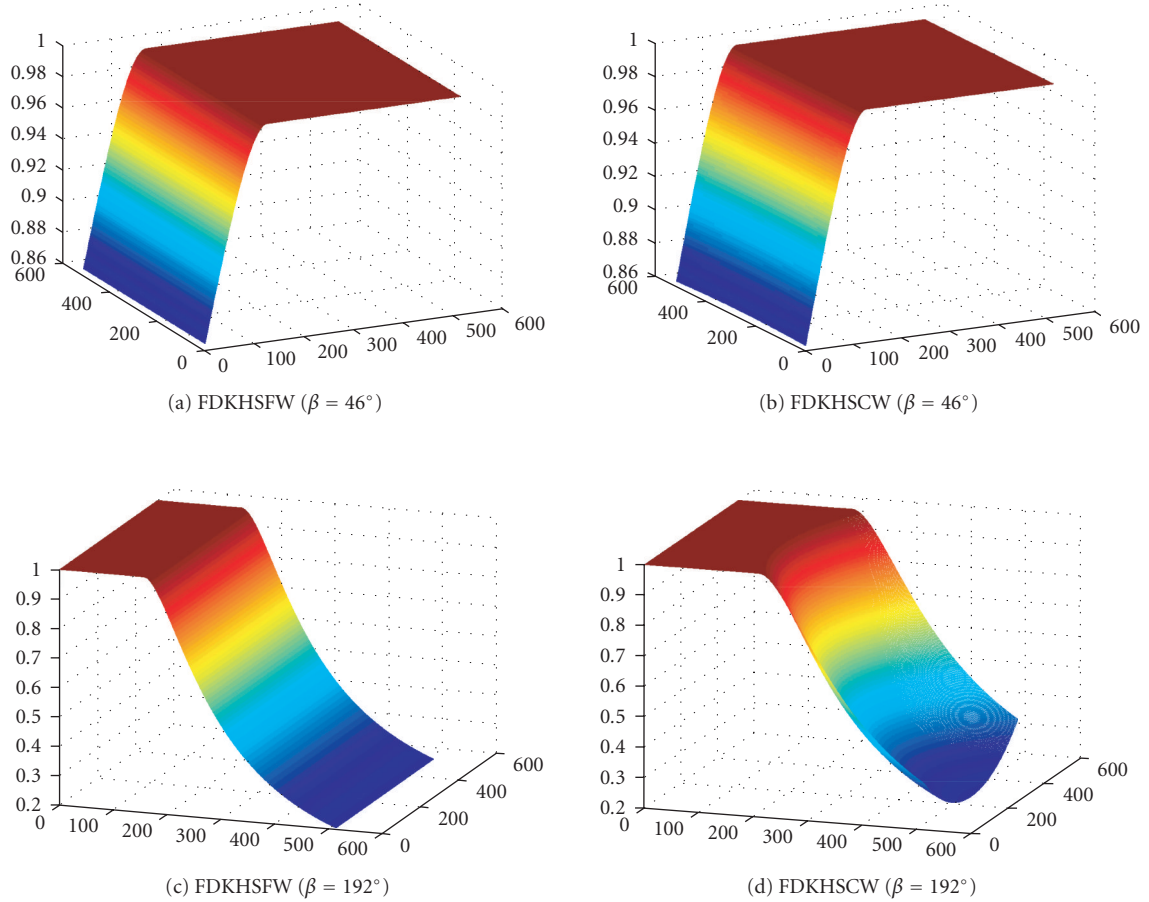


FIGURE 3: Weighting coefficients comparison between FDKHSFW and FDKHSCW when  $\beta = 46^\circ$  and when  $\beta = 192^\circ$  as shown in (a), (b) and (c), (d), respectively.

coefficient drop when the cone angle is large while maintaining the same visual image quality. FDKHSCW needs additional cone-beam weighting before filtering and only uses a scanning range of  $[\beta, 180 - \beta - 2\Delta]$ , where  $\beta$  is the starting projection angle of X-ray, and  $\Delta$  is half of the full fan angle; both of them are defined in the scanning plane. As soon as the starting angle is determined, each projection image can be processed (cone-beam weighting for half scan, pixel weighting inherited by FDK, and filtering). So, it will take less time to reconstruct an object in comparison to the full-scan scheme, a very desirable feature in practice. In addition, the half-scan scheme provides a flexibility to choose any starting point for reconstruction as long as the scanning range is guaranteed, another preferable feature for cone beam CT dynamic imaging. Based on the idea proposed by Silver [13], we can even conduct an extended half-scan scheme by making the scanning range larger than  $180 - 2\Delta$  applying this new cone beam weighting function for better noise characteristic.

Our proposed circular cone-beam half-scan weighting scheme works better for low-contrast object. We can see from our simulation on Shepp-Logan phantom that the largest compensation is within 0.03 in terms of attenuation

coefficient. We expect that FDKHSCW can show improvement in terms of intensity drop in the high-contrast phantoms, like a Defrise disk phantom. Yet, it is not as promising as in the low-contrast phantom.

Other proposed modified FDK methods called T-FDK and FDK-SLANT [14, 15] also corrected the attenuation coefficient drop to some extent along the rotation axis inherited in FDK with a larger cone angle. There is a difference between these methods and FDKHSCW. Although the results of these methods showed similar correction to FDKHSCW, FDK-SLANT and T-FDK need to be parallel rebinned from cone beam data. That means the filtering portion would not start until the whole set of data acquisition and parallel resorting procedures are completed and then followed by backprojection for image reconstruction. FDKHSCW possess the advantage that once a 2D projection data is acquired, the filtering portion can start and be immediately followed by backprojection. As long as the gantry speed and readout rate is high enough, this scheme can provide almost real time monitoring when continuous dynamic imaging is conducted. Wang [16] developed a weighting scheme for cone beam full circular-scan

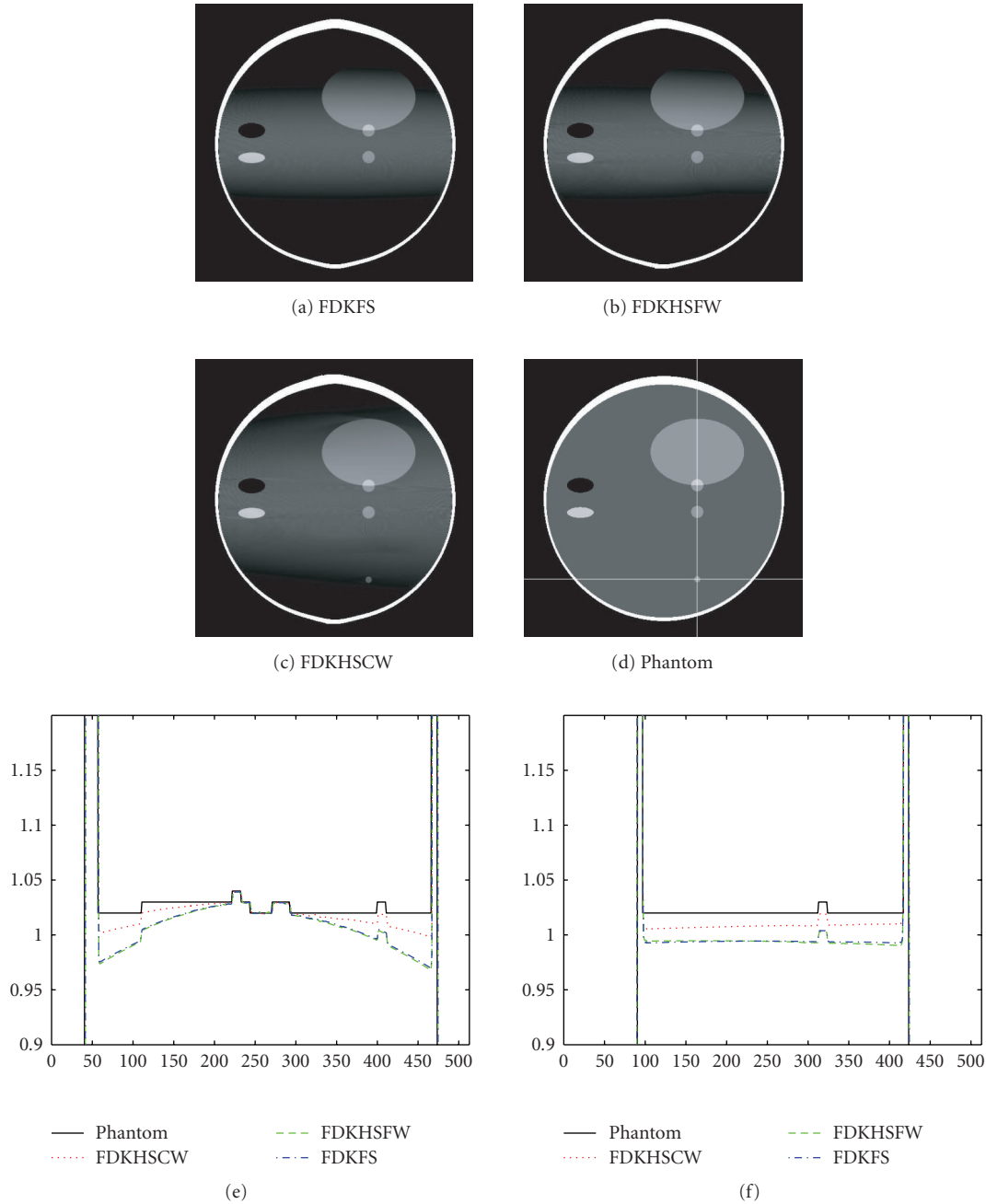


FIGURE 4: Reconstructed sagittal image from different FDK schemes at  $X = 0$  mm and respective line profile comparison in (e) and (f) along the solid vertical and horizontal white line shown in (d).

reconstruction on a displaced detector array without rebinning the projection data for reconstruction. As for the redundant area, our scheme can be applied to this algorithm by adjusting the weighting conditions in the scanning range.

Recently a new circular 3D weighting reconstruction algorithm [17] was proposed to reduce cone beam artifact based on the investigation on the data inconsistency between a direct ray and its conjugate rays. The basic idea is to have filtered projection data multiplied by correction coefficients

that are cone beam geometrical dependent during the back-projection. But the artifact it corrects is not what FDKHSCW tries to correct here, namely attenuation coefficient drop. However, it is worth trying to combine these two schemes for future evaluation.

In conclusion, by incorporating a new cone beam weighting scheme, a new FDK-based heuristic half-scan approximate algorithm for circular trajectory has been proposed based on flat panel detector, and the numerical simulation demonstrated its feasibility.

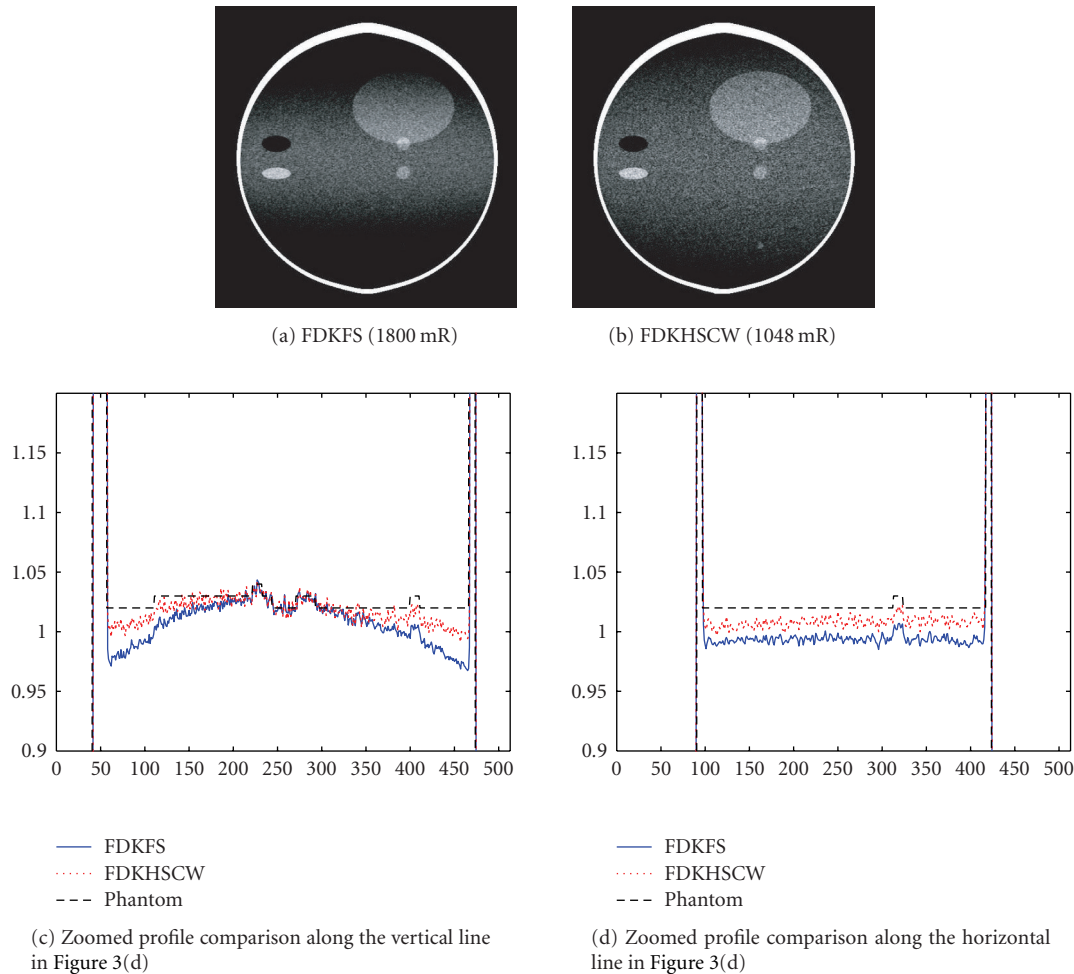


FIGURE 5: (a) FDKFS with total exposure level of 1800 mR. (b) FDKHSCW with total exposure level of 1048 mR. (c), (d) Profile comparison between FDKFS, FDKHSCW, and phantom along the solid vertical and horizontal lines in Figure 4(d).

## ACKNOWLEDGMENTS

The authors thank the anonymous reviewers for their helpful comments. This project was supported in part by NIH Grants 8 R01 EB002775, R01 9 HL078181, and 4 R33 CA94300.

## REFERENCES

- [1] Y. Liu, H. Liu, Y. Wang, and G. Wang, "Half-scan cone-beam CT fluoroscopy with multiple x-ray sources," *Medical Physics*, vol. 28, no. 7, pp. 1466–1471, 2001.
- [2] K. Taguchi, "Temporal resolution and the evaluation of candidate algorithms for four-dimensional CT," *Medical Physics*, vol. 30, no. 4, pp. 640–650, 2003.
- [3] G. Wang, Y. Liu, T. H. Lin, and P. C. Cheng, "Half-scan cone-beam x-ray microtomography formula," *Scanning*, vol. 16, no. 4, pp. 216–220, 1994.
- [4] S. Zhao and G. Wang, "Feldkamp-type cone-beam tomography in the wavelet framework," *IEEE Transactions on Medical Imaging*, vol. 19, no. 9, pp. 922–929, 2000.
- [5] G. T. Gullberg and G. L. Zeng, "A cone-beam filtered back-projection reconstruction algorithm for cardiac single photon emission computed tomography," *IEEE Transactions on Medical Imaging*, vol. 11, no. 1, pp. 91–101, 1992.
- [6] F. Noo and D. J. Heuscher, "Image reconstruction from cone-beam data on a circular short-scan," in *Medical Imaging 2002: Image Processing*, vol. 4684 of *Proceedings of SPIE*, pp. 50–59, San Diego, Calif, USA, February 2002.
- [7] S. W. Lee and G. Wang, "A Grangeat-type half-scan algorithm for cone-beam CT," *Medical Physics*, vol. 30, no. 4, pp. 689–700, 2003.
- [8] P. Grangeat, "Mathematical framework of cone beam 3D reconstruction via the first derivative of the Radon transform," in *Mathematical Methods in Tomography*, G. T. Herman, A. K. Luis, and F. Natterer, Eds., Lecture Notes in Mathematics, pp. 66–97, Springer, Berlin, Germany, 1991.
- [9] D. L. Parker, "Optimal short scan convolution reconstruction for fan beam CT," *Medical Physics*, vol. 9, no. 2, pp. 254–257, 1982.
- [10] G. Wang, C. R. Crawford, and W. A. Kalender, "Multirow detector and cone-beam spiral/helical CT," *IEEE Transactions on Medical Imaging*, vol. 19, no. 9, pp. 817–821, 2000.

- [11] I. A. Feldkamp, L. C. Davis, and J. W. Kress, "Practical cone-beam algorithm," *Journal of the Optical Society of America A*, vol. 1, no. 6, pp. 612–619, 1984.
- [12] Y. Zhang, R. Ning, D. Conover, and Y. Yu, "Image noise due to quantum fluctuations in flat-panel detector based cone-beam CT imaging," in *Medical Imaging 2005: Physics of Medical Imaging*, vol. 5745 of *Proceedings of SPIE*, pp. 656–663, San Diego, Calif, USA, February 2005.
- [13] M. D. Silver, "A method for including redundant data in computed tomography," *Medical Physics*, vol. 27, no. 4, pp. 773–774, 2000.
- [14] M. Grass, Th. Köhler, and R. Proksa, "3D cone-beam CT reconstruction for circular trajectories," *Physics in Medicine and Biology*, vol. 45, no. 2, pp. 329–347, 2000.
- [15] H. Turbell, "Cone-beam reconstruction using filtered back-projection," Linköping Studies in Science and Technology Dissertation 672, Linköping University, Linköping, Sweden, 2001.
- [16] G. Wang, "X-ray micro-CT with a displaced detector array," *Medical Physics*, vol. 29, no. 7, pp. 1634–1636, 2002.
- [17] X. Tang, J. Hsieh, A. Hagiwara, R. A. Nilsen, J.-B. Thibault, and E. Drapkin, "A three-dimensional weighted cone beam filtered backprojection (CB-FBP) algorithm for image reconstruction in volumetric CT under a circular source trajectory," *Physics in Medicine and Biology*, vol. 50, no. 16, pp. 3889–3905, 2005.

**Dong Yang** received his M.S. degree in biomedical engineering in 1998 from Chongqing University, China. He got the M.S. degree in electronic and computer engineering in 2004 from University of Rochester, USA. He is now a Ph.D. candidate in the Department of Electrical and Computer Engineering of the University of Rochester. His research work is in the flat panel-based cone beam CT reconstruction implementation and clinical application, and medical imaging processing.



**Ruola Ning** received a B.S. degree in electronic physics from Zhongshan University in China in 1982, an M.S. degree in electrical engineering in 1986, and a Ph.D. degree in electrical engineering in 1989 from the University of Utah. He is a Member of both SPIE and AAPM. Since 1989, he has been on the Faculty of the University of Rochester. He is an ABR certified medical physicist and is the author of more than 80 referred journal articles and proceedings. He is currently a Professor of imaging sciences (the formal radiology), biomedical engineering, electrical & computer engineering, radiation oncology, and oncology at the University of Rochester, where his research interests include the development of cone beam CT imaging, cone beam breast CT, cone beam CT angiography, functional cone beam CT, cone beam reconstruction algorithms, three-dimensional medical imaging, pattern recognition, and image-based explosive detection.



# Analysis of Cone-Beam Artifacts in off-Centered Circular CT for Four Reconstruction Methods

S. Valton,<sup>1,2,3,4</sup> F. Peyrin,<sup>1,2,3,4</sup> and D. Sappey-Marinier<sup>1,2,3,4</sup>

<sup>1</sup>CREATIS, UMR CNRS 5515, 69621 Villeurbanne, France

<sup>2</sup>CREATIS, U630 INSERM, 69621 Villeurbanne, France

<sup>3</sup>CREATIS, INSA-Lyon, 69621 Villeurbanne, France

<sup>4</sup>CREATIS, Université Claude Bernard-Lyon1, 69677 Bron, France

Received 1 December 2005; Revised 30 May 2006; Accepted 31 May 2006

Cone-beam (CB) acquisition is increasingly used for truly three-dimensional X-ray computerized tomography (CT). However, tomographic reconstruction from data collected along a circular trajectory with the popular Feldkamp algorithm is known to produce the so-called CB artifacts. These artifacts result from the incompleteness of the source trajectory and the resulting missing data in the Radon space increasing with the distance to the plane containing the source orbit. In the context of the development of integrated PET/CT microscanners, we introduced a novel off-centered circular CT cone-beam geometry. We proposed a generalized Feldkamp formula ( $\alpha$ -FDK) adapted to this geometry, but reconstructions suffer from increased CB artifacts. In this paper, we evaluate and compare four different reconstruction methods for correcting CB artifacts in off-centered geometry. We consider the  $\alpha$ -FDK algorithm, the shift-variant FBP method derived from the T-FDK, an FBP method based on the Grangeat formula, and an iterative algebraic method (SART). The results show that the low contrast artifacts can be efficiently corrected by the shift-variant method and the SART method to achieve good quality images at the expense of increased computation time, but the geometrical deformations are still not compensated for by these techniques.

Copyright © 2006 S. Valton et al. This is an open access article distributed under the Creative Commons Attribution License, which permits unrestricted use, distribution, and reproduction in any medium, provided the original work is properly cited.

## 1. INTRODUCTION

Tomographic reconstruction has been a very active research field for over twenty years. Early works were rather focused on the inverse problem of tomography [1], the theoretical basis of which was founded on the Radon inversion formula, while later contributions have mostly been devoted to practical reconstruction methods for specific acquisition geometries. Tomographic reconstruction methods are generally classified into two classes of reconstruction algorithms (see, e.g., [2, 3]): analytical and algebraic methods. The discretization of continuous inversion formulae leads to analytical methods while algebraic methods are based on the resolution of a linear system modeling the projection process. In algebraic reconstruction, the choice of the resolution technique results in a given algorithm (ART [4], SIRT [5], SART [6], etc.) characterized by an iteration formula which is completely independent of the acquisition geometry. In contrast, analytical methods are strongly dependent on the scanner geometry. Successive generations of scanners led to two-dimensional (2D) tomography with parallel-beam (PB) geometry, fan-beam (FB) geometry [7, 8], and today 3D

cone-beam (CB) tomography [9–11]. 3D tomography enables the reconstruction of larger (multislice) volumes with reduced acquisition duration and irradiation.

The trajectory of the X-ray source is an important feature in 3D CB tomography. In addition to simple circle, numerous trajectories such as circle plus line [12], two circles [13], set of lines [14], helix, and so forth, have been investigated but currently, most contributions deal with the circular and the helical trajectories [15, 16]. The completeness condition on the source trajectory establishes whether or not exact reconstruction can be achieved from the projection data. According to the condition due to Kirillov [17] and formulated by Tuy [18] and Smith [19], a trajectory is complete if any plane crossing the support of the object intersects the vertex path at least once. No exact reconstruction can be expected if the source trajectory does not fulfill this condition owing to the incomplete projection data set.

In regular circular CB geometry, the most commonly used reconstruction algorithm is the FDK [20] which is a generalization to 3D CB of the standard filtered backprojection (FBP) algorithm. It is clear that the circular trajectory is incomplete since a plane parallel to the source path might

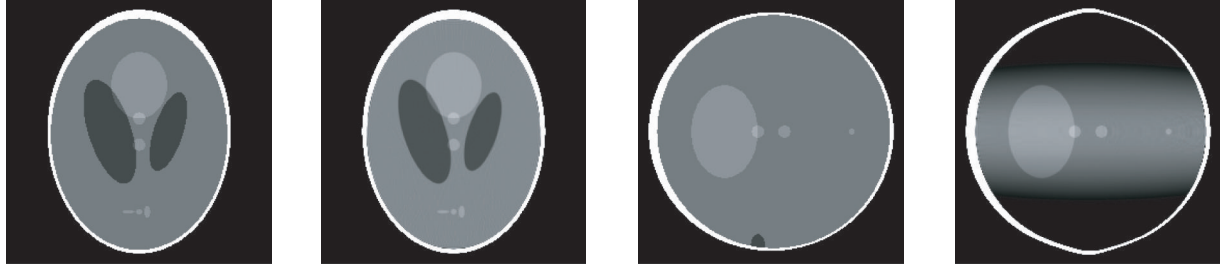


FIGURE 1: 3D Shepp-Logan phantom with total CB angle  $36^\circ$ . From left to right: horizontal mid-plane of the reference phantom, horizontal mid-plane of the reconstruction with the FDK algorithm, vertical plane of the reference phantom, and vertical plane of the FDK reconstruction.

intersect the support of the reconstructed volume while not crossing the source vertex. Reconstruction is therefore approximate except in the mid-plane (where it is equivalent to FB reconstruction). If reconstructions of good quality can be obtained with FDK for limited CB angles, artifacts rapidly increase with the distance to the mid-plane for a given focus length. Figure 1 represents the mid-plane and a vertical slice of a 3D Shepp-Logan phantom reconstructed with a total CB angle equal to  $36^\circ$ . The reconstruction suffers from two kinds of CB artifacts: drop of low contrast intensity and geometrical deformations which appear at contrast jumps along the rotation axis (here: vertical axis). In order to reduce CB artifacts, different approaches have been reported in the past few years. Grass et al. [21] proposed the T-FDK algorithm which relies on changing the ramp filtering direction through CB to parallel fan-beam (PFB) rebinning. Yu et al. [22] have improved the reconstruction resolution via shift-variant filtering. Another class of methods is based on the Grangeat formula which relates the CB projections to the derivative of the 3D Radon transform [23]. The Radon transform reconstituted from the CB projection collected along a circular trajectory forms a torus instead of a sphere. This difference, referred to as the shadow zone, corresponds to the missing data. The reconstruction obtained with zero padding of the shadow was presumed to be equivalent to FDK and therefore suffered from CB artifacts. Lee et al. showed that filling in the shadow zone by interpolation could improve reconstruction [24]. Moreover, Hu made an important contribution providing a link between the Grangeat and the FDK formulae. He established that the FDK formula only deals with the inner part of the Radon torus and proposed a method which added the contribution of the Radon data on the torus shell [25]. Yang et al. completed this approach with information on the shadow zone [26]. More empirical approaches were suggested such as a 3D weighting of the projection data before the backprojection step [23] or error-correction-based methods [27–29] which associate analytical and algebraic approaches.

We recently introduced a novel acquisition geometry for CT data which enables simultaneous acquisition of PET and CT data for small animal [30]. This concept is based on photon counting pixel X-ray detectors expected to have a very high counting rate at X-rays energy (around 50 keV) while

not stopping gamma rays (511 keV) [31]. This feature permits their placement inside a full micro-PET ring, in front of the PET crystals. However, this configuration imposes the X-ray source to be located outside the PET ring on an independently rotating system and focused on the center of the PET field of view (FOV). In this design, the X-ray source is off-centered with respect to the volume of interest (VOI) which results in the rotation of the source and the detector in two distinct planes. We first proposed a generalized formula called  $\alpha$ -FDK [30] allowing for this topology, which comes down to standard FDK when applied to the simple circular geometry. However, the off-centered geometry is clearly exposed to CB artifacts since the entire volume of interest might be outside the exactly reconstructed mid-plane. The  $\alpha$ -FDK performs the reconstruction of a shifted (or not) VOI defined by the angle  $\alpha$  and partially compensates for the low-contrast attenuation via the addition of an offset to obtain the correct value in the central plane. Nevertheless, the formula produces geometrical deformations and does not suppress the ramp of the reconstructed intensity. Reconstruction results obtained on simulations with the  $\alpha$ -FDK therefore suffered from severe CB artifacts with large values of  $\alpha$  and multislice volumes.

The purpose of this paper is to evaluate four different reconstruction techniques in our specific off-centered geometry in terms of CB artifacts reduction. We consider three analytical reconstruction methods, the  $\alpha$ -FDK [30], the adaptation to our geometry of the shift-variant filtering (SVF) technique [22], and an FBP Grangeat-based (GB) formula [25]. We also evaluate an algebraic method, SART [6].

The paper is organized as follows. Section 2 gives a detailed description of the acquisition geometry. The four reconstruction methods are presented in Section 3. The reconstruction results obtained by computer simulations are presented and discussed in Section 4.

## 2. ACQUISITION GEOMETRY

The off-centered geometry parameterized by angle  $\alpha$  is depicted in Figure 2. Let  $f(x, y, z)$  be a 3D attenuation function whose support is a sphere of radius  $r$  centered on the origin  $O$  of a Cartesian coordinate system. The plane  $(O, x, y)$  is called the central plane. The X-ray source is located at a

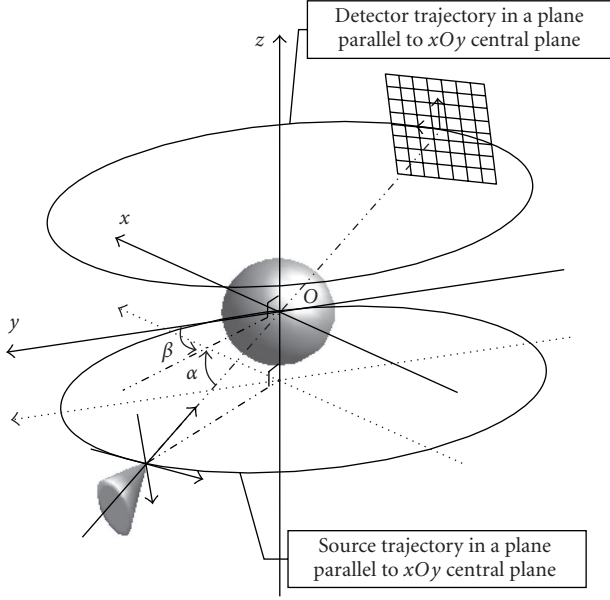


FIGURE 2: Off-centered geometry: the X-ray source (depicted by the small cone) and the detector rotate in two parallel planes, the offset of which is parameterized by angle  $\alpha$ . The position of the source at each projection is given by angle  $\beta$ .

distance  $R$  from the origin where  $R > r$  and rotates in the plane  $z = c$  where  $c \neq 0$ , called the mid-plane. The X-ray tube is oriented so that the central ray passes through  $O$ . Its position on the vertex path is parameterized by angle  $\beta$ . The acquisition geometry is characterized by  $\alpha$ , defined as the angle between the central ray and the central plane. Detector plane is perpendicular to the central ray and faces the source at a distance  $D$ . For the sake of simplicity and without loss of generality, we will consider a virtual detector whose center is on the  $z$  axis, that is,  $D = R$ . Let  $(u, \nu)$  be the coordinate system centered on the orthogonal projection of the source on the detector, where  $u$  refers to the lines of the detector ( $z$  constant) and  $\nu$  refers to the columns. Let  $p_{\alpha,\beta}(u, \nu)$  denote the 2D off-centered CB projection at angular position  $\beta$  in the off-centered geometry defined by angle  $\alpha$ .

### 3. RECONSTRUCTION METHODS

#### 3.1. $\alpha$ -FDK

We derived a modified FDK expression adapted to the parameterization of the off-centered geometry. We recall the generalized inversion  $\alpha$ -FDK formula [30]

$$f_{\alpha\text{-FDK}}(x, y, z) = \int_0^{2\pi} \frac{1}{U^2} \tilde{p}_{\alpha,\beta} \left( \frac{t'}{U}, \frac{r'}{U} \right) d\beta, \quad (1)$$

where the weight  $U$  is given by

$$U = \frac{D - s'}{D} \quad (2)$$

and  $(t', s', r')$  is the coordinates system obtained by rotation of angle  $\beta$  around  $z$  axis followed by rotation of angle  $-\alpha$

around  $x$  axis so that the  $s'$  axis points toward the source. Coordinates  $t', s',$  and  $r'$  are given by

$$\begin{aligned} t' &= x \cos \beta + y \sin \beta, \\ s' &= -x \cos \alpha \sin \beta + y \cos \alpha \cos \beta - z \sin \alpha, \\ r' &= x \sin \alpha \sin \beta - y \sin \alpha \cos \beta + z \cos \alpha. \end{aligned} \quad (3)$$

The preweighting and filtering operations are given by

$$\begin{aligned} p'_{\alpha,\beta}(u, \nu) &= \frac{D}{\sqrt{D^2 + u^2 + \nu^2}} p_{\alpha,\beta}(u, \nu), \\ \tilde{p}_{\alpha,\beta}(u, \nu) &= p'_{\alpha,\beta}(u, \nu) * \frac{1}{2} h(u), \end{aligned} \quad (4)$$

where  $h$  is the ramp filter.

This formula is equivalent to the standard FDK when  $\alpha = 0$ . From a practical point of view, the  $\alpha$ -FDK offers the same advantages as FDK for implementation: filtering is made on the lines of the detector, and each projection can be processed independently making the algorithm easily parallelizable.

#### 3.2. T-FDK with shift-variant filtration

The algorithm proposed in [22] by Yu et al. for CB reconstruction is an FBP applied to parallel fan-beam data. The CB-to-PFB rebinning is performed via the Fourier space. The rebinned PFB projections are given by  $\text{pr}'_{\varphi}(u, \nu)$  where angle  $\varphi$  satisfies

$$\varphi = \beta - \arctan \left( \frac{u}{R} \right). \quad (5)$$

The projections obtained after the CB-to-PFB rebinning operation lie on a curved virtual detector where the native coordinates are no longer equispaced. This step is thus followed by a vertical rebinning to obtain vertically equispaced  $\text{pr}_{\varphi}(u, \nu e)$  projection data where

$$\nu e = \nu \frac{R^2}{R^2 + u^2}. \quad (6)$$

Then, a similar horizontal rebinning is performed in [21] while Yu et al. alternatively propose to modify the 1D ramp filter. A shift-variant filtering of the nonrebinned data is applied instead of the ramp filtering of the equispaced data. Let  $\xi$  be the equispaced coordinate along the detector lines given by

$$\xi = \frac{uR}{\sqrt{u^2 + R^2}}. \quad (7)$$

Then one obtains via a changing variable the following reconstruction formula:

$$\begin{aligned} f_{\text{SVF}}(x, y, z) &= \frac{1}{2} \int_0^{2\pi} d\varphi \int_{-u_{\max}}^{u_{\max}} D(u) \text{pr}_{\varphi}(u, \nu e_0) G(u_0, u) h(u_0 - u) du, \end{aligned} \quad (8)$$

where

$$ve_0(x, y, z, \varphi) = \frac{z\sqrt{R^2 - \xi^2}}{\sqrt{R^2 - \xi^2 + x \sin \varphi - y \cos \varphi}},$$

$$D(u) = \frac{d\xi}{du} = \left( \frac{R}{\sqrt{u^2 + R^2}} \right)^3, \quad (9)$$

$$G(u_0, u) = \left( \frac{u_0 - u}{Ru_0/\sqrt{R^2 + u_0^2} - Ru/\sqrt{R^2 + u^2}} \right).$$

This formula has two drawbacks compared to the standard FDK:

- (i) the CB-to-PFB rebinning requires all the CB projections which is memory and time consuming,
- (ii) the shift-variant filter kernel prevents from implementing the filtering in the Fourier space.

### 3.3. Radon-based method (RB)

The 3D Radon transform  $\mathfrak{R}f(\rho, \vec{n})$  of the function  $f$  corresponds to its integral along the plane of normal vector  $\vec{n}$  at a distance  $\rho$  from the origin:

$$\mathfrak{R}f(\rho, \vec{n}) = \iint_{M \in P(\rho, \vec{n})} f(M) dM. \quad (10)$$

Hu showed in [25] that the function  $f_{RB}$  reconstructed with the Grangeat formula based on the 3D Radon inversion could be expressed as the sum of three terms:

$$f_{RB} = f_{M0} + f_{M1} + f_N. \quad (11)$$

The first term corresponds to the FDK formula, or the inversion of the 3D Radon data contained into the torus. The second term can be interpreted as the inversion of the 3D Radon data situated on the torus shell and was expressed as a filtered backprojection. The last term is a contribution from the shadow zone which is set to 0 in Hu's method.

The first term is thus given by

$$f_{M0} = f_{FDK}. \quad (12)$$

The second term is expressed as

$$f_{M1}(x, y, z) = -\frac{1}{4\pi^2} \int_0^{2\pi} \frac{z}{R + x \sin \beta - y \cos \beta} \frac{\partial \sigma_\beta(\nu)}{\partial \nu} d\beta, \quad (13)$$

where the Radon data on the circle which describes the radon shell is obtained by

$$\sigma_\beta(\nu) \int_{u_{\min}}^{u_{\max}} p'_\beta(u, \nu) du, \quad (14)$$

where the preponderate projection  $p'_\beta$  is given by (4) with  $p'_\beta = p'_{\alpha=0, \beta}$ .

It is important to note that both the RB and the SVF methods are given for standard trajectory. We therefore performed reconstructions with these methods by considering a shifted VOI to account for the off-centered geometry without modifying the algorithms.

### 3.4. SART

Algebraic methods are based on a discrete modeling of the reconstruction problem. The 3D attenuation function is represented by an  $N$ -element vector  $\mathbf{F}$  and for each  $\beta$ , the projections by an  $M$ -element vector  $\mathbf{P}_{\alpha\beta}$  obtained by the following matrices product:

$$\mathbf{P}_{\alpha\beta} = \mathbf{R}_{\alpha\beta} \mathbf{F}, \quad (15)$$

where  $\mathbf{R}_{\alpha\beta}$  is the  $M \times N$  matrix describing the projection process. The purpose is to find  $\mathbf{F}$ , given projections  $\mathbf{P}_{\alpha\beta}$  for  $\beta$  describing a discrete set of angles. The solution  $\mathbf{F}$  is then approached by iterative corrections of the volume  $\mathbf{F}^k$ . The algorithm we implemented is the SART (simultaneous algebraic reconstruction technique) and adopts the following scheme.

For each cycle,

- (i) for each projection, the following is required:

- (1) estimation of the projection of the reconstructed volume  $F^k$ ,
- (2) difference between real projection and estimated projection,
- (3) normalization of the error,
- (4) backprojection of the error.

This algorithm is summarized by the iteration formula

$$F_n^{k+1} = F_n^k + \lambda \frac{\sum_{m=1}^M ((\mathbf{P}_{\alpha\beta n} - \mathbf{R}_{\alpha\beta m} \mathbf{F}^k) / \sum_{n=1}^N \mathbf{R}_{\alpha\beta mn}) \mathbf{R}_{\alpha\beta mn}}{\sum_{m=1}^M \mathbf{R}_{\alpha\beta mn}}, \quad (16)$$

where  $N$  is the number of voxels,  $M$  the number of pixels on the projections, and  $\lambda$  is a relaxation parameter. The SART algorithm was implemented on the basis of the  $\alpha$ -FDK, with minimum modifications. The projection matrices used for the backprojection were used reversely to compute the re-projections. A bilinear interpolation on the detector was used both for back- and re-projection, and the relaxation parameter  $\lambda$  was set to 1. This implementation produces numerical artifacts which were smoothed by the application of a mean filter to the final reconstructed volume.

## 4. SIMULATION RESULTS

### 4.1. Simulation parameters

Simulations were performed with the 3D Shepp-Logan phantom [32]. The acquisition system was defined with the features given in Table 1 where all distances are given in centimeters.

We tested the reconstruction with six values of angle  $\alpha$  between 0 and 0.5 radian which corresponds to  $0^\circ$  to  $28.5^\circ$ . The resulting half-CB angle varies from  $9.5^\circ$  to  $50^\circ$  which is very large compared to current values in standard CB geometry.

The four methods developed in Section 3 were implemented and results were studied on simulations. The peak-to-peak signal-to-noise ratio (PPSNR) is used for the quantitative evaluation of the reconstructions. It was computed

TABLE 1: Simulation parameters.

$R$	$D$	Detector		Volume		Number of projections
		Number of pixels	Pixel side size	Number of voxels	Voxel side size	
6	6	$256 \times 256$	0.0078125	$256 \times 256 \times 256$	0.0078125	256

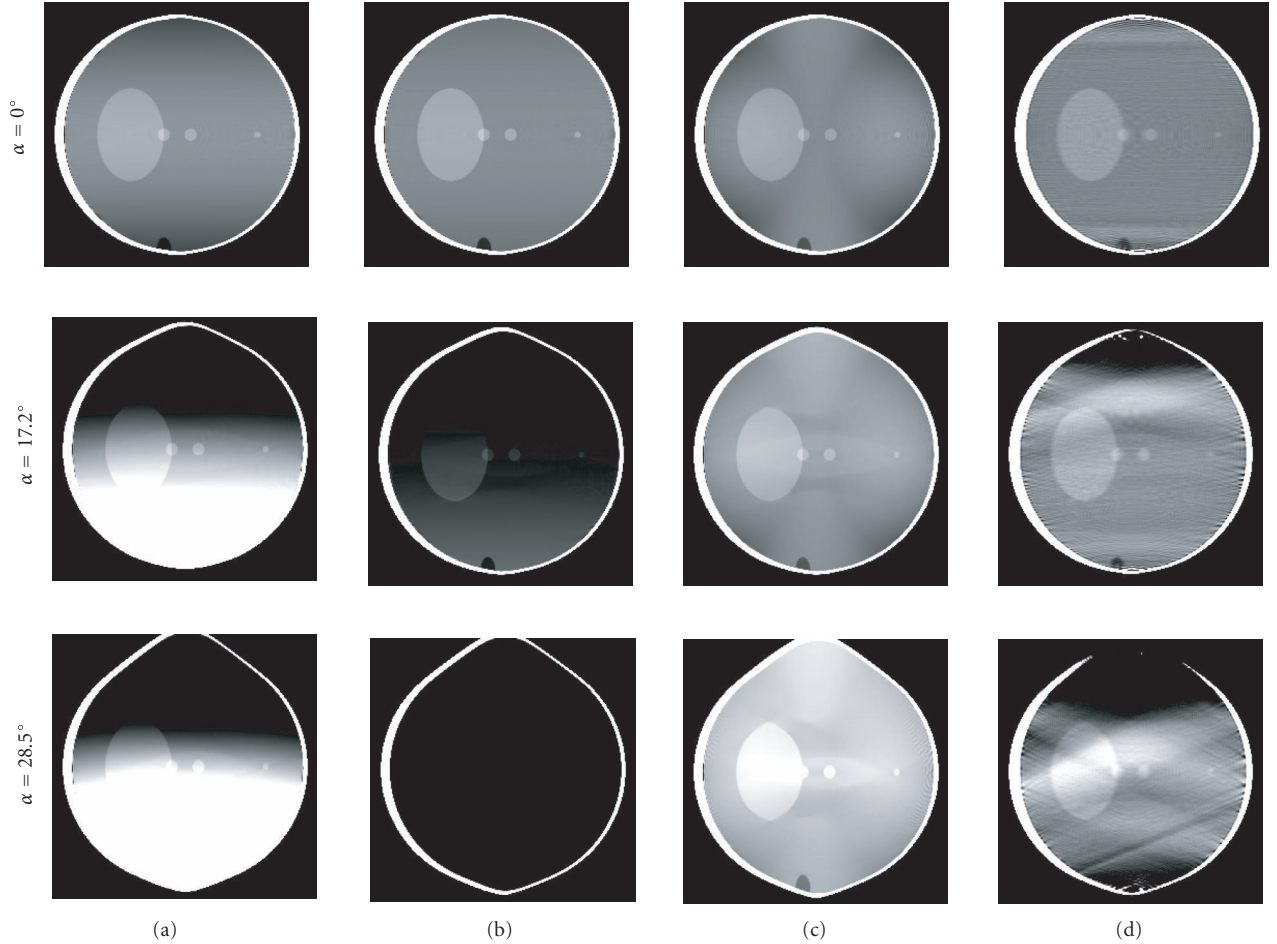


FIGURE 3: Vertical slice of the 3D Shepp-Logan phantom reconstructed with: (a)  $\alpha$ -FDK, (b) RB, (c) SVF, and (d) SART. From top to bottom, the lines correspond to 3 values of  $\alpha$  (from top to bottom):  $0^\circ$ ,  $17.2^\circ$ , and  $28.5^\circ$ . The display window is  $[0.98, 1.06]$ .

using the following expression:

$$10 * \log_{10} \left( \frac{\text{reconstructed image range}^2}{\text{MSE}} \right), \quad (17)$$

where MSE is the mean square error between the reconstructed and the reference phantom volume. In the following subsections, we present and discuss reconstruction results obtained with the three analytical methods and the SART algorithm after ten cycles.

#### 4.2. Reconstruction results

Figure 3 displays vertical planes extracted from volumes reconstructed with the different algorithms for three values of

$\alpha$ :  $0^\circ$ ,  $17.2^\circ$ , and  $28.5^\circ$ . The corresponding profiles along  $z$ -axis for  $\alpha = 28.5^\circ$  are plotted in Figure 4.

As expected, the volumes reconstructed with  $\alpha$ -FDK (Figure 3(a)) show two kinds of asymmetrical artifacts for  $\alpha \neq 0$ : vertical geometrical deformations and drop of low-contrast intensity. The vertical profiles displayed in Figure 4 include the result obtained with the standard FDK and reveal an offset between the two formulae. The RB algorithm (Figure 3(b)) partially compensates for the intensity drop but since no offset is used, the reconstructed intensity stays below the result of the  $\alpha$ -FDK (Figure 4). In Figure 3, the result with  $\alpha = 28.5^\circ$  appears dark because the same grey level window was used for comparison between the different reconstructions. The SVF algorithm (Figure 3(c)) better compensates

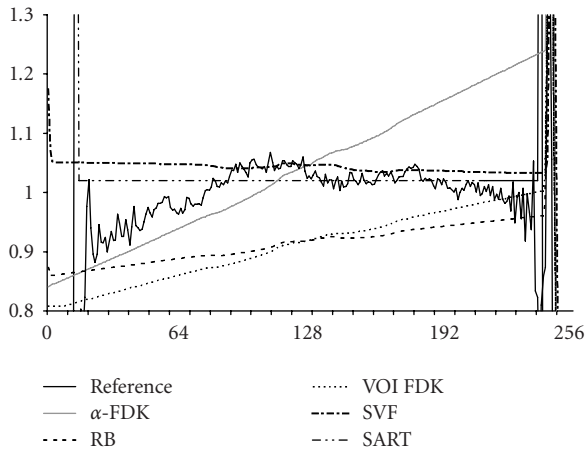


FIGURE 4: Vertical profile plot of the reconstructed Shepp-Logan at  $\alpha = 28.5^\circ$ .

for the intensity drop but the vertical elongation remains. The results obtained with standard SART after 10 cycles displayed in Figure 3(d) show that the intensity drop is only partially compensated for while the elongation is slightly corrected. The PPSNRs reported in Table 2 indicate that, quantitatively, the best reconstruction is obtained with the algebraic algorithm.

### 4.3. Discussion

In standard circular trajectory, CB artifacts correction is already a challenge since those artifacts come from the ill-conditioning of the inverse tomographic problem. In off-centered geometry, this problem is worse since the CB angle is more important and the VOI is asymmetrical with respect to the exactly reconstructed mid-plane.

The  $\alpha$ -FDK provides a practical formula adapted to the parameterization by the angle  $\alpha$  of the off-centered geometry while preserving the rapidity and simplicity of the standard formulation. It compensates for the low-contrast drop by adding an offset to the reconstructed value. However, since it does not suppress the increase of the drop with the distance to the mid-plane, this compensation is fully valuable only for a small volume around the central plane of the VOI.

The RB method reduces the CB artifacts in standard circular geometry but the correction is weak. In off-centered geometry, the  $\alpha$ -FDK outperforms the RB method when  $\alpha$  is large. In addition, the method presented by Hu takes 20% more time than the  $\alpha$ -FDK.

Concerning the SVF method, the simulation results presented above show that the intensity drop is well corrected by this method which, however, does not deal with the geometrical deformations. We can notice in Table 2 that the PPSNR is slightly inferior to that obtained with the  $\alpha$ -FDK until  $\alpha = 28.5^\circ$ . We presume that this difference is due to the numerical errors introduced by the different rebinning operations. Given the supplementary rebinning step and the shift-variant filtering, this algorithm is more time and memory

consuming than the  $\alpha$ -FDK. Besides, the rebinning step prevents from starting the reconstruction before the end of the acquisitions. To conclude, reconstructions obtained with the SVF algorithm are better than those obtained with the  $\alpha$ -FDK, but the computation time is twice as long. The choice of the optimal reconstruction method thus depends on the constraints of the application. We have seen that the reconstruction obtained with the  $\alpha$ -FDK for a volume made of a limited number of slices is acceptable. Therefore, in the perspective of a bimodal scanner, it might be interesting to prefer this simple algorithm if the axial FOV of microPET scanners is limited to few slices, depending on the number of detector rings.

Our implementation of the SART algorithm produces numerical noise resulting from the model of forward projection and the value of the relaxation factor. This high-frequency noise appears very clearly in the picture if no mean filtering is applied because of the narrow grey level display window. In contrast, it has minor effects on the PPSNR thanks to its low amplitude and MSE. The high PPSNR compared to the other methods is related to the algebraic nature of the SART which minimizes a numerical error, namely, the difference between the real and the estimated projection. The profile plot in Figure 4 shows that the correction of intensity drop is less efficient than with the SVF method, but a close look at the right end of the graph points out that the elongation is slightly corrected by this algebraic reconstruction. Nevertheless, we think that this minor improvement is not worth the additional time expense needed to perform 10 cycles of the algorithm.

To our knowledge, no correction method compensates for the geometrical deformations due to the large CB angle. Actually, no clear mention of this kind of artifacts is made in the literature dealing with CB artifact since they clearly appear only with very large values of the CB angle. We believe that this aspect needs to be addressed in future works concerning CB artifacts reduction and that the correction of the elongation should, at least partially, compensate for the low-contrast drop.

## 5. CONCLUSION

In this paper, a comparison between the results obtained with four different reconstruction techniques on data simulated with an off-centered CB circular acquisition geometry was presented. Since this geometry increases the proportion of missing data compared to the standard circular trajectory, the CB artifacts correction methods developed for the standard case need to be reinvestigated. On the one hand, the  $\alpha$ -FDK reconstruction algorithm that we derived in a previous work produces strong CB artifacts, but a good correction is obtained in the planes closed to the VOI central plane, without additional time expense. On the other hand, the intensity drop is corrected by the RB algorithm, but not sufficiently enough, by the SART and even better by the SVF algorithm in return for a certain time expense. The preferable method therefore depends on the application, in terms of computation time and accuracy needs. Generally speaking, the SVF is

TABLE 2: Signal-to-noise ratio in dB obtained with the four reconstruction methods for increasing values of  $\alpha$ .

Angle $\alpha$	0°	5.7°	11.5°	17.2°	22.9°	28.5°
$\alpha$ -FDK	27.03	26.83	26.34	25.53	24.40	23.06
RB	26.89	26.75	25.89	24.99	24.32	22.72
SVF	26.29	26.29	25.65	24.94	24.37	23.08
SART	30.73	30.57	30.16	29.42	28.42	27.15

preferable to the SART owing to the expensive computation time of the algebraic method, and to the  $\alpha$ -FDK thanks to the attenuation correction. For limited number of slices and important value of  $\alpha$ , the  $\alpha$ -FDK gives better results than the RB method and can be used instead of SVF for its rapidity. Nonetheless, the geometrical deformations could not be efficiently corrected. Further research is therefore necessary to address this complicated problem inherent to CT.

## REFERENCES

- [1] G. T. Herman, *Image Reconstruction from Projections*, chapter 14, Academic Press, New York, NY, USA, 1980.
- [2] F. Natterer, "The Mathematics of Computerized Tomography," John Wiley & sons, Chichester, NY, USA, 1986.
- [3] A. C. Kak and M. Slaney, *Principles of Computerized Tomographic Imaging*, IEEE Press, New York, NY, USA, 1987.
- [4] R. Gordon, R. Bender, and G. T. Herman, "Algebraic reconstruction techniques (ART) for three-dimensional electron microscopy and x-ray photography," *Journal of Theoretical Biology*, vol. 29, no. 3, pp. 471–481, 1970.
- [5] P. Gilbert, "Iterative methods for the three-dimensional reconstruction of an object from projections," *Journal of Theoretical Biology*, vol. 36, no. 1, pp. 105–117, 1972.
- [6] A. H. Andersen and A. C. Kak, "Simultaneous algebraic reconstruction technique (SART): a superior implementation of the art algorithm," *Ultrasonic Imaging*, vol. 6, no. 1, pp. 81–94, 1984.
- [7] G. T. Herman, A. V. A. Lakshminarayanan, and A. Narpstek, "Convolution reconstruction techniques for divergent beams," *Computers in Biology and Medicine*, vol. 6, no. 4, pp. 259–271, 1976.
- [8] G. T. Gullberg, "The reconstruction of Fan Beam Data by filtering the back-projection," *Computer Graphics and Image Processing*, vol. 10, no. 1, pp. 30–47, 1979.
- [9] C. Hamaker, K. T. Smith, D. C. Solmon, and S. L. Wagner, "The divergent beam X-ray transform," *Rocky Mountain Journal of Mathematics*, vol. 10, pp. 253–283, 1980.
- [10] F. Peyrin, "The generalized back-projection theorem for cone-beam projection data," *IEEE Transactions on Nuclear Science*, vol. 32, pp. 1512–1219, 1985.
- [11] B. D. Smith, "Cone-beam tomography. Recent advances and a tutorial review," *Optical Engineering*, vol. 29, no. 5, pp. 524–534, 1990.
- [12] G. L. Zeng and G. T. Gullberg, "A cone-beam tomography algorithm for orthogonal circle-and-line orbit," *Physics in Medicine and Biology*, vol. 37, no. 3, pp. 563–577, 1992.
- [13] H. Kudo and T. Saito, "Fast and stable cone-beam filtered backprojection method for non-planar orbits," *Physics in Medicine and Biology*, vol. 43, no. 4, pp. 747–760, 1998.
- [14] G. Wang, T.-H. Lin, P. Cheng, and D. M. Shinozaki, "A general cone-beam reconstruction algorithm," *IEEE Transactions on Medical Imaging*, vol. 12, no. 3, pp. 486–496, 1993.
- [15] A. Katsevich, "Theoretically exact filtered backprojection-type inversion algorithm for spiral CT," *SIAM Journal on Applied Mathematics*, vol. 62, no. 6, pp. 2012–2026, 2002.
- [16] H. Kudo, T. Rodet, F. Noo, and M. Defrise, "Exact and approximate algorithms for helical cone-beam CT," *Physics in Medicine and Biology*, vol. 49, no. 13, pp. 2913–2931, 2004.
- [17] A. A. Kirillov, "On a problem of IM Gel'fand," *Soviet Mathematics Doklady*, vol. 2, pp. 268–269, 1961, English Translation.
- [18] H. K. Tuy, "An inversion formula for cone-beam reconstruction," *SIAM Journal on Applied Mathematics*, vol. 43, no. 3–4, pp. 546–552, 1983.
- [19] B. D. Smith, "Cone-beam convolution formula," *Computers in Biology and Medicine*, vol. 13, no. 2, pp. 81–87, 1983.
- [20] L. A. Feldkamp, L. C. Davis, and J. W. Kress, "Practical cone-beam algorithm," *Journal of the Optical Society of America A: Optics and Image Science, and Vision*, vol. 1, no. 6, pp. 612–619, 1984.
- [21] M. Grass, Th. Köhler, and R. Proksa, "3D cone-beam CT reconstruction for circular trajectories," *Physics in Medicine and Biology*, vol. 45, no. 2, pp. 329–347, 2000.
- [22] L. Yu, X. Pan, and C. A. Pelizzari, "Image reconstruction with a shift-variant filtration in circular cone-beam CT," *International Journal of Imaging Systems and Technology*, vol. 14, no. 5, pp. 213–221, 2004.
- [23] P. Grangeat, "Mathematical framework of cone-beam 3D reconstruction via the first derivative of the Radon transform," in *Mathematical Methods in Tomography*, G. T. Herman, A. K. Louis, and F. Natterer, Eds., Lecture Notes in Mathematics, pp. 66–97, Springer, New York, NY, USA, 1991.
- [24] S. W. Lee, G. Cho, and G. Wang, "Artifacts associated with implementation of the Grangeat formula," *Medical Physics*, vol. 29, no. 12, pp. 2871–2880, 2002.
- [25] H. Hu, "An improved cone-beam reconstruction algorithm for the circular orbit," *Scanning*, vol. 18, pp. 572–581, 1996.
- [26] H. Yang, M. Li, K. Koizumi, and H. Kudo, "A FBP-type cone-beam reconstruction algorithm with Radon space interpolation ability for axially truncated data from a circular orbit," in *Proceedings of the 8th International Conference on Fully 3D Reconstruction in Radiology and Nuclear Medicine*, pp. 401–404, Salt Lake City, Utah, USA, July 2005.
- [27] J. Hsieh, "A practical cone-beam artifact correction algorithm," in *Proceedings of the IEEE Nuclear Science Symposium Conference Record (NSS '00)*, vol. 2, pp. 15/71–15/74, Lyon, France, October 2000.
- [28] K. Zeng, Z. Chen, L. Zhang, and G. Wang, "A half-scan error reduction based algorithm for cone-beam CT," *Journal of X-Ray Science and Technology*, vol. 12, no. 2, pp. 73–82, 2004.
- [29] K. Zeng, Z. Chen, L. Zhang, and G. Wang, "An error-reduction-based algorithm for cone-beam computed tomography," *Medical Physics*, vol. 31, no. 12, pp. 3206–3212, 2004.
- [30] S. Valton, F. Peyrin, and D. Sappey-Marini er, "Generalization of 3D tomographic reconstruction algorithm FDK for an off-centred geometry," in *Proceedings of the IEEE International*

*Conference on Image Processing (ICIP '05)*, vol. 3, pp. 620–623, Genova, Italy, September 2005.

- [31] P. Delpierre, S. Basolo, J. F. Berar, et al., “Pixscan: pixel detector CT-scanner for small animal imaging,” in *Proceedings of the IEEE Nuclear Science Symposium Conference Record (NSS '05)*, vol. 4, pp. 2381–2385, San Juan, Puerto Rico, USA, October 2005.
- [32] C. Axelsson, *Direct Fourier methods in 3D-reconstruction from cone-beam data*, Ph.D. thesis, Department of Electrical Engineering, Linköping University, Linköping, Sweden, 1994, p. 123.

**S. Valton** was born in France in 1982. She received her M.S. degree in computer science from the University Jean Monnet in Saint Etienne and her Engineer degree from ISTASE, both in France in 2004. She is currently a Ph.D. student at the research center CREATIS, INSA-Lyon. Her research interest includes tomographic reconstruction.



**F. Peyrin** received her Doctorate degree in computer science in 1982, and her “Docteur ès Sciences” degree, both from the University of Lyon and the National Institute of Applied Sciences (INSA-Lyon), France, respectively, in 1982 and 1990. Since 1981, she has been a Researcher in the CREATIS Laboratory at INSA-Lyon. Her research interests include 3D imaging techniques particularly in X-ray tomography, 3D image analysis, and wavelet-based methods. She is now Director of Research at INSERM and leads a group on “3D bone architecture analysis” in the laboratory, and she is currently a Scientific Collaborator at the ESRF, Grenoble, France.



**D. Sappey-Marinier** received his Doctorate degree in biomedical engineering in 1987 from the University “Claude Bernard” of Lyon, France, and performed his postdoctorate fellowship at University of California, San Francisco, for 3 years. In 1993, he became an Associate Professor at the Medical School of the University “Claude Bernard” of Lyon, France. He has been a Researcher in the CREATIS Laboratory since 2003. His research activity concerns the development of functional and metabolic imaging techniques such as magnetic resonance, PET, and CT. He is currently coordinating the group of Lyon from the Crystal Clear European collaboration on the development of the ClearPET.



# Extending Three-Dimensional Weighted Cone Beam Filtered Backprojection (CB-FBP) Algorithm for Image Reconstruction in Volumetric CT at Low Helical Pitches

Xiangyang Tang, Jiang Hsieh, Roy A. Nilsen, and Scott M. McOlash

*GE Healthcare, 3000 North Grandview Boulevard, W-1190, Waukesha, WI 53188, USA*

Received 23 December 2005; Revised 24 May 2006; Accepted 25 May 2006

A three-dimensional (3D) weighted helical cone beam filtered backprojection (CB-FBP) algorithm (namely, original 3D weighted helical CB-FBP algorithm) has already been proposed to reconstruct images from the projection data acquired along a helical trajectory in angular ranges up to  $[0, 2\pi]$ . However, an overscan is usually employed in the clinic to reconstruct tomographic images with superior noise characteristics at the most challenging anatomic structures, such as head and spine, extremity imaging, and CT angiography as well. To obtain the most achievable noise characteristics or dose efficiency in a helical overscan, we extended the 3D weighted helical CB-FBP algorithm to handle helical pitches that are smaller than 1 : 1 (namely extended 3D weighted helical CB-FBP algorithm). By decomposing a helical over scan with an angular range of  $[0, 2\pi + \Delta\beta]$  into a union of full scans corresponding to an angular range of  $[0, 2\pi]$ , the extended 3D weighted function is a summation of all 3D weighting functions corresponding to each full scan. An experimental evaluation shows that the extended 3D weighted helical CB-FBP algorithm can improve noise characteristics or dose efficiency of the 3D weighted helical CB-FBP algorithm at a helical pitch smaller than 1 : 1, while its reconstruction accuracy and computational efficiency are maintained. It is believed that, such an efficient CB reconstruction algorithm that can provide superior noise characteristics or dose efficiency at low helical pitches may find its extensive applications in CT medical imaging.

Copyright © 2006 Xiangyang Tang et al. This is an open access article distributed under the Creative Commons Attribution License, which permits unrestricted use, distribution, and reproduction in any medium, provided the original work is properly cited.

## 1. INTRODUCTION

Along with the fast evolution in theoretically exact helical cone beam (CB) reconstruction algorithms [1–5], in the recent years comes the exciting progress in theoretically approximate helical CB reconstruction algorithms [6–9]. A three-dimensional (3D) weighted helical CB filtered backprojection (CB-FBP) algorithm (namely, original 3D weighted helical CB-FBP algorithm) has been proposed to reconstruct images from the projection data acquired along a helical trajectory within an angular range up to  $[0, 2\pi]$  [6]. Except for the adoption of 3D weighting functions, the original 3D weighted helical CB-FBP algorithm is essentially similar to the FDK algorithm [10] and its extensions [11]. By using phantoms simulated by computer and scanned by CB volumetric CT scanners, the reconstruction accuracy and other properties of the original 3D weighted helical CB-FBP algorithm have been experimentally evaluated and verified. Although it is theoretically approximate, the experimental evaluation shows that, at a moderate cone angle up to  $4^\circ$  that

corresponds to a detector  $z$ -dimension of  $64 \times 0.625$  mm, the original 3D weighted helical CB-FBP algorithm reaches the reconstruction accuracy comparable to that of theoretically exact helical CB-FBP algorithms, such as the algorithm proposed by Katsevich [1, 2], and its extensions [3–5]. Moreover, other imaging performances, such as noise characteristics or dose efficiency, noise uniformity, spatial resolution, temporal resolution, computational efficiency, and robustness over clinical applications, are maintained comparable with the FDK-like CB reconstruction algorithms [10, 11].

A helical trajectory angular range of  $[0, 2\pi]$  corresponds to a full scan [12, 13], under which the normalized helical pitch is usually about 1 : 1. However, a helical overscan is usually employed in the clinic to reconstruct tomographic images with superior noise characteristics at the most challenging anatomic structures, such as head and spine, extremity imaging, and CT angiography as well. In an overscan, the projection data acquired along a helical trajectory angular range larger than  $[0, 2\pi]$  should be utilized to reconstruct an image, and the corresponding normalized

helical pitch is usually smaller than 1 : 1. Due to the  $[0, 2\pi]$  constraint in helical trajectory angular range, a direct application of the original 3D weighted helical CB-FBP algorithm in an overscan cannot make full use of available projection data, resulting in a degraded noise characteristics or dose efficiency.

To improve noise characteristics or dose efficiency in an overscan, we extended the original 3D weighted helical CB-FBP algorithm to handle helical pitches that are lower than 1 : 1 (namely extended 3D weighted helical CB-FBP algorithm). As in the original algorithm, the extended algorithm can be implemented in either the native CB geometry or the cone-parallel geometry (or wedge-geometry) that is obtained through row-wise fan-to-parallel rebinning from the native CB geometry. An experimental study is conducted in this paper to evaluate the reconstruction accuracy and noise characteristics or dose efficiency of the extended 3D weighted helical CB-FBP algorithm. Since image reconstructed in the cone-parallel geometry is of better noise uniformity and computation efficiency, the experimental evaluation is carried out in the cone-parallel geometry using the helical body phantom (HBP) [14, 15] and the Defrise phantom [16] simulated by computer. As shown below, at helical overscan, the extended 3D weighted helical CB-FBP algorithm can provide significantly improved noise characteristics or dose efficiency in comparison to the original 3D weighted helical CB-FBP algorithm, while other advantages of the original algorithm, such as reconstruction accuracy and computational efficiency, can be maintained.

## 2. MATERIALS AND METHODS

### 2.1. Native cone beam and cone-parallel geometries

The native cone beam geometry for the helical projection data acquisition and image reconstruction is shown in Figure 1(a), where  $Oxyz$  denotes the coordinate system,  $S$  the source focal spot,  $D$  the cylindrical multirow CT detector, and  $R$  the radius of the helical source trajectory.  $P(x, y, z)$  is a point within the object to be reconstructed. The ray emanating from focal spot  $S$  and passing through point  $P(x, y, z)$  is uniquely determined by its view angle  $\beta$ , fan angle  $\gamma$ , and cone angle  $\alpha$ . The helical source trajectory can be mathematically represented by

$$ST(\beta) = \left( R \sin \beta, R \cos \beta, \frac{H}{2\pi} \beta \right), \quad \beta \in [\beta_s, \beta_e], \quad (1)$$

where  $\beta_s$  and  $\beta_e$  are the starting and ending points of the helical source trajectory, respectively. Notice that view angle  $\beta$  is defined in relative to the  $y$ -axis, and  $H$  is the distance traveled by the source focal spot per rotation along the  $z$ -axis.

Through row-wise fan-to-parallel rebinning in the native CB geometry, the cone-parallel geometry for image reconstruction is attained as shown in Figure 1(b) [17–19]. The ray emanating from focal spot  $S$  and passing through point  $P(x, y, z)$  is uniquely determined by its view angle  $\beta$ , orthogonal distance  $t$  from the iso-ray (namely orthogonal iso-distance), and cone angle  $\alpha$ .

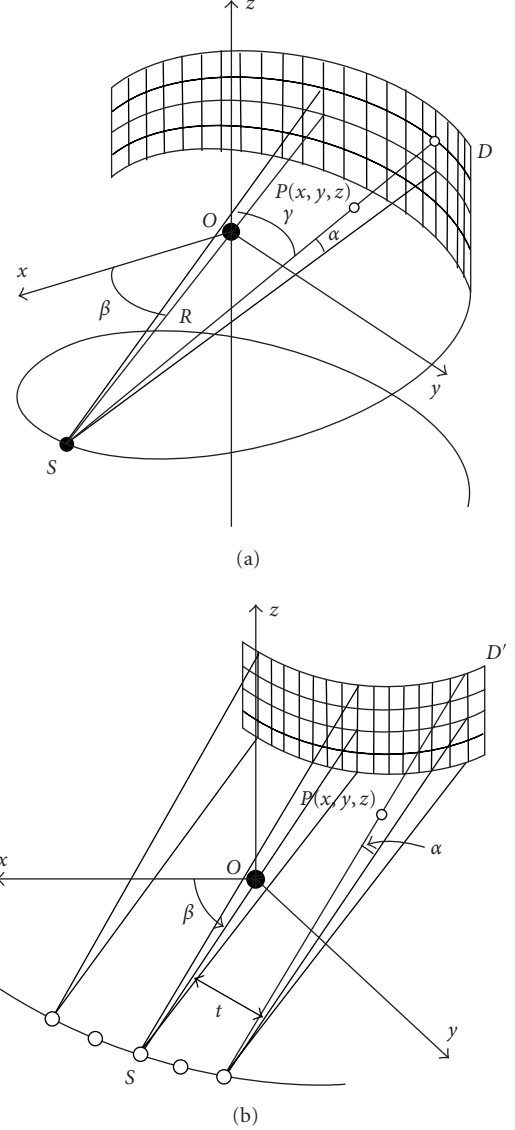


FIGURE 1: Schematic diagrams showing the geometries in which the extended 3D weighted helical CBFBP reconstruction algorithm is derived: (a) the native CB geometry; (b) the cone-parallel geometry.

### 2.2. 3D weighted CB-FBP reconstruction algorithm

In the cone-parallel geometry shown in Figure 1(b), the original 3D weighted helical CB-FBP reconstruction algorithm for a full scan is [6]

$$\tilde{f}(x, y, z) = \frac{1}{2} \int_{\beta_0 - \pi}^{\beta_0 + \pi} \frac{R}{\sqrt{R^2 + Z^2(x, y, z)}} w_{3d}(\alpha, \beta, t) \tilde{s}(\alpha, \beta, t) d\beta, \quad (2)$$

$$\tilde{s}(\alpha, \beta, t) = s(\alpha, \beta, t) \otimes q(t), \quad (3)$$

where  $Z(x, y, z)$  is the projected  $z$ -coordinate of point  $P(x, y, z)$  onto detector  $D$ , and  $q(t)$  is the conventional

ramp filter kernel in parallel beam geometry. The interval  $[\beta_0 - \pi, \beta_0 + \pi]$  defines the view angle range over which the projection data are used to reconstruct an image intersecting the helical source trajectory at view angle  $\beta_0$ . It is important to note that the filtering in (3) is naturally tangential [6, 20] due to the row-wise fan-to-parallel rebinning.

The 3D weighting function can be expressed in the form

$$w_{3d}(\alpha, \beta, t) = \frac{w_{2d}(\beta, t)g(\alpha_c, p(h))}{w_{2d}(\beta, t)g(\alpha_c, p(h)) + w_{2d}(\beta_c, t_c)g(\alpha, p(h))}, \quad (4)$$

where  $\alpha$  and  $\alpha_c$  are the cone angles corresponding to a direct ray and its conjugate ray, respectively [6], and  $h$  is the normalized helical pitch defined by

$$h = \frac{H}{L}, \quad (5)$$

where  $L$  represents the height of the detector along  $z$ -direction at the iso-center.

$g(|\alpha|, p(h))$  is a monotonically increasing function over the magnitude of cone angle  $\alpha$ , that is, given a normalized helical pitch  $h$ , one has

$$g(|\alpha_1|, p(h)) < g(|\alpha_2|, p(h)), \quad \text{while } |\alpha_1| < |\alpha_2|, \quad (6)$$

where  $p(h)$  is a monotonic increasing function of helical pitch  $h$ , that is,

$$p(h_1) < p(h_2), \quad \text{while } h_1 < h_2, \quad (7)$$

and the 3D weighting function  $w_{3d}(\alpha, \beta, \gamma)$  has to satisfy the normalization condition

$$w_{3d}(\alpha, \beta, t) + w_{3d}(\alpha_c, \beta_c, t_c) = 1.0. \quad (8)$$

Any 3D weighting function  $w_{3d}(\alpha, \beta, \gamma)$  satisfying the conditions specified by (6)–(8) is acceptable, and a special example is given by [6]

$$w_{3d}(\alpha, \beta, \gamma) = \frac{w_{2d}(\beta, t) \tan^{kh}(\alpha_c)}{w_{2d}(\beta, t) \tan^{kh}(\alpha_c) + w_{2d}(\beta_c, t_c) \tan^{kh}(\alpha)}, \quad (9)$$

where  $k$  is a parameter that varies over different helical pitches, and can be adjusted to get a balanced capability between artifact suppression and noise characteristics.  $w_{2d}(\beta, t)$  is a 2D view weighting function and can find its examples in the literature [12, 13, 21–24].

### 2.3. Projection of reconstruction plane and 3D weighting

Prior to extending the original 3D weighted helical CB-FBP algorithm presented above, it is insightful for us to investigate the projection of reconstruction plane in helical

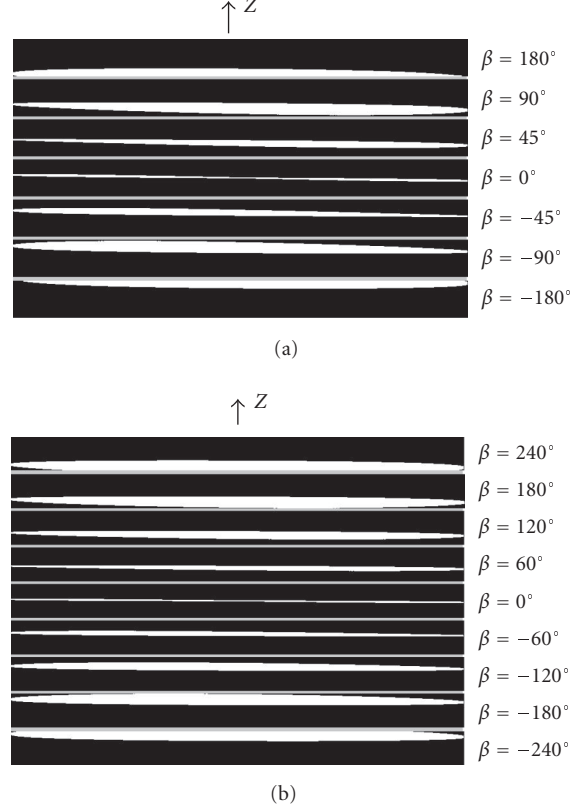


FIGURE 2: The schematic diagram showing the projection of image plane as a function over view angle at (a) helical pitch 33/64 : 1; and (b) helical pitch 63/64 : 1. (The vertical direction is parallel to the rotation axis of a CT gantry, while the horizontal direction corresponds to the latitudinal direction of the gantry.)

scanning in the cone-parallel geometry. Supposing the reconstruction plane is orthogonal to the  $z$ -axis and intersects the helical source trajectory at  $\beta = 0^\circ$ , shown in Figure 2(a) are the projections of reconstruction plane at helical pitch 63/64 : 1 corresponding to view angle  $\beta = -180^\circ, -90^\circ, -45^\circ, 0^\circ, 45^\circ, 90^\circ, 180^\circ$ , respectively, in which the white area corresponds to the projection of the reconstruction plane, and the grey area the outside of the detector. At such a helical pitch, about half projection of the reconstruction plane at  $\beta = \pm 180^\circ$  is outside the detector boundary (detector  $z$ -dimension:  $64 \times 0.625$  mm), and this is the reason why 3D weighting is needed in the original 3D weighted helical CB-FBP algorithm to reconstruct images in a full scan [6]. However, at a lower helical pitch, such as 33/64 : 1 as shown in Figure 2(b), projections of the reconstruction plane at  $\beta = \pm 180^\circ$  are within the detector boundaries. Notice that, even at  $\beta = \pm 240^\circ$ , a larger portion of the projection of reconstruction plane at pitch 33/64 : 1 is within the detector boundaries than that at helical pitch 63/64 : 1. Hence, it is intuitive to deduce that projection data corresponding to an overscan can be utilized at helical pitch 33/64 to reconstruct images with better noise characteristics or dose efficiency if the original 3D weighted helical CB-FBP algorithm can be extended to deal with overscan.

## 2.4. Extended 3D weighted helical CB-FBP algorithm

Suppose the angular range of projection data corresponding to an overscan is

$$[\beta_{\min}, \beta_{\text{axn}}] = [0, 2\pi + \Delta\beta]. \quad (10)$$

A direct extension of the original algorithm by just stretching the angular range from  $[0, 2\pi]$  to  $[0, 2\pi + \Delta\beta]$  violates the normalization condition specified in (8) and can result in artifacts in reconstructed images. However, if the helical trajectory angular range of an overscan  $[0, 2\pi + \Delta\beta]$  is decomposed into a union of  $N$  overlapped subangular ranges

$$[\beta_{\min}, \beta_{\text{max}}] = \bigcup_{i=0}^{N-1} [\beta_{\min,i}, \beta_{\text{max},i}], \quad (11)$$

and each subangular range spans  $2\pi$ , that is,

$$[\beta_{\min,i}, \beta_{\text{max},i}] = [0, 2\pi], \quad (12)$$

the original 3D weighted helical CB-FBP algorithm can be extended to reconstruct images from projection data corresponding to an overscan in the way specified below:

$$\begin{aligned} f(x, y, z) &= \frac{1}{2N} \sum_{i=0}^{N-1} \int_{\beta_{\min,i}}^{\beta_{\text{max},i}} \frac{R}{\sqrt{R^2 + Z(x, y, z)^2}} w_{3d,i}(\alpha, \beta_i, t) \tilde{s}(\alpha, \beta_i, t) d\beta_i, \end{aligned} \quad (13)$$

where the support of each 3D weighting function  $w_{3d,i}(\alpha, \beta_i, t)$  is  $[\beta_{\min,i}, \beta_{\text{max},i}]$ , that is, view angle  $\beta_i$  has to be determined within each subangular range, respectively.

Since a filtered backprojection reconstruction algorithm is linear from the perspective of system analysis, (13) can be rearranged as

$$f(x, y, z) = \frac{1}{2} \int_{\beta_{\min}}^{\beta_{\text{max}}} \frac{R}{\sqrt{R^2 + Z(x, y, z)^2}} w_{3d}(\alpha, \beta, t) \tilde{s}(\alpha, \beta, t) d\beta, \quad (14)$$

with

$$w_{3d}(\alpha, \beta, t) = \frac{1}{N} \sum_{i=0}^{N-1} w_{3d,i}(\alpha, \beta_i, t), \quad (15)$$

$$w_{3d,i}(\alpha, \beta, t) = \frac{w_{2d}(\beta_i, t) \tan^{kh}(\alpha_c)}{w_{2d}(\beta_i, t) \tan^{kh}(\alpha_c) + w_{2d}(\beta_{i,c}, t_c) \tan^{kh}(\alpha)}. \quad (16)$$

This means that the reconstructed image under a helical overscan is just a linear summation of the images reconstructed from data acquired over a series of full scans corresponding to each subangular range  $[\beta_{\min,i}, \beta_{\text{max},i}]$  ( $\beta_{\text{max},i} - \beta_{\min,i} = 2\pi$ ). The reconstruction accuracy corresponding to a full scan  $[\beta_{\min,i}, \beta_{\text{max},i}]$  ( $\beta_{\text{max},i} - \beta_{\min,i} = 2\pi$ ) has been evaluated and verified in [6]. Consequently, the reconstruction accuracy of the extended 3D weighted helical CB-FBP algorithm specified by (13) or (14) is warranted as long as

the overscan angular range  $[\beta_{\min,o}, \beta_{\text{max},o}]$  ( $\beta_{\text{max},o} - \beta_{\min,o} = 2\pi + \Delta\beta$ ) is decomposed into subangular ranges appropriately. Note that  $N$  is a parameter that can be optimized under various low helical pitches to achieve a balance between the most achievable image quality and computational efficiency, and  $w_{2d}(\beta_i, t)$  can be in the form [12]

$$w_{2d}(\beta_i, t) = \begin{cases} 0.0, & \beta \leq -\pi, \\ 0.25 \cdot \frac{(\beta + \pi)}{\beta_t}, & -\pi < \beta \leq -\pi + 2\beta_t, \\ 0.5, & -\pi + 2\beta_t < \beta \leq -2\beta_t, \\ 0.5 + \frac{0.25(\beta + 2\beta_t)}{\beta_t}, & -2\beta_t < \beta \leq 0, \\ 1.0 - \frac{0.25\beta}{\beta_t}, & 0 < \beta \leq 2\beta_t, \\ 0.5, & 2\beta_t < \beta \leq \pi - 2\beta_t, \\ 0.5 - 0.25 \cdot \frac{(\beta - \pi + 2\beta_t)}{\beta_t}, & \pi - 2\beta_t < \beta \leq \pi, \\ 0.0, & \beta > \pi, \end{cases} \quad (17)$$

where  $\beta_t$  is the parameter that can be adjusted to optimize the capability of suppressing artifacts and maintenance of noise characteristics or dose efficiency.

## 2.5. Evaluation

Just like the original algorithm, the extended 3D weighted helical CB-FBP algorithm is essentially approximate. Hence, the reconstruction accuracy of the extended algorithm has to be evaluated and verified experimentally. Two computer-simulated phantoms are utilized to evaluate the reconstruction accuracy. The first phantom is the helical body phantom (HBP) [14] to evaluate the reconstruction accuracy in transverse view, and the second is a modified Defrise phantom consisting of 5 cylindrical discs [15], rather than ellipsoidal discs in the original Defrise phantom, to evaluate the reconstruction accuracy in coronal view. The dimension of each disc is  $200 \times 200 \times 10 \text{ mm}^3$ , centered at the  $z$ -axis, and their linear attenuation coefficient is equivalent to a CT number of 600 HU in reconstructed tomographic images. The central disc is located at  $z = 0.0 \text{ mm}$ , and other 4 discs are 20 mm apart along the  $z$ -direction. In the computer simulation, the distance from source to the iso-center of the volumetric CT is 541.0 mm, the X-ray detector consists of 64 detector rows and each detector row is made up of 888 detector cells with a dimension of 0.625 mm along  $z$ -axis and 0.5836 mm in  $xy$ -plane at the iso-center, respectively. The scanning techniques for the computer phantom simulation are 120 kVp, 300 mA, and 1.0 sec/rot, respectively. To quantitatively investigate noise characteristics or dose efficiency, a 20 cm water phantom scanned by a volumetric CT scanner (LightSpeed VCT, GE Healthcare, Waukesha, WI, USA) is employed. The matrix dimension of a reconstructed transverse image is  $512 \times 512$ , no matter the projection data is

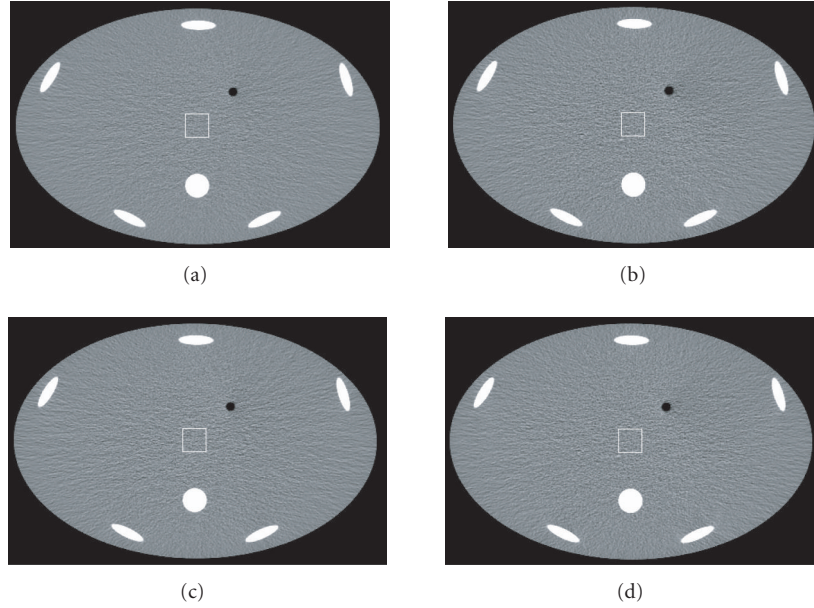


FIGURE 3: Tomographic images of the helical body phantom reconstructed by (a) the original algorithm using full-scan data at helical pitch  $33/64 : 1$ ; (b) the extended algorithm using overscan data at helical pitch  $33/64 : 1$ ; (c) the original algorithm using full-scan data at helical pitch  $63/64 : 1$ ; and (d) the extended algorithm using overscan data at helical pitch  $63/64 : 1$  ( $w/l = 200/0$  HU).

simulated or scanned by the volumetric CT system, and 984 projections are simulated or scanned in one turn of the helical scanning ( $360^\circ$ ).

### 3. RESULTS

In general, the extended 3D weighted helical CB-FBP algorithm is applicable at any helical pitch lower than  $1 : 1$ . Due to space limitation, only the results corresponding to helical pitch  $33/64 : 1$  and  $63/64 : 1$  are presented here. At helical pitch  $33/64 : 1$ , the parameters of the weighting function are selected as  $\beta_t = 0.15\pi$ ,  $\beta_{\max} - \beta_{\min} = 2.5\pi$ , and  $N = 3$ , while the parameters of the weighting function are selected as  $\beta_t = 0.225\pi$ ,  $\beta_{\max} - \beta_{\min} = 2.5\pi$  and  $N = 3$ , at helical pitch  $63/64 : 1$ .

#### 3.1. Evaluation of reconstruction accuracy

##### 3.1.1. Evaluation by the HBP phantom

At helical pitch  $33/64 : 1$ , the transverse image of the computer-simulated HBP phantom reconstructed by the original algorithm using full-scan projection data is presented in Figure 3(a), while the one at the same location but reconstructed by the extended algorithm using overscan projection data is in Figure 3(b). The reconstruction field of view (FOV) is 450 mm, and no helical artifact is observed in both images, showing that the reconstruction accuracy of the extended algorithm is as good as that of the original algorithm. More specifically, it has to be revealed that  $kh = 0.25$  for the original algorithm using full-scan projection data, while  $kh = 0.125$  for the extended algorithm using overscan projection data to reconstruct the image.

At helical pitch  $63/64 : 1$ , the transverse image of the HBP phantom reconstructed by the original algorithm using full-scan projection data is presented in Figure 3(c), while that at the same location but reconstructed by the extended algorithm using overscan projection data is in Figure 3(d). Again, no helical artifact is observed in both images, showing that the reconstruction accuracy of the extended algorithm is as good as that of the original algorithm at such a moderate helical pitch. Moreover, it has to be indicated that  $kh = 0.5$  for both the extended and original algorithms using full-scan and overscan projection data, respectively.

##### 3.1.2. Evaluation by the Defrise phantom

Multiple planar reformatted images in the coronal view of the Defrise phantom reconstructed by the original algorithm at helical pitch  $33/64 : 1$  using full-scan projection data is shown in Figure 4(a), while that by the extended algorithm using overscan projection data in Figure 4(b). Meanwhile, the coronal view of the Defrise phantom reconstructed by the original algorithm at helical pitch  $63/64 : 1$  using full-scan projection data is shown in Figure 4(c), while that by the extended algorithm using overscan projection data is in Figure 4(d). Just like the original reconstruction algorithm, the extended algorithm can reconstruct the Defrise phantom very well, showing that its reconstruction accuracy is comparable to the original 3D weighted helical CB-FBP algorithm.

#### 3.2. Evaluation of noise characteristics or dose efficiency

A total of 5 ROIs are chosen within the 250 mm FOV of the 20 cm cylindrical water phantom to gauge the noise

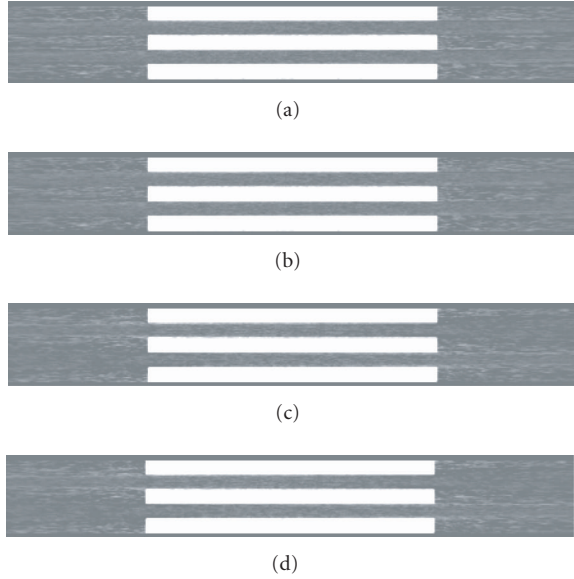


FIGURE 4: Multiple planar reformatted (coronal) images of the De-frise phantom reconstructed by (a) the original algorithm using full-scan data at helical pitch  $33/64 : 1$ ; (b) the extended algorithm using overscan data at helical pitch  $33/64 : 1$ ; (c) the original algorithm using full-scan data at helical pitch  $63/64 : 1$ ; and (d) the extended algorithm using overscan data at helical pitch  $63/64 : 1$  ( $w/l = 600/0$  HU).

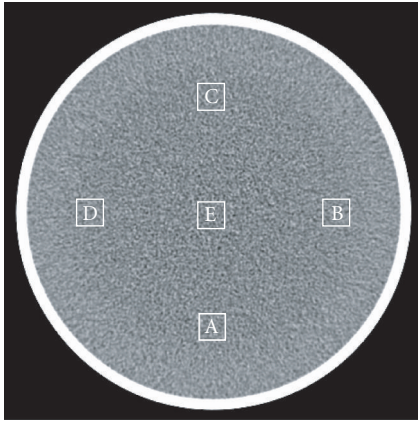


FIGURE 5: The schematic diagram showing the ROIs in the tomographic image of the 20 cm water phantom to gauge noise characteristics: ROI A, B, C, D, and E are square consisting of  $30 \times 30$  pixels; the center of ROI A, B, C, and D is 67.5 mm from the iso, while the center of ROI E is at the iso.

characteristics. As shown in Figure 5, the ROI labeled by E is at the iso-center, while those ROIs labeled by A, B, C, and D, respectively, are located at 6, 3, 12, and 9 o'clock orientation at 62.5 mm from the iso-center. Each ROI contains  $30 \times 30$  pixels, and the noise is measured as the standard deviation of Hounsfield Unit variation within the ROI.

At helical pitch  $33/64 : 1$ , the measured noise at those ROIs corresponding to the original algorithm are itemized

TABLE 1: Noise measurement of the ROIs specified in Figure 5 at helical pitches  $33/64 : 1$  and  $63/64 : 1$ , respectively.

ROI	Pitch = $33/64 : 1$		Pitch = $63/64 : 1$	
	Full scan ( $kh = 0.125$ )	Overscan ( $kh = 0.125$ )	Full scan ( $kh = 0.5$ )	Overscan ( $kh = 0.5$ )
A	7.98	7.42	8.40	8.23
B	7.89	7.31	8.49	8.27
C	7.51	7.28	8.09	7.95
D	7.14	6.74	7.61	7.49
E	8.89	8.58	9.49	9.34

in the 1st column of Table 1, and those corresponding to the extended algorithm are in the 2nd column. Apparently, the noise level at each ROI in the image reconstructed by the extended algorithm is significantly smaller than that in the image reconstructed by the original algorithm. Moreover, the noise uniformity at those ROIs in the image reconstructed by the extended algorithm is significantly better than that in the images reconstructed by the original algorithm. However, as shown in the right columns of Table 1, there is virtually no improvement in noise level and uniformity at helical pitch  $63/64 : 1$  in the images reconstructed by the extended algorithm over the original algorithm. This is consistent with our observation in Section 2.2, in which it has been shown that there is almost no extra projection data in comparison to a full scan can be utilized to reconstruct an image at helical pitch  $63/64 : 1$ .

#### 4. DISCUSSIONS AND CONCLUSIONS

It is well recognized that the 3D backprojection is the most computationally expensive process in image reconstruction using CB-FBP algorithms. It is important to point out that, the rearrangement of (13) into (14) not only simplifies algorithm expression but also improves image generation efficiency. In the implementation of (13), a total of  $N$  images corresponding to projection data acquired along each sub-angular range and weighted by  $w_{3d,i}(\alpha, \beta, t)$  have to be reconstructed using the original algorithm. However, in the implementation of (14), only one 3D backprojection is demanded to reconstruct image from projection data acquired along  $[\beta_{\min,i}, \beta_{\max,i}]$  ( $\beta_{\max,i} - \beta_{\min,i} = 2\pi$ ) and weighted by  $w_{3d}(\alpha, \beta, t)$ . Apparently, such an  $N : 1$  ratio in computational complexity assures that the implementation of the extended 3D weighted helical CB-FBP algorithm by (14) is a better choice than that by (13) in practice.

It is worthwhile indicating that (11) and (12) do not demand each subangular range  $[\beta_{\min,i}, \beta_{\max,i}]$  ( $\beta_{\max,i} - \beta_{\min,i} = 2\pi$ ) evenly shifting in the decomposition to cover the whole angular range  $[0, 2\pi + \Delta\beta]$ , while an even shifting can result in data manipulation efficiency. Moreover, it is not mandatory for the 3D weighting function  $w_{3d}(\alpha, \beta, t)$  corresponding to  $[\beta_{\min,o}, \beta_{\max,o}]$  ( $\beta_{\max,o} - \beta_{\min,o} = 2\pi + \Delta\beta$ ) to be the average of each 3D weighting function  $w_{3d-i}(\alpha, \beta_i, t)$  corresponding to  $[\beta_{\min,i}, \beta_{\max,i}]$  ( $\beta_{\max,i} - \beta_{\min,i} = 2\pi$ ) as specified by (15). Indeed, other weighted summation strategies can be exercised in practice.

As indicated in [6], the original 3D weighted helical CB-FBP algorithm can be implemented in the native CB geometry, although its derivation in the cone-parallel geometry was given as an example in [6]. Hence, the extended 3D weighted helical CB-FBP algorithm can also be implemented in the native CB geometry as its counterpart. Moreover, it has to be pointed out that the determination of the parameters  $\Delta\beta$  and  $kh$  is not optimized in the experimental evaluation shown above. All the parameters chosen are just to show how the extended 3D weighted helical CB-FBP algorithm works in overscan corresponding to helical pitches lower than 1 : 1.

It has to be emphasized that both the original 3D weighting scheme proposed in [6] and the extended 3D weighting scheme presented in this manuscript are ray-wise weightings. This means that, by making use of the cone angle corresponding to both direct and conjugate rays, the 3D weighting is actually a ray-wise optimization process to obtain balanced image quality and most achievable dose efficiency over helical pitches. By making use of the cone angle information corresponding to conjugate rays, our ray-wise 3D weighting scheme distinguishes itself from other 3D weighting schemes existing in the literature [7–9]. The readers that are interested in the difference between our ray-wise 3D weighting scheme and that proposed in [7] are referred to [6], where a brief discussion on the difference is given. Detector-row-dependent weighting schemes have been proposed in [8, 9], respectively. By using predefined weighting distribution, the ray intercepting inner detector rows are given favorable weights and those intercepting outer detector rows are given unfavorable weights, in which the cone angle information corresponding to conjugate ray is not utilized. The weight in our method is ray-wise calculated and such a ray-wise optimization process can make use of redundant projection data as much as possible over helical pitches, particularly at high helical pitches. However, it seems very hard, if not impossible, to make use of projection data as much as possible by using a predefined weighting distribution in the detector as done in [8, 9]. Interested readers are referred to references [8, 9] for more detail.

Moreover, it should be indicated that, the extended 3D weighted helical CB-FBP algorithm proposed in this manuscript is quite different from the n-PI CB reconstruction methods existing in the literature [25–27]. The concepts of Tam-window, PI-line, N-PI window, and N-PI line play critical roles in the derivation of both exact and approximate n-PI CB reconstruction algorithms. However, as clearly shown above, none of these concepts has been utilized in deriving the extended 3D weighted helical CB-FBP algorithm.

In summary, recognizing the clinical importance of reconstructing tomographic images from overscan projection data, the original 3D weighted helical CB-FBP algorithm has been extended in this manuscript to reconstruct tomographic images at helical pitches lower than 1 : 1. As shown in previous sections, such an extension can make use of projection data as efficient as possible, resulting in significantly improved noise characteristics or dose efficiency. In principle, the extended 3D weighted helical CB-FBP algorithm is approximate, but its reconstruction accuracy has been evaluated and verified at a relatively moderate cone

angle ( $4^\circ$ ) corresponding to a detector with the dimension of  $64 \times 0.625$  mm at the source to iso-center distance of 541.0 mm. In fact, the extended algorithm is expected to be applicable in volumetric CT scanners with the detector  $z$ -dimension corresponding to larger cone angles, and more investigation is being carried out to assure the maximum cone angle up to which the proposed algorithm can still provide acceptable reconstruction accuracy for diagnostic CT imaging applications.

## ACKNOWLEDGMENT

The authors would like to express their appreciation to the anonymous reviewers for their constructive comments and suggestions.

## REFERENCES

- [1] A. Katsevich, "Analysis of an exact inversion algorithm for spiral cone-beam CT," *Physics in Medicine and Biology*, vol. 47, no. 15, pp. 2583–2597, 2002.
- [2] A. Katsevich, "Theoretically exact filtered backprojection-type inversion algorithm for spiral CT," *SIAM Journal on Applied Mathematics*, vol. 62, no. 6, pp. 2012–2026, 2002.
- [3] Y. Zou and X. Pan, "Exact image reconstruction on PI-lines from minimum data in helical cone-beam CT," *Physics in Medicine and Biology*, vol. 49, no. 6, pp. 941–959, 2004.
- [4] J. D. Pack and F. Noo, "Cone-beam reconstruction using 1D filtering along the projection of M-lines," *Inverse Problems*, vol. 21, no. 3, pp. 1105–1120, 2005.
- [5] G.-H. Chen, "An alternative derivation of Katsevich's cone-beam reconstruction formula," *Medical Physics*, vol. 30, no. 12, pp. 3217–3226, 2003.
- [6] X. Tang, J. Hsieh, R. A. Nilsen, S. Dutta, D. Samsonov, and A. Hagiwara, "A three-dimensional-weighted cone beam filtered backprojection (CB-FBP) algorithm for image reconstruction in volumetric CT - Helical scanning," *Physics in Medicine and Biology*, vol. 51, no. 4, pp. 855–874, 2006.
- [7] K. Taguchi, B.-S. S. Chiang, and M. D. Silver, "A new weighting scheme for cone-beam helical CT to reduce the image noise," *Physics in Medicine and Biology*, vol. 49, no. 11, pp. 2351–2364, 2004.
- [8] K. Stierstorfer, A. Rauscher, J. Boese, H. Bruder, S. Schaller, and T. Flohr, "Weighted FBP—a simple approximated 3D FBP algorithm for multislice spiral CT with good dose usage for arbitrary pitch," *Physics in Medicine and Biology*, vol. 49, no. 11, pp. 2209–2218, 2004.
- [9] D. Heuscher, K. Brown, and F. Noo, "Redundant data and exact helical cone-beam reconstruction," *Physics in Medicine and Biology*, vol. 49, no. 11, pp. 2219–2238, 2004.
- [10] I. A. Feldkamp, L. C. Davis, and J. W. Kress, "Practical cone-beam algorithm," *Journal of the Optical Society of America A: Optics and Image Science, and Vision*, vol. 1, no. 6, pp. 612–619, 1984.
- [11] G. Wang, T.-H. Lin, P.-C. Cheng, and D. M. Shinozaki, "General cone-beam reconstruction algorithm," *IEEE Transactions on Medical Imaging*, vol. 12, no. 3, pp. 486–496, 1993.
- [12] C. R. Crawford and K. F. King, "Computed tomography scanning with simultaneous patient translation," *Medical Physics*, vol. 17, no. 6, pp. 967–982, 1990.
- [13] M. D. Silver, "A method for including redundant data in computed tomography," *Medical Physics*, vol. 27, no. 4, pp. 773–774, 2000.

- [14] X. Tang, "Matched view weighting in tilted-plane-based reconstruction algorithms to suppress helical artifacts and optimize noise characteristics," *Medical Physics*, vol. 30, no. 11, pp. 2912–2918, 2003.
- [15] X. Tang and J. Hsieh, "A filtered backprojection algorithm for cone beam reconstruction using rotational filtering under helical source trajectory," *Medical Physics*, vol. 31, no. 11, pp. 2949–2960, 2004.
- [16] M. Defrise and R. Clack, "Cone-beam reconstruction algorithm using shift-variant filtering and cone-beam backprojection," *IEEE Transactions on Medical Imaging*, vol. 13, no. 1, pp. 186–195, 1994.
- [17] P. E. Danielsson, P.-E. P. Edholm, J. Eriksson, and M. Magnusson-Seger, "Towards exact 3D-reconstruction for helical cone-beam scanning of long objects: a new arrangement and a new completeness condition," in *International Meeting on Fully Three-Dimensional Image Reconstruction in Radiology and Nuclear Medicine*, pp. 141–144, Pittsburgh, Pa, USA, June 1997.
- [18] S. Schaller, T. Flohr, and P. Steffen, "New efficient Fourier-reconstruction method for approximate image reconstruction in spiral cone-beam CT at small cone angles," in *Medical Imaging 1997: Physics of Medical Imaging*, vol. 3032 of *Proceedings of SPIE*, pp. 213–224, Newport Beach, Calif, USA, February 1997.
- [19] H. Tuy, "3D image reconstruction for helical partial cone beam scanners using wedge beam transform," Patent, US 6,104,775, 2000.
- [20] X. Yan and R. M. Leahy, "Cone beam tomography with circular, elliptical and spiral orbits," *Physics in Medicine and Biology*, vol. 37, no. 3, pp. 493–506, 1992.
- [21] D. L. Parker, "Optimal short scan convolution reconstruction for fanbeam CT," *Medical Physics*, vol. 9, no. 2, pp. 254–257, 1982.
- [22] J. Hsieh, "A general approach to the reconstruction of x-ray helical computed tomography," *Medical Physics*, vol. 23, no. 2, pp. 221–229, 1996.
- [23] K. Taguchi and H. Aradate, "Algorithm for image reconstruction in multi-slice helical CT," *Medical Physics*, vol. 25, no. 4, pp. 550–561, 1998.
- [24] H. Hu, "Multi-slice helical CT: scan and reconstruction," *Medical Physics*, vol. 26, no. 1, pp. 5–18, 1999.
- [25] R. Proska, Th. Koehler, M. Grass, and J. Timmer, "The n-PI-method for helical cone-beam CT," *IEEE Transactions on Medical Imaging*, vol. 19, no. 9, pp. 848–863, 2000.
- [26] A. Katsevich, "On two versions of a  $3\pi$  algorithm for spiral CT," *Physics in Medicine and Biology*, vol. 49, no. 11, pp. 2129–2143, 2004.
- [27] H. Yu, Y. Ye, S. Zhao, and G. Wang, "A backprojection-filtration algorithm for nonstandard spiral cone-beam CT with an n-PI-window," *Physics in Medicine and Biology*, vol. 50, no. 9, pp. 2099–2111, 2005.

**Xiangyang Tang** is currently with the Applied Science Laboratory of GE Healthcare Technologies as a Senior Scientist. With a focus on the development of image reconstruction algorithms for cone beam (CB) volumetric computed tomography (VCT) in diagnostic imaging, he has been working in the field of CB-VCT for almost 10 years, covering system analysis and design, development of algorithms for system



calibration, artifacts suppression, digital image/video processing, and CT cardiac imaging applications. In the recent 5 years, as an active Researcher in the field of medical imaging, he published more than 50 papers or book chapters in scientific journals and conference proceedings, and filed more than 10 US patent applications. Meanwhile, he also served as Guest Editor or Reviewer for a number of prestigious scientific journals in the field of medical imaging.

**Jiang Hsieh** is a Chief Scientist in the Applied Science Laboratory of GE Healthcare Technologies and an adjunct Professor in the Medical Physics Department of the University of Wisconsin, Madison. He has more than 20 years of experience in medical imaging. He holds over 100 US patents, has coauthored more than 100 articles, book chapters, and textbook. He taught AAPM summer school, refresher courses at RSNA, short courses at IEEE Medical Imaging Conference, AAPM annual meeting, and SPIE Medical Imaging Conference. His research interests include tomographic reconstruction, CT image artifact reduction and correction, signal processing, image processing, and advanced CT applications.



**Roy A. Nilsen** is currently a Principal Engineer of the Functional Imaging and Computed Tomography Image Reconstruction Group of GE Healthcare Technologies. He has been developing SW and HW for General Electric medical imaging devices since June 1988. Most of that time has been spent developing image reconstruction modules for CT systems. He has a B.S. degree in both electrical engineering and computer science from the University of Wisconsin.



**Scott M. McOlash** is a software Engineer in the Functional Imaging and Computed Tomography Image Reconstruction Group of GE Healthcare Technologies, where he currently develops and integrates reconstruction algorithms. His career includes 20 years of hardware and software development in applied research, CAD/CAM integration, industrial control networking, and diagnostic imaging. He holds an M.S. degree and a B.S. degree in electrical engineering from Marquette University in Milwaukee, WI.



# Comparison of Lesion Detection and Quantification in MAP Reconstruction with Gaussian and Non-Gaussian Priors

Jinyi Qi

*Department of Biomedical Engineering, University of California, Davis, CA 95616, USA*

Received 21 December 2005; Revised 13 April 2006; Accepted 19 April 2006

Statistical image reconstruction methods based on maximum a posteriori (MAP) principle have been developed for emission tomography. The prior distribution of the unknown image plays an important role in MAP reconstruction. The most commonly used prior are Gaussian priors, whose logarithm has a quadratic form. Gaussian priors are relatively easy to analyze. It has been shown that the effect of a Gaussian prior can be approximated by linear filtering a maximum likelihood (ML) reconstruction. As a result, sharp edges in reconstructed images are not preserved. To preserve sharp transitions, non-Gaussian priors have been proposed. However, their effect on clinical tasks is less obvious. In this paper, we compare MAP reconstruction with Gaussian and non-Gaussian priors for lesion detection and region of interest quantification using computer simulation. We evaluate three representative priors: Gaussian prior, Huber prior, and Geman-McClure prior. We simulate imaging a prostate tumor using positron emission tomography (PET). The detectability of a known tumor in either a fixed background or a random background is measured using a channelized Hotelling observer. The bias-variance tradeoff curves are calculated for quantification of the total tumor activity. The results show that for the detection and quantification tasks, the Gaussian prior is as effective as non-Gaussian priors.

Copyright © 2006 Jinyi Qi. This is an open access article distributed under the Creative Commons Attribution License, which permits unrestricted use, distribution, and reproduction in any medium, provided the original work is properly cited.

## 1. INTRODUCTION

Statistical image reconstruction methods have been developed for emission tomography to improve the signal-to-noise ratio (SNR), for example, [1–3]. The most popular maximum-likelihood (ML) reconstruction algorithm is the expectation-maximization (EM) algorithm [1, 4]. However, the ML estimate can be very noisy because emission tomography is an ill-posed problem. Hence some form of regularization is needed to obtain a useful image. Bayesian methods regularize the solution by using a prior probability distribution on the image. The prior probability distribution plays an important role in Bayesian image reconstruction. The most commonly used prior is the Gaussian prior which strongly discourages sharp transitions in images. To preserve edges, non-Gaussian priors have been proposed [3, 5, 6]. Empirical results showed that images reconstructed with edge-preserving non-Gaussian priors have less mean-squared error than those reconstructed with the Gaussian prior. However, the effect of edge-preserving priors on clinical tasks is not obvious.

Gifford et al. [7] compared a quadratic penalty function with Huber penalty functions in a penalized-EM algo-

rithm for tumor detection. However, the comparison was done as a function of iteration, so the result is algorithm-dependent. Nuyts and Michel [8] compared maximum a posteriori (MAP) reconstruction with a relative difference prior to post-smoothed ML reconstruction for hot lesion detection and found similar performance between MAP and post-smoothed ML reconstructions. In this paper we evaluate the performance of Bayesian image reconstructions with the Gaussian and non-Gaussian priors for hot lesion detection and region of interest quantification, which are two major clinical applications of emission tomography. Some preliminary results were reported in [9].

This paper is organized as follows. We briefly review Bayesian image reconstruction and different prior functions in Section 2. The methods for evaluating image quality are described in Section 3. The results are presented in Section 4. Finally, the conclusion is drawn in Section 5.

## 2. BAYESIAN IMAGE RECONSTRUCTION

In emission tomography data are well modeled as a collection of independent Poisson random variables with the mean  $\bar{y} \in \mathbb{R}^{M \times 1}$  related to the unknown image,  $\mathbf{x} \in \mathbb{R}^{N \times 1}$ , through an

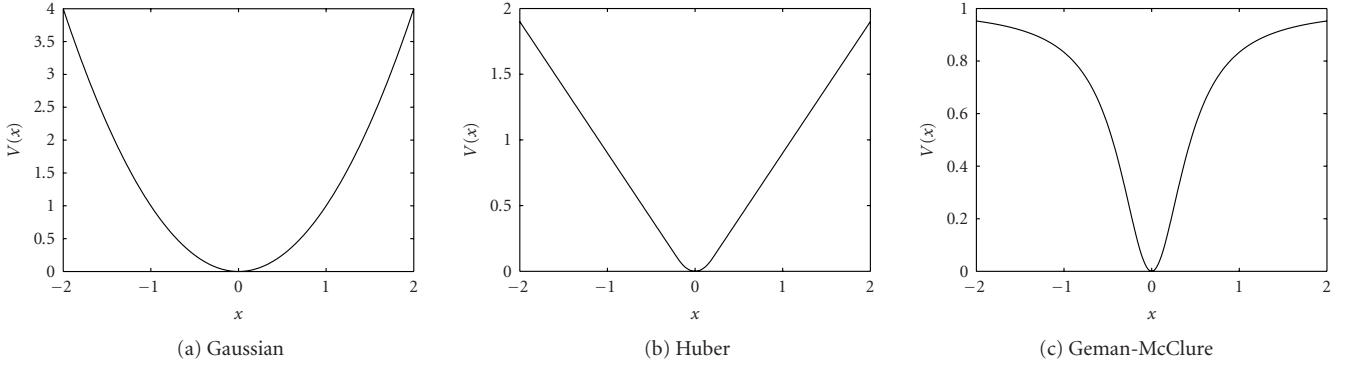


FIGURE 1: The potential functions of the Gaussian, Huber, and Geman-McClure priors.

affine transform

$$\bar{\mathbf{y}} = \mathbf{P}\mathbf{x} + \mathbf{r}, \quad (1)$$

where  $\mathbf{P} \in \mathbb{R}^{M \times N}$  is the detection probability matrix with element  $(i, j)$  equal to the probability of an event produced in voxel  $j$  being detected by sinogram bin  $i$ , and  $\mathbf{r} \in \mathbb{R}^{M \times 1}$  accounts for the presence of scatters and randoms in the data. The appropriate log-likelihood function is given by

$$L(\mathbf{y} | \mathbf{x}) = \sum_i (y_i \log \bar{y}_i - \bar{y}_i - \log y_i!), \quad (2)$$

where  $\mathbf{y}$  is the measured data.

The ML reconstruction can be obtained by maximizing (2). However, the ML estimate can be very noisy because emission tomography is an ill-posed problem. Bayesian methods regularize the noise by using a prior probability distribution on the image. Most image priors use a Markov random field with a Gibbs distribution of the form

$$p(\mathbf{x}) = \frac{1}{Z} e^{-\beta U(\mathbf{x})}, \quad (3)$$

where  $U(\mathbf{x})$  is the energy function,  $\beta$  is the hyperparameter that controls the resolution of the reconstructed image, and  $Z$  is a normalization constant. The Markovian properties of these distributions make them theoretically attractive as formalism for describing empirical local image properties, as well as computationally appealing. The energy function  $U(\mathbf{x})$  often contains potentials defined on pair-wise cliques of neighboring voxels:

$$U(\mathbf{x}) = \sum_{j=1}^N \sum_{k \in \mathcal{N}_j} \kappa_{jk} V(x_j - x_k), \quad (4)$$

where  $\mathcal{N}_j$  denotes the set of neighboring voxels of voxel  $j$ ,  $\kappa_{jk}$  are weighting factors, and  $V(\cdot)$  is the potential function. A wide range of potential functions has been studied in the literature that attempt to produce local smoothing while not removing or blurring true boundaries or edges in the image. All have the basic property that they are monotonic

nondecreasing functions of the absolute intensity difference  $|x_j - x_k|$ .

The potential function of a Gaussian prior is a quadratic function

$$V(x) = x^2. \quad (5)$$

It produces smooth images with very low probability of sharp transitions in intensity. In an attempt to increase the probability of sharp transitions, Bouman and Sauer [3] propose using the generalized  $p$ -Gaussian model where  $V(x) = |x|^p$ ,  $1 < p < 2$ . An alternative function is the Huber prior in which  $V(\cdot)$  is defined as [10]

$$V(x) = \begin{cases} \frac{x^2}{2\delta}, & |x| < \delta, \\ |x| - \frac{\delta}{2}, & |x| \geq \delta. \end{cases} \quad (6)$$

When  $\delta$  is small, the Huber function approximates the absolute value function. It is probably the most edge-preserving prior with a convex potential function. Other potential functions with similar behavior are  $V(x) = \log \cosh(\delta x)$  [6] and  $V(x) = \delta^2 [|\delta x| - \log(1 + |\delta x|)]$  [11]. In an attempt to produce even sharper intensity transitions, nonconvex functions have also been proposed. One example that we will study is the Geman-McClure prior [5], of which

$$V(x) = \frac{x^2}{x^2 + \delta^2}. \quad (7)$$

Figure 1 shows the potential functions of the Gaussian, Huber, and Geman-McClure priors. Note that in practice both the Huber prior and Geman-McClure prior can approach performance of the Gaussian prior by setting  $\delta$  to be sufficiently large.

To demonstrate the difference between these potential functions, we show two images in Figure 2. For the Huber prior ( $\delta \ll 1$ ) the two images are equally probable, while the Gaussian prior strongly favors the cone image (with an energy ratio of 50 : 1) and the Geman-McClure prior favors the disk image.

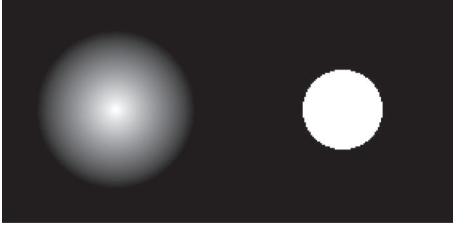


FIGURE 2: Images of a cone and a disk. The intensity in both images are between 0 and 1. See text for details.

Combine the likelihood function and prior distribution, the MAP reconstruction  $\hat{\mathbf{x}}$  is found by maximizing the log-posterior density function:

$$\hat{\mathbf{x}} = \arg \max_{\mathbf{x} \geq 0} [L(\mathbf{y} | \mathbf{x}) - \beta U(\mathbf{x})]. \quad (8)$$

For priors with a convex potential function, (8) generally has a unique solution. When nonconvex potential functions are used, there may exist multiple local optima and the solution of most deterministic optimization algorithms will depend on the initial image.

### 3. METHODS

#### 3.1. Computer simulation

We conduct computer simulations to study the effect of non-Gaussian priors on lesion detection. We simulate imaging of a prostate tumor using C-11 choline [12]. The simulated PET system has similar parameters as an ECAT HR+ clinical scanner (CPS, Knoxville, TN). It has 576 detectors forming a ring with radius 41.3 cm. The phantom has a body shape that is obtained from a patient image. The background has nearly uniform uptake of the radiotracer and has an attenuation coefficient of  $0.0095 \text{ mm}^{-1}$ . We place a round hot spot of different diameters (5 mm and 15 mm) at the center of the image to simulate a prostate tumor. Different pixel sizes are used in data generation and image reconstruction to introduce some model mismatch. For data generation, phantoms are represented by  $256 \times 256$  2-mm square pixels, whereas  $128 \times 128$  4.5-mm square pixels are used in reconstruction.

Figure 3 shows various phantom images that we used. Figure 3(a) is a fixed uniform background. Figures 3(b)–3(d) are three random backgrounds obtained by superimposing the background image in Figure 3(a) with a realization of lumpy backgrounds [13]. The lumpy backgrounds are modeled as

$$\text{LB} = \sum_{i=1}^K G(b, \sigma^2, \mathbf{r}_k), \quad (9)$$

where  $G(b, \sigma^2, \mathbf{r}_k)$  is a Gaussian blob with variance  $\sigma^2$  and height  $b$  centering at a random location  $\mathbf{r}_k$ , and  $K$  is a Poisson random variable. The mean of  $K$  is set to 100. Two sets of  $b$  and  $\sigma$  are used:  $b = 0.02$  and  $\sigma = 32 \text{ mm}$  in Figure 3(b);  $b = 0.1$  and  $\sigma = 23 \text{ mm}$  in Figures 3(c) and 3(d). In Figure 3(d)

we also add a hot region with activity to background ratio of 4 : 1 to mimic possible bladder uptake. In all four cases the mean activity of the background is about 0.20.

For each type of the background we generate three groups of data: background only, background with the 5-mm lesion, and background with the 15-mm lesion. Each group consists of 1000 independent identically distributed data sets. The expected total number of detected events is about 200 000. All data sets are independently reconstructed using a preconditioned conjugate gradient algorithm with the Gaussian prior, Huber prior, and Geman-McClure prior and different  $\beta$  and  $\delta$  values. Five hundred iterations are used to ensure effective convergence of the algorithm. All reconstructions start from a uniform image. For Geman-McClure prior, the reconstructed image may correspond to a local optimum of the log-posterior density function because the objective function is nonconvex.

#### 3.2. Lesion detection

Detection of cancerous lesions is one major task of emission tomography. A standard methodology for studying lesion detectability is the receiver operating characteristic (ROC) study that compares true positive versus false positive rates for human observers for the task of lesion detection. Numerical observers based on signal-detection theory have been developed to mimic human performance [14]. For a given reconstructed image  $\hat{\mathbf{x}}$ , a linear numerical observer computes a test statistic (a scalar-valued decision variable),  $\eta(\hat{\mathbf{x}})$ , by

$$\eta(\hat{\mathbf{x}}) = \mathbf{t}'\hat{\mathbf{x}}, \quad (10)$$

where  $\mathbf{t}$  is the observer template. The detection performance can be measured by the SNR of  $\eta(\hat{\mathbf{x}})$ , which is defined as

$$\begin{aligned} \text{SNR}^2 [\eta(\hat{\mathbf{x}})] &= \frac{(E[\eta(\hat{\mathbf{x}}) | H_1] - E[\eta(\hat{\mathbf{x}}) | H_0])^2}{(\text{var}[\eta(\hat{\mathbf{x}}) | H_1] + \text{var}[\eta(\hat{\mathbf{x}}) | H_0])/2} \\ &= \frac{2(\mathbf{t}'\mathbf{z})^2}{\mathbf{t}'\Sigma_{\hat{\mathbf{x}}|H_1}\mathbf{t} + \mathbf{t}'\Sigma_{\hat{\mathbf{x}}|H_0}\mathbf{t}}, \end{aligned} \quad (11)$$

where  $H_0$  is the null hypothesis representing lesion absent,  $H_1$  is the hypothesis representing lesion present,  $\Sigma_{\hat{\mathbf{x}}|H_1}$  and  $\Sigma_{\hat{\mathbf{x}}|H_0}$  are the conditional covariance matrices of  $\hat{\mathbf{x}}$  under hypotheses of  $H_1$  and  $H_0$ , respectively, and  $\mathbf{z} \equiv E[\hat{\mathbf{x}} | H_1] - E[\hat{\mathbf{x}} | H_0]$  is the difference between the mean reconstructions under the two hypotheses. When  $\eta(\hat{\mathbf{x}})$  is normally distributed, the area under the ROC curve (AUC) is related to the SNR by

$$\text{AUC} = \frac{1}{2} \left[ 1 + \text{erf} \left( \frac{\text{SNR}}{2} \right) \right], \quad (12)$$

where  $\text{erf}(x)$  is the error function.

We use a channelized Hotelling observer (CHO), which has been shown to correlate with human performance [15–19]. The test statistic of CHO is

$$\eta(\hat{\mathbf{x}}) = \mathbf{z}'\mathbf{U}'\mathbf{K}^{-1}(\mathbf{U}\hat{\mathbf{x}} + \mathbf{n}), \quad (13)$$

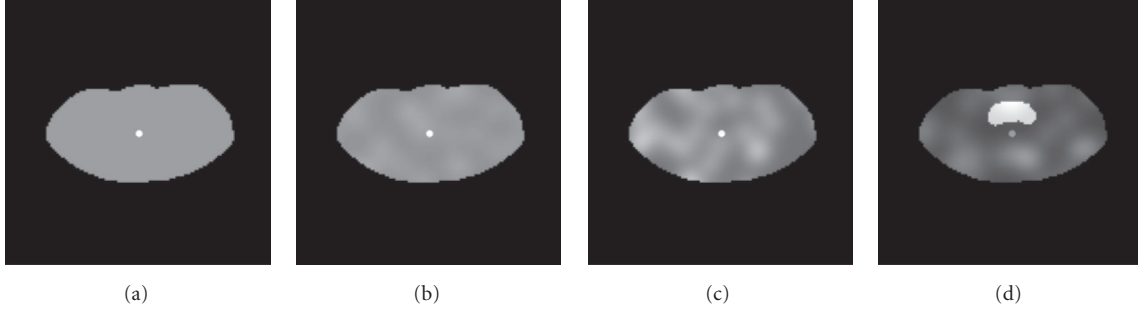


FIGURE 3: The simulated phantom with the 15-mm lesion in four different backgrounds. (a) The uniform background; (b) a lumpy background of  $b = 0.02$  and  $\sigma = 32$  mm; (c) a lumpy background of  $b = 0.1$  and  $\sigma = 23$  mm; and (d) a lumpy background of  $b = 0.1$  and  $\sigma = 23$  mm with a hot region mimicking bladder uptake. The mean of the background in all cases is about 0.20.

where  $\mathbf{U}$  denotes frequency-selective channels that mimic the human visual system,  $\mathbf{n}$  is the internal channel noise that models the uncertainty in the human detection process [20] with zero mean and covariance  $\mathbf{K}_N$ , and  $\mathbf{K}$  is the covariance of the channel outputs, that is,

$$\mathbf{K} = \frac{1}{2} \mathbf{U} (\Sigma_{\hat{\mathbf{x}}|H_1} + \Sigma_{\hat{\mathbf{x}}|H_0}) \mathbf{U}' + \mathbf{K}_N. \quad (14)$$

In this work the channel functions are the differences of four Gaussian functions with standard deviations  $\sigma = 2.653, 1.592, 0.995$ , and  $0.573$ , respectively [21]. The internal noise is modeled as uncorrelated noise with  $\mathbf{K}_N = \text{diag}[0.15\sigma_i^2 + 0.25 \max_i\{\sigma_i^2\}]$ , where  $\sigma_i^2$  is the data variance in the  $i$ th channel output [22]. Monte Carlo reconstructions are used to calculate the expectation of the reconstruction and covariance matrices. The SNR of CHO is then calculated by

$$\text{SNR}^2 [\eta(\hat{\mathbf{x}})] = \mathbf{z}' \mathbf{U}' \mathbf{K}^{-1} \mathbf{U} \mathbf{z} \quad (15)$$

because the SNR calculated from (15) is meaningful only when  $\eta(\hat{\mathbf{x}})$  is normally distributed, we also calculate AUCs from empirical ROC curves using numerical integration.

### 3.3. Quantification performance

Another clinical task in emission tomography is to quantify the uptake of radioactive tracer in a region of interest (ROI). This can be written as

$$\eta_Q(\hat{\mathbf{x}}) = \mathbf{t}' \hat{\mathbf{x}}, \quad (16)$$

where  $\mathbf{t}$  is the indicator function of the ROI, that is,  $t_j = 1$  if voxel  $j$  is inside the ROI, and  $t_j = 0$  otherwise. The accuracy of the quantification can be measured by the bias and variance of  $\eta_Q(\hat{\mathbf{x}})$  as

$$\begin{aligned} \text{bias}(\eta_Q) &= \mathbf{t}' \mathbf{x} - \mathbf{t}' E[\hat{\mathbf{x}}], \\ \text{var}(\eta_Q) &= \mathbf{t}' \Sigma_{\hat{\mathbf{x}}|H_1} \mathbf{t}, \end{aligned} \quad (17)$$

where  $\mathbf{x}$  denotes the true tracer uptake. Note that the ROI quantification is only performed on images in which a lesion is known to be present.

We use the bias versus variance tradeoff curve to evaluate the quantification performance. The above equations are calculated from Monte Carlo reconstructions.

## 4. RESULTS

Figures 4 and 5 show examples of reconstructed images with different priors. For all priors the reconstructed images become less noisy as we increase the hyperparameter  $\beta$ . The images reconstructed with the Gaussian prior have blurred edges, whereas the images reconstructed with the Huber prior and Geman-McClure prior tend to form piece-wise constant regions.

Figure 6 shows the variation of AUC as a function of  $\beta$  and  $\delta$  for detecting the 15-mm lesion in the lumpy background shown in Figure 3(c). In this case, the optimum parameters for the Gaussian, Huber, and Geman-McClure priors are  $\beta = 30$ ,  $(\beta = 10, \delta = 0.1)$ , and  $(\beta = 0.3, \delta = 0.1)$ , respectively. Comparing to the results of the fixed background (not shown), we found that lumpy backgrounds reduce lesion detectability at low resolution (large  $\beta$ ) and slightly decrease the optimum  $\beta$  value for lesion detection.

To give a fair comparison between different priors, we choose to compare the maximum SNR and maximum AUC of each prior. The results are shown in Figure 7. The error bars are computed using a bootstrap method. In all detection studies, the contrasts of the 5-mm and 15-mm lesions are 3 and 0.9, respectively, which are selected to obtain a reasonable detectability ( $\text{AUC} \approx 0.9$ ). In each case, SNR and AUC give similar ranking for the optimum performances of the three priors. No statistically significant advantage is found for non-Gaussian priors. For lesions with lower contrast, we expect the performances of the three priors to be even closer. We notice that some differences in AUC do not correspond well to the differences in SNR (see Figures 7(c) and 7(d)), which indicates that the test statistics of the numerical observer does not follow a Gaussian distribution.

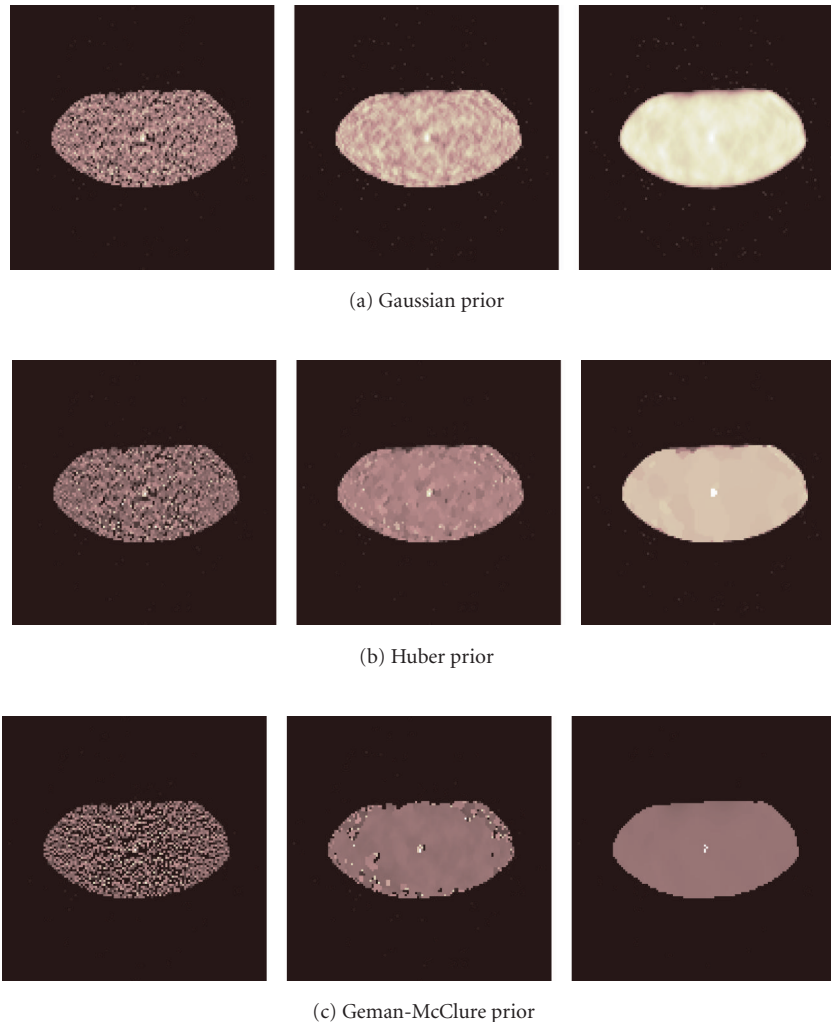


FIGURE 4: Reconstructed images of one noisy data set with a fixed background. The three images in each group are reconstructed with different  $\beta$ .

Figure 8 shows the bias versus variance tradeoff curves for quantification. The contrast of the lesion is 3.0 for the 5-mm lesion and 0.9 for the 15-mm lesion, respectively. The ROIs were obtained from the original phantom image. Bias and standard deviation are normalized to the total activity inside each ROI. Here we plot all the cases. It is interesting to see that Gaussian prior seems to set a lower bound for the Huber and Geman-McClure priors (except in Figure 8(h)). Considering that both Huber and Geman-McClure priors include Gaussian prior as a special case, no improvement in ROI quantification is found by using the Huber or Geman-McClure prior. In many cases, the performance of the non-Gaussian priors is much worse than that of the Gaussian prior, indicating that hyperparameter selection is more important for non-Gaussian priors. In Figures 8(b), 8(d), 8(f) there is a kink in the Gaussian bias-variance curve at low noise levels. This is because at such low resolution the reconstructed background is no longer uniform, but forms a dome, which artificially increases the ac-

tivity inside the ROI and, hence, reduces the bias. The decrease in bias at low noise levels in Figures 8(g) and 8(h) is mostly caused by the spill-over effect of the nearby hot region (“bladder”).

We also studied lesions with higher contrast (9 for the 5-mm lesion and 2.7 for the 15-mm lesion, respectively) and found very similar results [9]. To investigate the bias-variance tradeoff for large regions, we quantify the total activity in the hot “bladder” in Figure 3(d). The results are shown in Figure 9. Even for this large region with 4 : 1 activity ratio, we do not see any advantage of using the Huber and Geman-McClure priors.

## 5. CONCLUSION AND DISCUSSION

We have compared the performance of three representative priors for lesion detection and ROI quantification. The Gaussian prior is the most commonly used prior in emission reconstruction; the Huber prior is probably the most

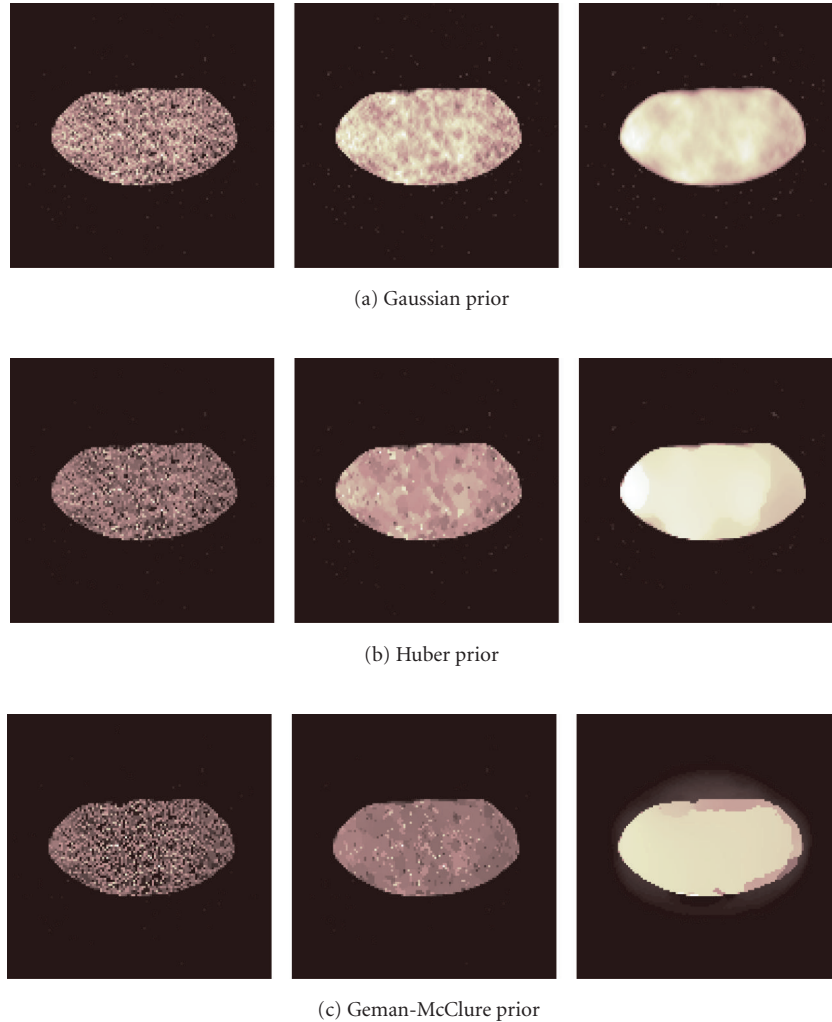


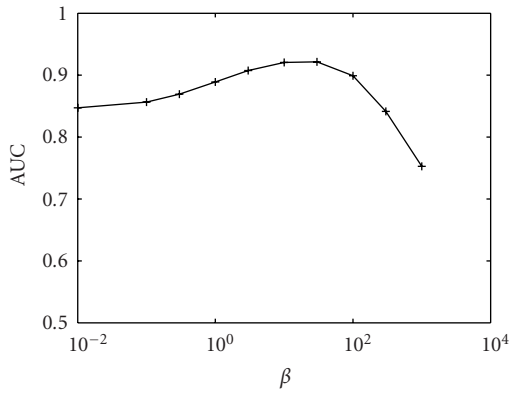
FIGURE 5: Reconstructed images of one noisy data set with the lumpy background shown in Figure 3(c). The three images in each group are reconstructed with different  $\beta$ .

edge-preserving prior among all priors with a convex potential function; and the Geman-McClure is a typical edge-preserving prior with a nonconvex potential function. Note that both the Huber and Geman-McClure priors can approach the Gaussian prior by setting  $\delta$  to be sufficiently large. Thus we focus on whether the Huber and Geman-McClure priors can outperform the Gaussian prior. In all the cases that we have tested, we have not observed any significant improvement. The results show that for the detection and quantification tasks that are considered here, the Gaussian prior is as effective as the more complex non-Gaussian priors.

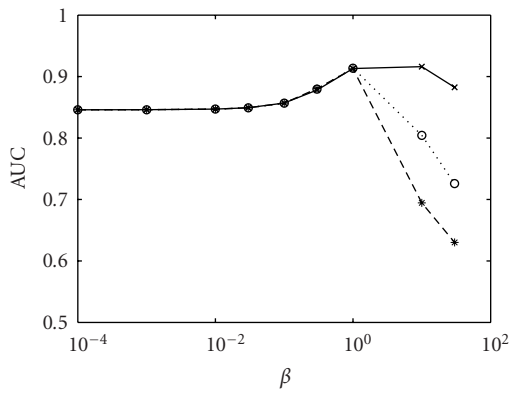
We should note that while we have investigated each prior with a range of  $\beta$  and  $\delta$  values, it is still possible that the results may not reflect the best performance for non-Gaussian priors because of the lack of theoretical guidance on the hyperparameter selection for non-Gaussian priors. Nonetheless, the results indicate that hyperparameter selection is extremely important for non-Gaussian priors. For the Geman-

McClure prior, the simulation results presented here may not correspond to the global maximum of the log posterior distribution because the objective function is nonconcave. It is possible that the performance of Geman-McClure prior may be improved by using deterministic or stochastic annealing techniques at an expense of increased computational cost [23].

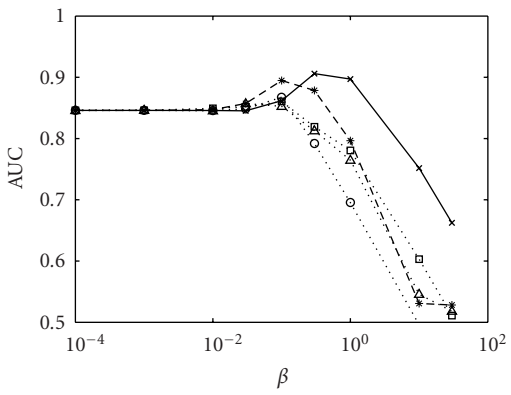
In this paper we used a channelized Hotelling observer for lesion detection and a simple ROI estimator for quantification because of their popularity. It is possible that some results might change if different observers or estimators were used. In ROI quantification we defined ROI using the original phantom data. If an ROI is to be delineated on the reconstructed image, the error in ROI delineation will also affect the ROI quantification [24]. Such effect is not included in this study. We expect that with the recent development of combined PET/CT and SPECT/CT scanners, high-resolution anatomical images will help to reduce the error in ROI definition.



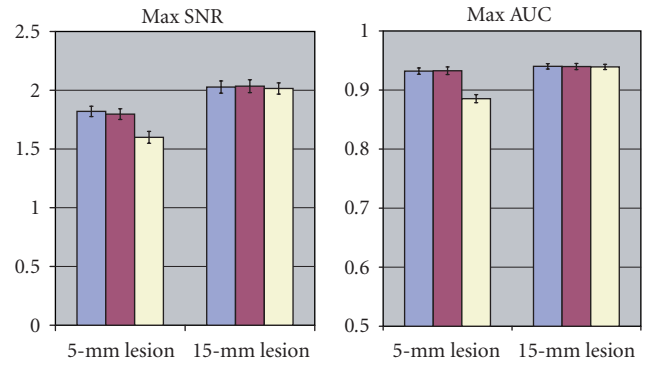
(a)



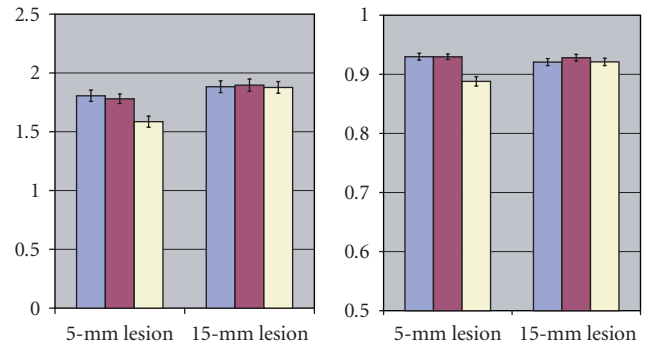
(b)



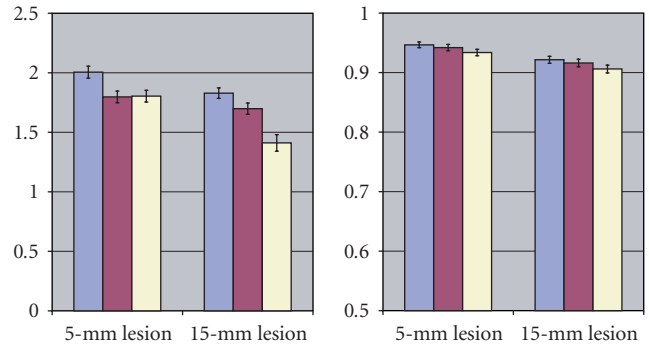
(c)



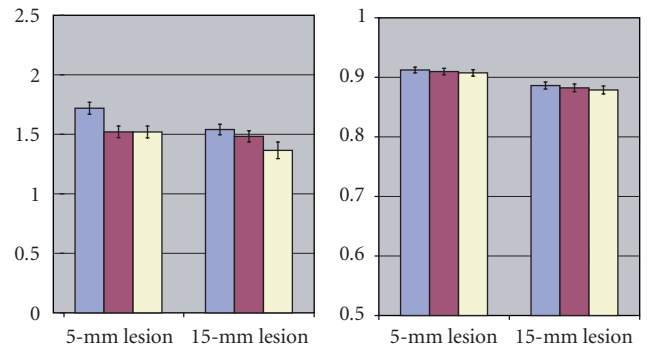
(a)



(b)



(c)



■ Gauss ■ Huber ■ Geman-McClure

(d)

FIGURE 6: Plots of AUCs for detecting the 15-mm lesion in the lumpy background shown in Figure 3(c) as a function of the prior parameters: (a) Gaussian prior; (b) Huber prior; and (c) Geman-McClure prior.

FIGURE 7: The maximum SNR and maximum AUC for detecting a lesion in different backgrounds. (a) Fixed background; (b) lumpy backgrounds in Figure 3(b); (c) lumpy backgrounds in Figure 3(c); and (d) lumpy backgrounds in Figure 3(d).

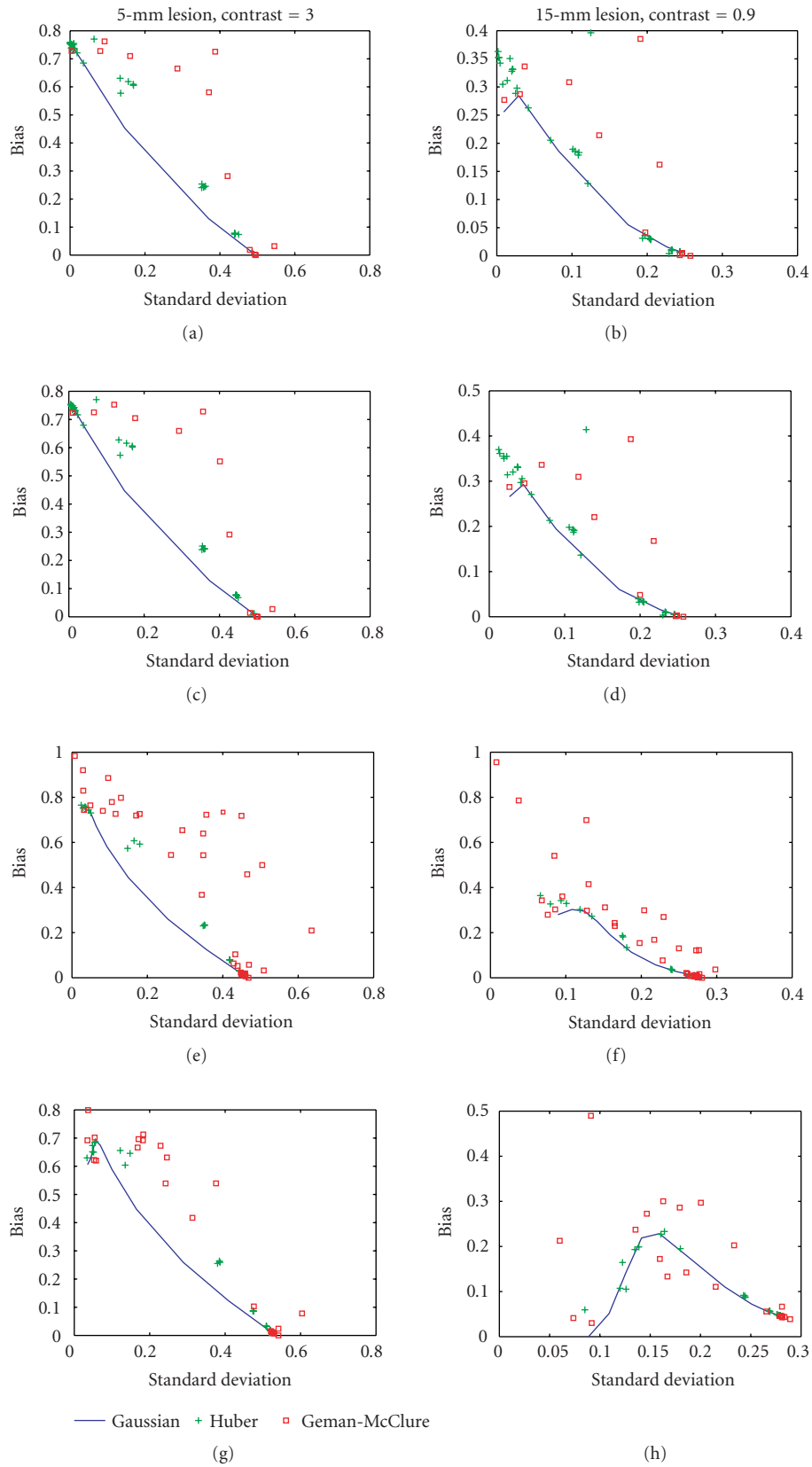


FIGURE 8: The bias versus standard deviation tradeoff for quantification of total uptake of a tumor in different backgrounds. (a) and (b) Fixed uniform background; (c) and (d) lumpy backgrounds in Figure 3(b); (e) and (f) lumpy backgrounds in Figure 3(c); and (g) and (h) lumpy backgrounds in Figure 3(d).

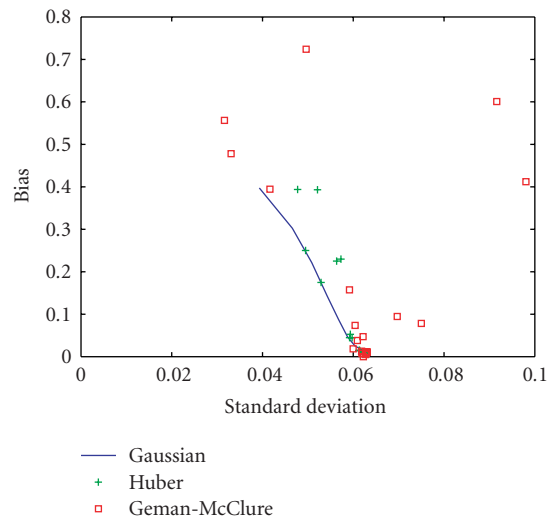


FIGURE 9: The bias versus standard deviation tradeoff for quantification of the large hot region ("bladder") in Figure 3(d).

## ACKNOWLEDGMENT

This work is supported by National Institutes of Health under Grant R01 EB000194.

## REFERENCES

- [1] L. Shepp and Y. Vardi, "Maximum likelihood reconstruction for emission tomography," *IEEE Transactions on Medical Imaging*, vol. 1, no. 2, pp. 113–122, 1982.
- [2] J. A. Fessler and A. O. Hero III, "Penalized maximum-likelihood image reconstruction using space-alternating generalized EM algorithms," *IEEE Transactions on Image Processing*, vol. 4, no. 10, pp. 1417–1429, 1995.
- [3] C. A. Bouman and K. Sauer, "A unified approach to statistical tomography using coordinate descent optimization," *IEEE Transactions on Image Processing*, vol. 5, no. 3, pp. 480–492, 1996.
- [4] K. Lange and R. Carson, "EM reconstruction algorithms for emission and transmission tomography," *Journal of Computer Assisted Tomography*, vol. 8, no. 2, pp. 306–316, 1984.
- [5] S. Geman and D. McClure, "Bayesian image analysis: an application to single photon emission tomography," in *Proceedings of the Statistical Computing Section of the American Statistical Association*, pp. 12–18, Washington, DC, USA, 1985.
- [6] P. J. Green, "Bayesian reconstructions from emission tomography data using a modified EM algorithm," *IEEE Transactions on Medical Imaging*, vol. 9, no. 1, pp. 84–93, 1990.
- [7] H. C. Gifford, T. H. Farncombe, and M. A. King, "Ga-67 tumor detection using penalized-EM with nonanatomical regularizers," in *Proceedings of the IEEE Nuclear Science Symposium and Medical Imaging Conference (NSS-MIC '02)*, vol. 3, pp. 1397–1401, Norfolk, Va, USA, November 2002.
- [8] J. Nuyts and C. Michel, "Performance of the relative difference prior for hot lesion detection in whole-body PET/CT: an evaluation with numerical and real observers," in *Proceedings of the IEEE Nuclear Science Symposium and Medical Imaging Conference (NSS-MIC '05)*, pp. 2155–2159, Wyndham El Conquistador, Puerto Rico, USA, October 2005.
- [9] J. Qi, "Investigation of lesion detection and quantitation in MAP reconstruction with non-Gaussian priors," in *Proceedings of the IEEE Nuclear Science Symposium and Medical Imaging Conference (NSS-MIC '05)*, pp. 1704–1708, Wyndham El Conquistador, Puerto Rico, USA, October 2005.
- [10] P. J. Huber, *Robust Statistics*, John Wiley & Sons, New York, NY, USA, 1981.
- [11] K. Lange, "Convergence of EM image reconstruction algorithms with Gibbs smoothing," *IEEE Transactions on Medical Imaging*, vol. 9, no. 4, pp. 439–446, 1990, correction: vol. 10, no. 2, p. 228, 1991.
- [12] T. Hara, N. Kosaka, and H. Kishi, "PET imaging of prostate cancer using carbon-11-choline," *Journal of Nuclear Medicine*, vol. 39, no. 6, pp. 990–995, 1998.
- [13] J. P. Rolland and H. H. Barrett, "Effect of random background inhomogeneity on observer detection performance," *Journal of the Optical Society of America A*, vol. 9, no. 5, pp. 649–658, 1992.
- [14] H. H. Barrett, J. Yao, J. Rolland, and K. Myers, "Model observers for assessment of image quality," *Proceedings of the National Academy of Sciences of the United States of America*, vol. 90, no. 21, pp. 9758–9765, 1993.
- [15] C. K. Abbey, H. H. Barrett, and D. W. Wilson, "Observer signal-to-noise ratios for the ML-EM algorithm," in *Medical Imaging 1996: Image Perception*, vol. 2712 of *Proceedings of SPIE*, pp. 47–58, Newport Beach, Calif, USA, February 1996.
- [16] D. de Vries, M. A. King, E. Soares, B. Tsui, and C. Metz, "Effects of scatter subtraction on detection and quantitation in hepatic SPECT," *Journal of Nuclear Medicine*, vol. 40, no. 6, pp. 1011–1023, 1999.
- [17] T. Narayan and G. Herman, "Prediction of human observer performance by numerical observers: an experimental study," *Journal of the Optical Society of America A*, vol. 16, no. 3, pp. 679–693, 1999.
- [18] S. D. Wollenweber, B. M. W. Tsui, D. S. Lalush, E. C. Frey, K. J. LaCroix, and G. T. Gullberg, "Comparison of Hotelling observer models and human observers in defect detection from myocardial SPECT imaging," *IEEE Transactions on Nuclear Science*, vol. 46, no. 6, pp. 2098–2103, 1999.
- [19] H. Gifford, M. A. King, D. de Vries, and E. Soares, "Channelized Hotelling and human observer correlation for lesion detection in hepatic SPECT imaging," *Journal of Nuclear Medicine*, vol. 41, no. 3, pp. 514–521, 2000.
- [20] J. Yao and H. H. Barrett, "Predicting human performance by a channelized Hotelling observer model," in *Mathematical Methods in Medical Imaging*, vol. 1768 of *Proceedings of SPIE*, pp. 161–168, San Diego, Calif, USA, July 1992.
- [21] M. A. King, D. de Vries, and E. Soares, "Comparison of the channelized Hotelling and human observers for lesion detection in hepatic SPECT imaging," in *Medical Imaging 1997: Image Perception*, vol. 3036 of *Proceedings of SPIE*, pp. 14–20, Newport Beach, Calif, USA, February 1997.
- [22] J. Oldan, S. Kulkarni, Y. Xing, P. Khurd, and G. Gindi, "Channelized hotelling and human observer study of optimal smoothing in SPECT MAP reconstruction," *IEEE Transactions on Nuclear Science*, vol. 51, no. 3, pp. 733–741, 2004.
- [23] S. Geman and D. Geman, "Stochastic relaxation, Gibbs distributions, and the Bayesian restoration of images," *IEEE Transactions on Pattern Analysis and Machine Intelligence*, vol. 6, no. 6, pp. 721–741, 1984.
- [24] R. G. Wells, H. C. Gifford, and M. A. King, "Impact of ROI definition on estimator performance on FBP reconstructed Ga-67 SPECT images," *IEEE Transactions on Nuclear Science*, vol. 47, no. 3, pp. 1210–1217, 2000.

**Jinyi Qi** received the B.Eng. degree (with highest honor) from Tsinghua University in Beijing in 1993, and the M.S. and Ph.D. degrees from the University of Southern California in 1997 and 1998, respectively, all in electrical engineering. He was recognized with the 2001 Young Investigator Medical Image Science Award by the IEEE Nuclear and Plasma Science Society for contributions to the analysis of Bayesian image



reconstruction algorithms, and for the development of high-resolution 3D Bayesian image reconstruction methods for animal PET scans. Currently he is an Assistant Professor in the Department of Biomedical Engineering at the University of California, Davis, and is also a Faculty Scientist in the Department of Functional Imaging at Lawrence Berkeley National Laboratory. His research interests include statistical image reconstruction, medical image processing, image quality evaluation, and imaging system optimization.

# Comparison of Quadratic- and Median-Based Roughness Penalties for Penalized-Likelihood Sinogram Restoration in Computed Tomography

Patrick J. La Rivière, Junguo Bian, and Phillip A. Vargas

*Department of Radiology, The University of Chicago, Chicago, IL 60637, USA*

Received 13 December 2005; Revised 3 March 2006; Accepted 5 March 2006

We have compared the performance of two different penalty choices for a penalized-likelihood sinogram-restoration strategy we have been developing. One is a quadratic penalty we have employed previously and the other is a new median-based penalty. We compared the approaches to a noniterative adaptive filter that loosely but not explicitly models data statistics. We found that the two approaches produced similar resolution-variance tradeoffs to each other and that they outperformed the adaptive filter in the low-dose regime, which suggests that the particular choice of penalty in our approach may be less important than the fact that we are explicitly modeling data statistics at all. Since the quadratic penalty allows for derivation of an algorithm that is guaranteed to monotonically increase the penalized-likelihood objective function, we find it to be preferable to the median-based penalty.

Copyright © 2006 Patrick J. La Rivière et al. This is an open access article distributed under the Creative Commons Attribution License, which permits unrestricted use, distribution, and reproduction in any medium, provided the original work is properly cited.

## 1. INTRODUCTION

We have recently developed penalized-likelihood approaches to the problems of sinogram smoothing and sinogram restoration in computed tomography [1–4], with a particular eye to the low-dose regime being considered for screening studies for lung and colon cancer [5–9]. In both cases, we assume that the statistics of each detector measurement are given by the sum of a compound Poisson term, representing the photon counting statistics for polychromatic photons, and a Gaussian term, representing electronic noise. In the case of sinogram restoration, we generalize the measurement model to include blurring coefficients representing sinogram degradations such as off-focal radiation, detector afterglow, and detector crosstalk [2, 4]. From the noisy, degraded measurements, we then seek to estimate a set of “ideal,” undegraded line integrals by iteratively maximizing an objective function comprising a sum of a simple Poisson likelihood (an approximation to the measurement statistics assumed above) and a roughness penalty. The estimated line integrals can then be fed into an existing analytic reconstruction algorithm, such as those typically implemented in hardware on commercial CT scanners. The hope is that this iterative sinogram-domain approach would provide some of the statistical advantages of fully iterative approaches to image reconstruction at a lower computational cost.

In our previous studies of the smoothing and restoration approaches, we have made use of a quadratic roughness penalty applied in the line integral (log) domain to the difference between a given sample in sinogram space and its four adjoining neighbors, that is, between a given detector channel and its two neighboring channels (we assumed a single-row detector), as well as to its own reading at the preceding and following view angles. While the approaches performed better in resolution-variance studies at low doses than did Hsieh’s noniterative adaptive trimmed mean (ATM) filter [10], the ATM filter was surprisingly effective at reducing the influence of a small number of very noisy measurements without unduly compromising resolution. The ATM filter is only applied to measurements whose signal strength falls below a certain threshold, and it entails replacing the value in question with the trimmed mean of the values in a neighborhood of the sinogram around the measurement in question. The trimmed mean filter is a median-like filter based on order statistics, and it varies adaptively between applying a true median filter and a simple boxcar filter, depending on the signal level. The relatively strong performance of this filter suggested that it would be worthwhile to explore the use of a median-based roughness penalty in the context of the sinogram smoothing and restoration methods we have developed.

The use of median-based roughness penalties in fully iterative penalized-likelihood image reconstruction was pioneered by Alenius et al., who referred to them as median root priors (MRPs) [11, 12]. Unfortunately, it does not appear to be possible to derive an iterative algorithm that is guaranteed to monotonically increase an objective function based on the MRP of Alenius et al. However, they derive a heuristic update equation, based on Green's one-step-late (OSL) strategy [13], that does not necessarily correspond to the maximization of a predefined objective function, but that does yield good results in practice.

In this work, we explore the use of a standard MRP penalty like those of Alenius et al. in the context of our sinogram-restoration approach and we make use of the heuristic, OSL strategy to derive the iterative update. We compare the images qualitatively and quantitatively to those obtained by use of our method with quadratic roughness penalties, as well as to those obtained by use of Hsieh's ATM filter.

## 2. METHODS

### 2.1. Measurement model

We assume that the CT scan produces a set of measurements that are represented as a one-dimensional (1D) vector  $\mathbf{y}^{\text{meas}}$ , with elements  $y_i^{\text{meas}}, i = 1, \dots, N_y$ , where  $N_y$  is the total number of measurements in the scan, and the index  $i$  denotes a particular attenuation line through the patient (i.e., a specific combination of detector channel, detector row, and projection angle).

To review the model, we have been employing [2–4], we assume, when we simulate data, that each  $y_i^{\text{meas}}$  is a realization of a random variable  $Y_i^{\text{meas}}$  whose statistics are described by

$$\begin{aligned} & \mathbf{y}_i^{\text{meas}} \\ &= G_i \sum_{m=1}^M E_m \text{Poisson} \left\{ \sum_{j=1}^{N_y} b_{ij} I_j \lambda_m^{(j)} \exp \left[ - \int_{L_j} \mu(\mathbf{x}, E_m) dl \right] + s_m^{(i)} \right\} \\ & \quad + \text{Normal} \{d_i, \sigma_i^2\}, \end{aligned} \quad (1)$$

with the various terms in this equation defined in Table 1. The compound Poisson distribution in the first term has been derived and validated by Whiting [14] and rederived by Elbakri and Fessler [15, 16]. We assume that  $I_i, G_i, d_i, \sigma_i^2$ , the average energy  $\bar{E}_i \equiv \sum_{m=1}^M E_m \lambda_m^{(i)}$  of the incident beam, and an energy-averaged and normalized estimated scatter term  $\bar{s}_i \equiv (1/\bar{E}_i) \sum_{m=1}^M E_m s_m^{(i)}$  are all known.

Our goal is to estimate a set of ideal, ‘‘monochromatic’’ attenuation line integrals:

$$l_i^{(\text{mono})} \equiv \int_{L_i} \mu(\mathbf{x}, E_r) dl, \quad (2)$$

$i = 1, \dots, N_y$ , at some reference energy  $E_r$  (usually  $\bar{E}_i$ ), from the set of measurements  $y_i^{\text{meas}}, i = 1, \dots, N_y$ . These estimated

line integrals can then be input to a standard analytic reconstruction algorithm as mentioned above.

Our strategy for estimating the line integrals entails maximizing a penalized-likelihood objective function. Because the model of (1) does not yield a tractable likelihood, we approximate it by defining a vector  $\mathbf{y}$  of new adjusted measurements with elements

$$y_i \equiv \left[ \left( \frac{y_i^{\text{meas}} - d_i}{\bar{E}_i G_i} \right) + \frac{\sigma_i^2}{G_i^2 \bar{E}_i^2} \right]_+, \quad (3)$$

where  $[x]_+$  is  $x$  for positive  $x$  and zero otherwise, that are realizations of random variables  $Y_i$  which we assume are approximately Poisson-distributed:

$$Y_i \sim \text{Poisson} \left\{ \sum_{j=1}^{N_y} I_j b_{ij} e^{-l_j^{(\text{poly})}} + \bar{s}_i + \frac{\sigma_i^2}{G_i^2 \bar{E}_i^2} \right\}, \quad (4)$$

where

$$l_j^{(\text{poly})} = f_j \left( l_j^{(\text{mono})} \right), \quad (5)$$

with  $f_j(l)$  being an empirically determined function, typically polynomial, that adequately captures the effect of beam hardening in slices that do not contain substantial amounts of bone [17]. Our strategy is then to estimate the vector  $\mathbf{l}^{(\text{poly})}$ , with elements  $l_j^{(\text{poly})}$ , from the vector of adjusted measurements  $\mathbf{y}$ , since the needed  $l_i^{(\text{mono})}$  can then be obtained by inverting (5). For simplicity, we drop the (poly) superscripts from  $\mathbf{l}^{(\text{poly})}$  in what follows.

### 2.2. Quadratic penalty approach

Our general strategy thus far [2–4] has been to maximize a penalized-likelihood objective function

$$\Phi(\mathbf{l}; \mathbf{y}) \equiv \mathcal{L}(\mathbf{l}; \mathbf{y}) - \beta R(\mathbf{l}), \quad (6)$$

where

$$\mathcal{L}(\mathbf{l}; \mathbf{y}) = \sum_{i=1}^{N_y} y_i \log \left[ \sum_{j=1}^{N_y} I_j b_{ij} e^{-l_j} + r_i \right] - \left[ \sum_{j=1}^{N_y} I_j b_{ij} e^{-l_j} + r_i \right] \quad (7)$$

is the Poisson log-likelihood for the random variables of (4) and where we have defined  $r_i \equiv s_i + \sigma_i^2 / (G_i^2 \bar{E}_i^2)$ .

The roughness penalty  $R(\mathbf{l})$  can be expressed in a general form as

$$R(\mathbf{l}) = \sum_{k=1}^K \psi_k \left( \sum_{j=1}^{N_y} t_{kj} l_j \right), \quad (8)$$

given by Fessler [18], where  $\psi_k$  is a potential function that assigns a cost to the  $K$  combinations of attenuation line integral values represented by the linear combinations  $\sum_{j=1}^{N_y} t_{kj} l_j$ .

Our quadratic penalty approach entails choosing  $\psi_k(t) = \omega_k t^2 / 2$  and constructing the  $t_{kj}$  to create differences of a sinogram sample with its horizontal and vertical neighbors, with

TABLE 1: Definition of terms in (1).

Variable	Meaning
$G_i$	Detector gain
$E_m$	Energy of $m$ th spectral bin
$b_{ij}$	Degradation coefficients
$I_i$	Number of incident photons along $i$ th attenuation line
$\lambda_m^{(i)}$	Probability of a photon incident on $i$ th attenuation line belonging to $m$ th spectral bin
$L_i$	Designates $i$ th attenuation line
$s_m^{(i)}$	Number of scattered photons of energy $E_m$ contributing to measurement $i$
$\mu(\mathbf{x}, E)$	Energy-dependent attenuation map, with $\mathbf{x}$ being spatial coordinate in patient
$d_i$	Dark current in $i$ th measurement
$\sigma_i^2$	Electronic noise in $i$ th measurement

$\omega_k = 1/2$  for those neighbors. This is equivalent to

$$R(\mathbf{I}) = \frac{1}{4} \sum_{j=1}^{N_y} \sum_{k \in \mathcal{N}_j} (l_j - l_k)^2, \quad (9)$$

where  $\mathcal{N}_j$  denotes the neighborhood comprising the 4 nearest horizontal and vertical neighbors of measurement  $j$ .

We have derived an algorithm that generates a sequence of estimates of  $\mathbf{I}$  that are guaranteed to increase the objective function of (6) by making use of the optimization transfer principal [18], in which at each iteration one defines a surrogate to the likelihood function, such that the vector of line integrals maximizing this surrogate is guaranteed to have a higher penalized likelihood than the previous vector estimate. The resulting update is

$$l_j^{(n+1)} = \left[ l_j^{(n)} - \frac{n_j + \beta \sum_{k=1}^K \sum_{i=1}^{N_y} t_{kj} t_{ki} \omega_k l_i^{(n)}}{c_j^{(n)} + \beta v_j} \right]_+, \quad (10)$$

where the notation  $l_j^{(n)}$  denotes the estimate of  $l_j$  after the  $n$ th iteration. Here,

$$n_j = \sum_{i=1}^{N_y} I_j b_{ij} \dot{g}_i \left( \sum_{j'=1}^{N_y} I_{j'} b_{ij'} e^{-l_{j'}^{(n)}} + r_i \right) e^{-l_j^{(n)}}, \quad (11)$$

where

$$\dot{g}_i(x) = y_i/x - 1, \quad v_j \equiv \sum_{k=1}^K |t_{ki}| t_k \omega_k, \quad \text{with } t_k \equiv \sum_{i=1}^{N_y} |t_{ki}|, \quad (12)$$

and the  $c_j^{(n)}$  are the curvatures of paraboloidal surrogates constructed to give rise to an overall, easy-to-maximize quadratic surrogate to the objective function. One choice for the curvatures that guarantee monotonicity is

$$c_j^{(n)} = I_j \sum_{i=1}^{N_y} b_{ij}, \quad (13)$$

although in practice we make use of a different set of curvatures that do not guarantee monotonicity but that in practice lead to faster convergence [19].

### 2.3. Median penalty

For the median penalty approach, we employ a more heuristic approach based on producing a sequence of estimates that, in the absence of a penalty, would yield a maximum-likelihood estimate, but that incorporates a penalty term in each iteration that discourages deviations from the local median of the last iteration. This is consistent with the approach of Alenius et al. in fully iterative reconstruction [11, 12]. Specifically, the update is defined as

$$l_j^{(n+1)} = \arg \max_{l_j > 0} \{S(\mathbf{I}, \mathbf{I}^{(n)}) - \beta R^{(\text{med})}(\mathbf{I}, \hat{\mathbf{m}}^{(n)})\}, \quad (14)$$

where  $S(\mathbf{I}, \mathbf{I}^{(n)})$  is a surrogate to the log likelihood to be described below and

$$R^{(\text{med})}(\mathbf{I}, \hat{\mathbf{m}}^{(n)}) \equiv \frac{1}{2} \sum_{k=1}^{N_y} \frac{(l_k - \hat{m}_k^{(n)})^2}{\hat{m}_k^{(n)}} \quad (15)$$

is the median penalty, with

$$\hat{m}_k^{(n)} = \text{Median}(\mathbf{I}^{(n)}, \mathcal{N}_k) \quad (16)$$

denoting the median of the values of  $\mathbf{I}^{(n)}$  in some neighborhood  $\mathcal{N}_k$  around value  $k$ .

The surrogate  $S(\mathbf{I}, \mathbf{I}^{(n)})$  is defined as

$$S(\mathbf{I}, \mathbf{I}^{(n)}) \equiv \sum_{k=1}^{N_y} S_k(l_k, \mathbf{I}^{(n)}), \quad (17)$$

where

$$S_k(l_k, \mathbf{I}^{(n)}) \equiv \sum_{i=1}^{N_y} \frac{I_k b_{ik} e^{-l_k^{(n)}}}{\bar{y}_i^{(n)}} g_i \left( \frac{e^{-l_k} \bar{y}_i^{(n)}}{e^{-l_k^{(n)}} \bar{y}_i^{(n)}} \right) + \frac{r_i}{\bar{y}_i^{(n)}} g_i(\bar{y}_i^{(n)}), \quad (18)$$

with

$$\bar{y}_i^{(n)} \equiv \sum_{k=1}^{N_y} I_k b_{ik} e^{-l_k^{(n)}} + r_i, \quad (19)$$

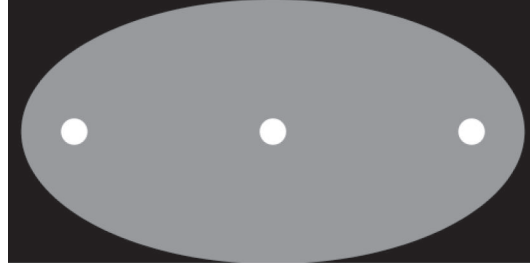


FIGURE 1: Illustration of the numerical ellipse phantom used for resolution-noise studies.

and  $g_i(x) \equiv y_i \log x - x$ . This surrogate satisfies both  $S(\mathbf{l}, \mathbf{l}^{(n)}) \leq L(\mathbf{l})$ ,  $\forall l_j \geq 0$  and  $S(\mathbf{l}^{(n)}, \mathbf{l}^{(n)}) = L(\mathbf{l}^{(n)})$ , and thus in the absence of the penalty term, finding the  $\mathbf{l}$  maximizing this surrogate necessarily increases the likelihood [4].

Substituting (17) and (15) into (14), our update is given by

$$l_j^{(n+1)} = \arg \max_{l_j > 0} \left\{ \sum_{k=1}^{N_y} S_k(l_k, \mathbf{l}^{(n)}) - \beta \frac{1}{2} \sum_{k=1}^{N_y} \frac{(l_k - \hat{m}_k^{(n)})^2}{\hat{m}_k^{(n)}} \right\}. \quad (20)$$

We can solve for the maximum by setting the derivative with respect to  $l_j$  equal to zero. Doing so yields

$$-\sum_{i=1}^{N_y} I_j b_{ij} \dot{g}_i \left( \frac{e^{-l_j}}{e^{-l_j^{(n)}}} \bar{y}_i^{(n)} \right) e^{-l_j} - \beta \left( \frac{l_j^{(n)} - \hat{m}_j^{(n)}}{\hat{m}_j^{(n)}} \right) = 0. \quad (21)$$

Solving for  $l_j$  yields the update

$$l_j^{(n+1)} = \left[ -\ln \left( \frac{\sum_{i=1}^{N_y} I_j b_{ij} \left( \left( \frac{y_i}{\bar{y}_i^{(n)}} \right) e^{-l_j^{(n)}} \right) + \beta \left( \frac{l_j^{(n)} - \hat{m}_j^{(n)}}{\hat{m}_j^{(n)}} \right)}{\sum_{i=1}^{N_y} I_j b_{ij}} \right) \right]_+. \quad (22)$$

### 3. RESULTS

#### 3.1. Qualitative results

To compare the two penalties to each other as well as to the ATM filter, we simulated projections of a numerical ellipse phantom shown in Figure 1 that we have used previously and that is modeled on the physical phantom employed by Hsieh [10]. We computed a sinogram of 1024 angles  $\times$  1024 bins of extent 0.5 mm at the isocenter with a source-to-isocenter distance of 540.0 mm. We simulated the data according to the forward model of (1) with discretization of a realistic CT spectrum into 1 keV bins. We assumed that the phantom was water-equivalent except for the three circular structures, which we assumed to be bone.

We simulated two exposure levels: a clinically typical  $I_i = 2.5 \times 10^6$  and a low-dose level  $I_i = 2.5 \times 10^5$ . We chose  $G_i = 3.57 \times 10^{-3}$  pA/keV, such that  $G_i \bar{E}_i = 0.25$  pA/quanta

for  $\bar{E}_i = 70$  keV, and  $\sigma_i^2 = 10.0$  pA<sup>2</sup> for all  $i$ . We included the effects of off-focal radiation in the simulation by convolving with kernels having 13 nonzero values arrayed diagonally with slope  $-2$  in discrete sinogram space. The central value (corresponding to the zero point of the kernel) had relative value 1.0 and the six values on either side had relative value 0.02 (these thirteen values were normalized so that their sum was 1.0). We found through simulations with water-equivalent phantoms that the beam-hardening effect of the simulated tube spectrum was well represented as a second-order polynomial  $f(l) = l - 0.007l^2$ .

We reconstructed images by means of four different approaches.

- (1) Hanning. Simple discrete deconvolution of the effect of off-focal radiation, followed by beam-hardening correction and fan-beam filtered backprojection (FFBP) reconstruction with a Hanning filter of varying cutoffs.
- (2) ATM. Presmoothing of data by means of the ATM filter, followed by simple discrete deconvolution of the effect of off-focal radiation, beam-hardening correction, and reconstruction by FFBP with an unapodized ramp filter. The ATM filter was implemented with cutoff parameter  $\lambda = 75.0$  pA and baseline parameter  $\delta = 0.05$  pA, as in [10] by Hsieh, and with the filter length varying from 3 to 19.
- (3) Quadratic. Penalized-likelihood sinogram restoration using the quadratic neighborhood penalty followed by beam-hardening correction and reconstruction by FFBP with an unapodized ramp filter. The smoothing parameter  $\beta$  was varied from 0.01 to 50.
- (4) Median. Penalized-likelihood sinogram restoration using the quadratic neighborhood penalty followed by beam-hardening correction and reconstruction by FFBP with an unapodized ramp filter. The smoothing parameter  $\beta$  was varied from 0.01 to 50. The size of the neighborhood used in median calculation was  $3 \times 3$ .

Figure 2 shows typical results of these reconstructions, where we have selected values of the smoothing parameters for the ATM and penalized-likelihood images that give approximately matched resolution at the center insert and approximately matched noise levels at the right insert, based on the resolution-variance results to be described below. It can be

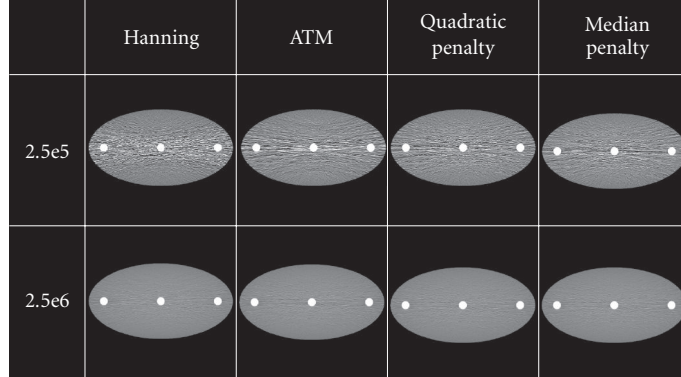


FIGURE 2: The left column illustrates reconstructions by FFBP employing a Hanning filter with cutoff 0.8 times the Nyquist frequency. The second column illustrates reconstructions by FFBP after sinogram smoothing by the ATM filter method and off-focal radiation deconvolution. The third column illustrates reconstructions by FFBP after sinogram restoration by the quadratic penalty method. The final column illustrates reconstructions by FFBP after sinogram restoration by the median penalty method. Exposures are listed at left. The window width is 400 and the level is 40.

seen that the noise level in the low-dose data leads to severe streaking artifacts in the Hanning filter reconstruction and that these are suppressed by the approaches under consideration, more so for the penalized-likelihood approaches than for the ATM approach. The results all appear to perform similarly at the higher-dose level. These qualitative impressions were explored quantitatively by use of resolution-variance studies.

### 3.2. Resolution-variance tradeoffs

To characterize resolution, we determined the local edge-spread function at the central and right high-attenuation inserts. The vertical profiles through these structures have profiles that are well fit by error functions parametrized by width  $\sigma_b$  which implies that the effective blurring kernel is Gaussian with standard deviation  $\sigma_b$ . We employ the FWHM of the Gaussian,  $2.35 \sigma_b$ , as our measure of resolution. To obtain an accurate fit, we performed targeted reconstructions of the central and right high-attenuation inserts with 0.25 mm pixel size from 10 different noise realizations. We then averaged the reconstructions together to obtain relatively low-noise profiles on which to perform the fitting. We characterized noise by calculating the average standard deviation of the pixel values in circular regions of interest (ROIs) of diameter 16.0 mm placed adjacent to, but not overlapping, the central and right high-attenuation inserts. We then plotted the resulting noise measure versus the resolution measure for the same location. Images reconstructed after smoothing with different values of the smoothing parameters  $\alpha$  or filter length  $\beta$  provide different combinations of such values and allowed us to sweep out a resolution-noise curve.

The results are given in Figure 3, where it can be seen that at the low-dose level, the two penalized-likelihood-based approaches both outperform the ATM filter in terms of resolution-noise performance. They perform very similarly to each other, with perhaps a slight advantage to the

quadratic penalty. At high-dose levels, the approaches all perform relatively similarly.

## 4. CONCLUSIONS

We have compared two different penalty choices for a penalized-likelihood sinogram-restoration strategy we have been developing, one is a quadratic penalty we have employed previously and the other is a median-based penalty. We compared the approaches to a noniterative adaptive filter that loosely but not explicitly models data statistics. We found that the two approaches produced very similar resolution-variance tradeoffs to each other and that they outperformed the ATM filter in the low-dose regime, which suggests that the particular choice of penalty in our approach may be less important than the fact that we are explicitly modeling data statistics at all.

It is not possible to conclude, of course, that the penalized-likelihood approaches would outperform any noniterative adaptive filter. In generating the resolution-variance tradeoffs for the ATM filter, we made use of the parameters  $\lambda$  and  $\delta$  given by Hsieh in describing the filter in [10] and varied the filter length parameter  $\beta$ . The filter length  $\beta$  is the most natural parameter to vary in sweeping out resolution-variance curves, but it is possible that further adjusting the parameters  $\lambda$  and  $\delta$  could further improve the achievable tradeoffs. In particular, it is possible that the version of the ATM filter implemented on GE scanners has been optimized beyond what was presented in [10].

Since the quadratic penalty allows for derivation of a monotonic algorithm guaranteed to increase the likelihood function while the median filter approach offers no such guarantee, we find it to be preferable to the median-based penalty. However, it might be worthwhile to explore the new class of median-like prior proposed by Hsiao et al. that does indeed involve maximization or minimization of a joint objective function involving the image of interest and an

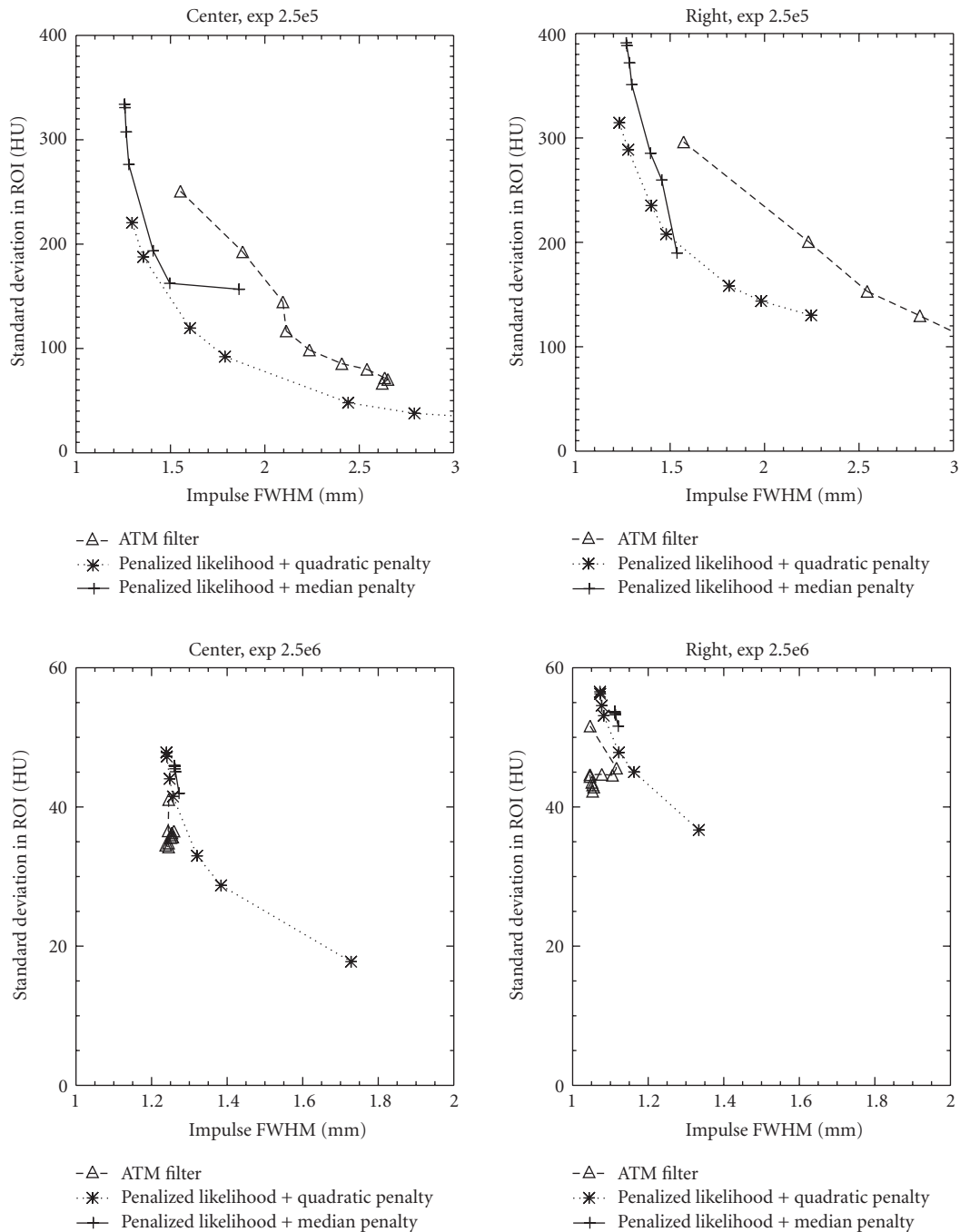


FIGURE 3: Resolution-noise tradeoffs for exposures  $2.5 \times 10^5$  and  $2.5 \times 10^6$  at the center and right circular inserts in the ellipse phantom for the three approaches under consideration.

auxiliary field derived from the local medians of the image [20]. Another possibility for future work would be to explore a penalty that uses Hsieh's ATM filter as an OSL prior much as the median prior was used here.

#### ACKNOWLEDGMENT

This work was supported by the Schewpe Foundation.

#### REFERENCES

- [1] P. J. La Rivière and D. M. Billmire, "Reduction of noise-induced streak artifacts in X-ray computed tomography through spline-based penalized-likelihood sinogram smoothing," *IEEE Transactions on Medical Imaging*, vol. 24, no. 1, pp. 105–111, 2005.
- [2] P. J. La Rivière, "Penalized-likelihood sinogram restoration for CT artifact correction," in *Proceedings of the IEEE Nuclear*

*Science Symposium and Medical Imaging Conference (NSS-MIC '04)*, vol. 5, pp. 3303–3307, Rome, Italy, October 2004, CD-ROM.

- [3] P. J. La Rivière, “Penalized-likelihood sinogram smoothing for low-dose CT,” *Medical Physics*, vol. 32, no. 6, pp. 1676–1683, 2005.
- [4] P. J. La Rivière, J. Bian, and P. Vargas, “Penalized-likelihood sinogram restoration for computed tomography,” to appear in *IEEE Transactions on Medical Imaging*.
- [5] S. Sone, S. Takashima, F. Li, et al., “Mass screening for lung cancer with mobile spiral computed tomography scanner,” *Lancet*, vol. 351, no. 9111, pp. 1242–1245, 1998.
- [6] C. I. Henschke, D. I. McCauley, D. F. Yankelevitz, et al., “Early lung cancer action project: overall design and findings from baseline screening,” *Lancet*, vol. 354, pp. 99–105, 1999.
- [7] K. Oguchi, S. Sone, K. Kiyono, et al., “Optimal tube current for lung cancer screening with low-dose spiral CT,” *Acta Radiologica*, vol. 41, no. 4, pp. 352–356, 2000.
- [8] S. Itoh, M. Ikeda, S. Arahata, et al., “Lung cancer screening: minimum tube current required for helical CT,” *Radiology*, vol. 215, no. 1, pp. 175–183, 2000.
- [9] J. Collins, “CT screening for lung cancer: are we ready yet?” *Wisconsin Medical Journal*, vol. 101, no. 2, pp. 31–34, 2002.
- [10] J. Hsieh, “Adaptive streak artifact reduction in computed tomography resulting from excessive x-ray photon noise,” *Medical Physics*, vol. 25, no. 11, pp. 2139–2147, 1998.
- [11] S. Alenius and U. Ruotsalainen, “Bayesian image reconstruction for emission tomography based on median root prior,” *European Journal of Nuclear Medicine*, vol. 24, no. 3, pp. 258–265, 1997.
- [12] S. Alenius, U. Ruotsalainen, and J. Astola, “Using local median as the location of the prior distribution in iterative emission tomography image reconstruction,” *IEEE Transactions on Nuclear Science*, vol. 45, no. 6 pt 2, pp. 3097–3104, 1998.
- [13] P. J. Green, “Bayesian reconstructions from emission tomography data using a modified EM algorithm,” *IEEE Transactions on Medical Imaging*, vol. 9, no. 1, pp. 84–93, 1990.
- [14] B. R. Whiting, “Signal statistics of x-ray computed tomography,” in *Medical Imaging 2002: Physics of Medical Imaging*, vol. 4682 of *Proceedings of SPIE*, pp. 53–60, San Diego, Calif, USA, February 2002.
- [15] I. A. Elbakri and J. A. Fessler, “Efficient and accurate likelihood for iterative image reconstruction in x-ray computed tomography,” in *Medical Imaging 2003: Physics of Medical Imaging*, vol. 5032 of *Proceedings of SPIE*, pp. 1839–1850, San Diego, Calif, USA, February 2003.
- [16] I. A. Elbakri, *X-ray CT image reconstruction using statistical methods*, Ph.D. thesis, The University of Michigan, Ann Arbor, Mich, USA, 2003.
- [17] J. Hsieh, *Computed Tomography: Principles, Design, Artifacts, and Recent Advances*, SPIE Press, Bellingham, Wash, USA, 2003.
- [18] J. A. Fessler, “Statistical image reconstruction methods for transmission tomography,” in *Handbook of Medical Imaging*, J. M. Fitzpatrick and M. Sonka, Eds., vol. 2, pp. 1–70, SPIE Press, Bellingham, Wash, USA, 2000.
- [19] H. Erdoğan and J. A. Fessler, “Monotonic algorithms for transmission tomography,” *IEEE Transactions on Medical Imaging*, vol. 18, pp. 801–814, 1999.

- [20] I. Hsiao, A. Rangarajan, and G. Gindi, “A new convex edge-preserving median prior with applications to tomography,” *IEEE Transactions on Medical Imaging*, vol. 22, no. 5, pp. 580–585, 2003.

**Patrick J. La Rivière** received the A.B. degree in physics from Harvard University in 1994 and the Ph.D. degree from the Graduate Programs in Medical Physics in the Department of Radiology at The University of Chicago in 2000. He is currently an Assistant Professor in the Department of Radiology at The University of Chicago, where his research interests include tomographic reconstruction in computed tomography, X-ray fluorescence computed tomography, and optoacoustic tomography.



**Junguo Bian** received the B.E. degree from Department of Engineering Physics at Tsinghua University, China, in 1998, and the M.S.N.E. degree from the Department of Nuclear Engineering at Purdue University in 2004. He is currently a Ph.D. student in the Graduate Programs in Medical Physics in the Department of Radiology at The University of Chicago.



**Phillip A. Vargas** received the B.S. degree in applied physics from Purdue University in 2002. He is currently a Research Technologist in the Department of Radiology at the University of Chicago, where his research interests include tomographic reconstruction in computed tomography, X-ray fluorescence computed tomography, and optoacoustic tomography.



# A Prospective Study on Algorithms Adapted to the Spatial Frequency in Tomography

Vincent Israel-Jost,<sup>1,2</sup> Philippe Choquet,<sup>2</sup> and André Constantinesco<sup>2</sup>

<sup>1</sup>*Institut de Recherche Mathématiques Avancées, 7 rue René Descartes, Université Louis Pasteur, 67084 Strasbourg Cedex, France*

<sup>2</sup>*Service de Biophysique et Médecine Nucléaire, Hôpital de Hautepierre, 1 avenue Molière, 67098 Strasbourg, France*

Received 1 December 2005; Revised 23 April 2006; Accepted 25 April 2006

The use of iterative algorithms in tomographic reconstruction always leads to a frequency adapted rate of convergence in that low frequencies are accurately reconstructed after a few iterations, while high frequencies sometimes require many more computations. In this paper, we propose to build *frequency adapted* (FA) algorithms based on a condition of incomplete backprojection and propose an FA *simultaneous algebraic reconstruction technique* (FA-SART) algorithm as an example. The results obtained with the FA-SART algorithm demonstrate a very fast convergence on a highly detailed phantom when compared to the original SART algorithm. Though the use of such an FA algorithm may seem difficult, we specify in which case it is relevant and propose several ways to improve the reconstruction process with FA algorithms.

Copyright © 2006 Vincent Israel-Jost et al. This is an open access article distributed under the Creative Commons Attribution License, which permits unrestricted use, distribution, and reproduction in any medium, provided the original work is properly cited.

## 1. INTRODUCTION

Iterative methods are increasingly used in computed tomography (image reconstruction from projections) where in most cases they advantageously replace analytical methods. The latter methods, whose success is based upon a great robustness and speed, unfortunately cannot take into account a certain number of physical and geometrical parameters which should appear in the *point spread function* (PSF). These parameters (intrinsic resolution of the detector, spatial variation of sensitivity, and others, related to specific applications) can be easily incorporated in the projection operator that models the process of imaging in iterative methods. This however does not change the nature of the problem to be solved, formulated as a large system of linear equations:

$$Ax = b, \quad (1)$$

where  $A$  is the projection operator,  $x$  is typically a set of (unknown) values taken by the voxels in the 3D space (attenuation coefficients, activity ...), and  $b$  is the set of measurements, often organized as a set of projection images.

In addition, besides the exponential growth in computer processing power that obviously plays an important role in the feasibility of large computations, solving methods for (1) profit from a broad effort realized in general inverse prob-

lems methods and from a continuous exchange between theory and applications.

One important ongoing study on the speed of convergence is contingent on the consideration of different algorithms (*algebraic reconstruction technique* (ART) [1], *simultaneous algebraic reconstruction technique* (SART) [2], *expectation maximization* (EM) [3], or conjugated gradient for the most famous), different types of implementation (sequential (Seq), simultaneous (Sim), or block-iterative (BI)), regularizations, or relaxation parameters (see [4] for details). A solid mathematical framework was formed, which in most cases tendered proof of convergence, including at times for the inconsistent case—generally that of computed tomography.

The idea of the work presented here has risen from the fact that the high frequencies (the details) are always reconstructed after the low frequencies in iterative methods for computed tomography. In the case of highly detailed objects (in a sense that we will later specify), an important number of iterations might be required to obtain the precision expected on the reconstructed image. This very general fact has been experienced by all who worked with iterative algorithms, and keys for the understanding of this phenomena can be found in [5], but in a framework of integral geometry resulting in a Dirac projection PSF and thus quite different from our context.

In this article, we propose a way to accelerate the convergence of iterative methods in the specific case of highly detailed objects, based on the use of an incomplete backprojection operator. This can be roughly formulated as a weighting of each correction  $d_{i,j}^k$  of voxel  $j$  by equation  $i$  during the  $k$ th iteration with weights  $w_{i,j}^k$  such as  $\sum_i w_{i,j}^k = 1$  for all  $j$  and  $k$  and the *incomplete backprojection condition* (IBC):

$$w_{i,j}^k = 0 \quad \text{for some } i, \text{ even if } A_{i,j} \neq 0. \quad (2)$$

To our knowledge, this condition has not been thus far reported in the use of reconstruction algorithms for computed tomography. Besides the formulation of a frequency adapted (FA) algorithm that realizes the reconstruction with IBC starting from the well-known SART algorithm, a major concern of this paper is to explain how the IBC permits to accelerate the convergence by updating the value of the voxels from the most relevant measurements and to give experimental results to support both the convergence of the algorithm and the gain obtained when compared to SART.

In Section 2, we describe the type of problems for which we believe the adaptation involved by the IBC can be useful and formulate the IBC in terms of projections onto convex sets. We explain the IBC for it to realize the expected acceleration and give an adaptation of the simultaneous algebraic reconstruction technique (SART) algorithm of Andersen and Kak [2] modified by the IBC. In Section 3, we show results on simulations, phantom, and small animal with a comparison between SART and FA-SART. Section 4 is a discussion on the proposed method which also suggests a number of different use for FA algorithms and Section 5 concludes the paper.

## 2. BUILDING AN ALGORITHM ADAPTED TO THE SPATIAL FREQUENCY

In computed tomography like in other applications leading to inverse problems, a set of discrete measurements is physically obtained, presumably by the application of some linear operator  $A$  to a studied object, discretized into a set of unknowns. For each unknown  $x_j$  (a voxel in tomography), the point spread function (PSF) (we should actually talk about the voxel spread function) appears in the column  $A_{\bullet,j}$  of the matrix  $A$  whose coefficients are assumed to be nonnegative here, to simplify the notations.

For some imaging techniques, the paradigmatic case of which is single photon emission computed tomography (SPECT), this PSF is always different from a Dirac function since it notably includes the detector components (collimator, scintillator, photo-multipliers, electronic boards, etc.). Indeed, the photons emitted from a voxel  $j$  reach far more than one single pixel on the detector and one has to take this into account in the matrix  $A$  when modeling this problem. PSF in SPECT is generally modelled by discretized Gaussian functions but some authors proposed more elaborate models, especially for pinhole SPECT (see Metzler et al. [6]).

But whatever the chosen model is, the actual situation is that two close voxels have many measurements in com-

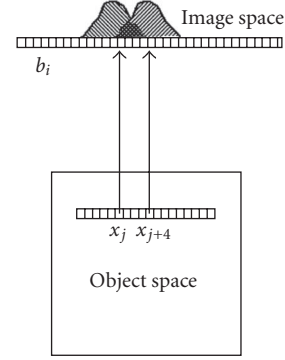


FIGURE 1: Overlapping between two close voxels' PSF. The darkest zone will be used to reconstruct voxel  $x_j$  as well as  $x_{j+4}$  (and all those in between), thus leading to a smoothed reconstruction after only a few iterations.

mon in their PSF (see Figure 1). This may result in a slow rate of convergence: the backprojection of these shared measurements leads to a smoothing for the voxels' values, that only tends to vanish as the number of iterations increases. This is not necessarily inadequate since when a large and homogeneous structure is to be imaged, this smoothing will mainly reduce the noise if one stops the iterations before the noise is reconstructed (Figure 2(a)). But when considering an image of projection with high frequencies, using these shared measurements in the backprojection, or at least the furthest away from the center of the PSF, will hold the voxels' values distant from the solution  $x^*$  for a certain number of iterations (Figure 2(b)). Throughout this paper, we will characterize highly detailed objects in an informal manner by reference to this figure, that is, when significant details of the image are of the same size or smaller than the PSF's width.

Our idea is to only use the most central measurements of the PSF to accelerate the convergence in the case of imaging with high spatial frequencies. To do so, we considered the SART algorithm whose iteration is

$$x_j^{k+1} = x_j^k + \frac{\lambda}{\sum_{i=1}^M A_{i,j}} \sum_{i=1}^M \frac{b_i - (Ax^k)_i}{\sum_{j=1}^N A_{i,j}} A_{i,j}, \quad (3)$$

where  $j = 1, \dots, N$  indexes the voxels and  $i = 1, \dots, M$  indexes the pixels so that  $x^k \in \mathbb{R}^N$  for all  $k$ ,  $b \in \mathbb{R}^M$ ,  $A$  is an  $M \times N$  matrix modelling the problem and  $\lambda$  is the relaxation parameter. This can also be written in a matrix form discussed by Jiang and Wang [7] ( $T$  denotes the transpose of a matrix or a vector):

$$x^{(k+1)} = x^{(k)} + \lambda V A^T W (b - Ax^{(k)}), \quad (4)$$

with  $V = \text{diag}(1/\sum_{i=1}^M A_{i,j})$  an  $N \times N$  diagonal matrix and  $W = \text{diag}(1/\sum_{j=1}^N A_{i,j})$  an  $M \times M$  diagonal matrix. We also assume the conditions  $\sum_{i=1}^M A_{i,j} \neq 0$  for all  $j$  and  $\sum_{j=1}^N A_{i,j} \neq 0$  for all  $i$ .

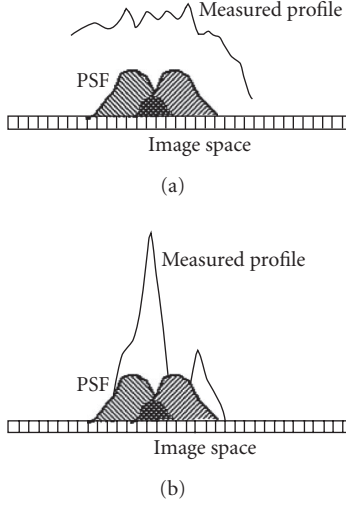


FIGURE 2: Comparison of the two main cases, when a profile corresponding to a large and homogeneous structure is measured with noise (a), and when the measured profile corresponds to a highly detailed object (b). On (a), using all the discrete measurements of voxel's PSF will smooth the reconstruction which will reduce the noise. On (b), "important" high frequencies are smoothed and more iterations will be needed to achieve an accurate reconstruction.

Although this might sound antinomic with the *simultaneous* of SART, we can write a component Seq form of SART

$$x_j^{k+1} = x_j^k + \lambda \frac{b_i - \langle a^i, x^k \rangle}{\|a^i\|_1} \mathbf{1}_{a_j^i > 0} \quad (5)$$

that can be derived from the analysis presented in [8] by Censor and Elfving. Then, applying this algorithm in the matrix form of (4), it is well known that the new estimate  $x^{k+1}$  is the projection of  $x^k$  onto the hyperplane  $H_i = \{x \in \mathbb{R}^N / \langle a^i, x \rangle = b_i\}$  if  $\lambda = 1$ .

This is our starting point for a frequency adapted algorithm based on SART. For the purpose of the incomplete backprojection condition, given  $0 \leq \rho \leq 1$ , let  $A^\rho$  denote the matrix

$$A^\rho := \begin{cases} A_{i,j} & \text{if } A_{i,j} \geq \rho \cdot \|A_{\bullet,j}\|_\infty, \\ 0 & \text{otherwise,} \end{cases} \quad (6)$$

so that  $A^\rho$  only keeps in each column the coefficients of  $A$  higher than  $\rho$  times the top of the PSF. We also define the matrix  $V^\rho := \text{diag}(1/\sum_{i=1}^M A_{i,j}^\rho)$  and  $W^\rho := \text{diag}(1/\sum_{j=1}^N A_{i,j}^\rho)$ . Then, following (4) we define the next iterate corresponding to the treatment of a single projection  $i$  as

$$x^{(k+1)} = x^{(k)} + \lambda V^\rho A^{\rho T} W^\rho (b - Ax^{(k)}) = P_i^\rho(x^k). \quad (7)$$

It can be shown in the exact same manner as for (4) (in the sequential case) that  $P_i^\rho(x)$  projects  $x$  onto the hyperplane  $H_i$ . But (7) is also designed to have  $P_i^\rho(x)$  in the affine

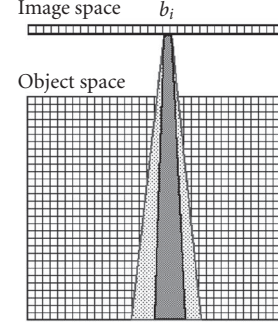


FIGURE 3: The original backprojection cone corresponding to a pixel  $b_i$  and composed of voxels  $v_j$ , such as  $A_{i,j} > 0$  (light grey), is replaced by a set of voxels, such as  $A_{i,j} > \rho \cdot \|A_{\bullet,j}\|_\infty$  (dark grey).

subspace of  $\mathbb{R}^N$ :

$$\Omega_i^k = \left\{ x \in \mathbb{R}^N / P_i^\rho(x)_j = x_j \quad \forall j / A_{i,j} < \rho \cdot \|A_{\bullet,j}\|_\infty \right\} \quad (8)$$

thus projecting the current estimate onto  $C_i^k := H_i \cap \Omega_i^k$ , which is a closed convex set of  $\mathbb{R}^N$ .

Now, we want to consider the scheme (7) in its natural case, that is, simultaneous. Thus we change the iteration (3) for the following.

*Algorithm 2.1* (FA-SART).

$$x_j^{k+1} = x_j^k + \frac{\lambda}{\sum_{i=1}^M A_{i,j}^\rho} \sum_{i=1}^M \frac{b_i - (Ax^k)_i}{\sum_{j=1}^N A_{i,j}^\rho} A_{i,j}^\rho. \quad (9)$$

The BI version requires some sophistication in the notations and for this purpose, we adopt pretty much the same ones as Censor and Elfving in [8]. Let then  $T$  be the number of blocks and, for  $t = 1, 2, \dots, T$ , let the blocks of indices  $B_t \subseteq \{1, 2, \dots, M\}$  be an ordered subset of the form  $B_t = \{l_1^t, l_2^t, \dots, l_{M(t)}^t\}$ , where  $M(t)$  is the number of elements in  $B_t$ . In our case, we define  $T = M$  and for each  $t$ ,  $B_t = \{t\}$ . For  $t = 1, 2, \dots, T$ , let  $A_t$  denote the matrix formed by taking all the rows  $\{a^i\}$  of  $A$  whose indices belong to the block of indices  $B_t$ , that is,  $A_t := a^t$ . The same applies to  $A^\rho$  with  $A_t^\rho$  the matrix formed by taking all the rows  $\{\tilde{a}^i\}$  of  $A^\rho$  whose indices belong to the block of indices  $B_t$  and  $\tilde{a}_c^{j,t(k)}$  the  $j$ th column of  $A_t^\rho$ .

The vector  $b$  is partitioned similarly with  $b^t$  denoting the elements of  $b$  whose indices belong to the block of indices  $B_t$ , that is,  $b^t := b_t$ . Let us also denote  $a_c^{j,t(k)}$  the  $j$ th column of  $A_t$ , then the BI FA-SART writes as follows.

*Algorithm 2.2* (BI FA-SART).

$$x_j^{k+1} = x_j^k + \frac{\lambda}{\|\tilde{a}_c^{j,t(k)}\|_1} \sum_{i=1}^{M(t(k))} \frac{b_i^{t(k)} - \langle a^{i,t(k)}, x^k \rangle}{\|\tilde{a}^{i,t(k)}\|_1} \tilde{a}_j^{i,t(k)}. \quad (10)$$

These algorithms realize a backprojection characterized by a contracted cone compared to the original SART (see Figure 3).

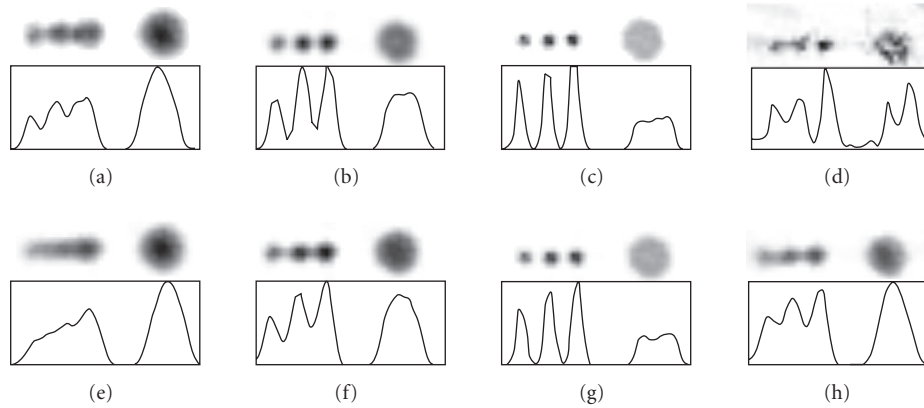


FIGURE 4: Simulation with a computed phantom composed of three small spots and a bigger structure. (a)–(d) show results obtained with the FA-SART algorithm,  $\rho = 1$ , and (e)–(h) show results with the SART algorithm (which is FA-SART with  $\rho = 0$ ). The pinhole aperture was 2.5 mm for (a) and (e), 1.5 mm for (b) and (f), 0.025 mm for (c) and (g), and 1.5 mm with noise added onto the projections for (d) and (h). These results show improvements with FA-SART when the PSF is large (2.5 mm and 1.5 mm) and better images with SART when the data are noisy (Gaussian noise, 20% of the maximum of the data), especially for big structures. No significant difference is visible when the PSF is small, because the stage of deconvolution is of less importance during the reconstruction process.

### 3. RESULTS

#### 3.1. Material and method

The applications shown here are simulations and pinhole SPECT acquisitions made on a small animal single head dedicated SPECT gamma camera (Gaede Medizinsysteme GMBH, Freiburg, Germany) with a 6.5 mm NaI(Tl) crystal 25 photomultipliers and a small field of view of 17 cm  $\times$  17 cm. The camera was equipped with a tungsten pinhole collimator of 120 mm in focal length and 1.5 mm in diameter for the phantom, 2 mm in diameter for the mouse study. A more complete description of the device, as well as results on small animal imaging can be found in [9]. Prior to reconstruction, we used a correction of the center of rotation applied on the projections after measurement of the defect on a single-line-source phantom as described in [10]. Both the FA-SART and SART algorithms were block iterative with each block corresponding to a different image of projection.

#### 3.2. Simulation

The simulation performed here on a computed phantom illustrates the typical behavior of the FA-SART algorithm, which accelerates the convergence when the PSF is large (see Figures 4(a), 4(b) and 4(e), 4(f)). For a thin PSF, no visible difference appears since FA-SART acts on the deconvolution. Bigger structures should not be reconstructed with  $\rho$  close to 1 from noisy data to avoid having the high frequencies of the noise emphasized. Three iterations were computed for all reconstructions.

#### 3.3. Phantom

A phantom, seen in Figure 5, with three types of cylindrical cavities (diameters 1 mm, 1.5 mm and 2 mm separated with the same distance), was filled with  $^{99m}\text{Tc}$ , 20 MBq activity.

The parameters for the acquisition were 30 mm radius of rotation, 60 projections of  $64 \times 64$  pixels on  $180^\circ$  and 1 minute per projection. For the comparison in Figures 5(b)–5(d), we used the FA-SART algorithm with  $\rho = 1$  and the SART algorithm (which is FA-SART with  $\rho = 0$ ). For this highly detailed object, the FA-SART reconstruction (5(b)) does better than 3 iterations of SART (5(c)) or even 10 iterations (5(d)), due to an important smoothing effect during the first iterations. Figure 5(e) provides a promising way to use FA-SART in a preconditioning of system (1). It shows a reconstruction obtained after 3 iterations of FA-SART ( $\rho = 1$ ) followed by 2 iterations of SART.

#### 3.4. Cardiac mouse imaging

For mouse heart perfusion, a normal adult female CD1 mouse (Mouse Clinical Institute, Ilkirch, France) weighting 30 g was injected with 400 MBq of  $^{99m}\text{Tc}$ -Tetrofosmin (Amersham, General Electric Healthcare, USA). The radius of rotation of the camera was 2.5 cm corresponding to a zoom factor of 5 and 48 projections of  $64 \times 64$  pixels were acquired over  $180^\circ$  (see [9] for details). Figure 6 demonstrates a satisfying result with FA-SART and  $\rho = 0.8$  that makes both the left and right ventricles visible.

### 4. DISCUSSION

From the obtained results, it seems that the FA-SART algorithm is able to reconstruct high details in less iterations than SART. While the reconstructions performed from physical structures (phantom and animal) show a faster convergence to what seems to be the true distribution, those performed from simulated data demonstrate that this acceleration increase with the PSF's width of the system, that is, when the intrinsic resolution decreases. These simulations also prove that the improvement obtained with the FA-SART algorithm

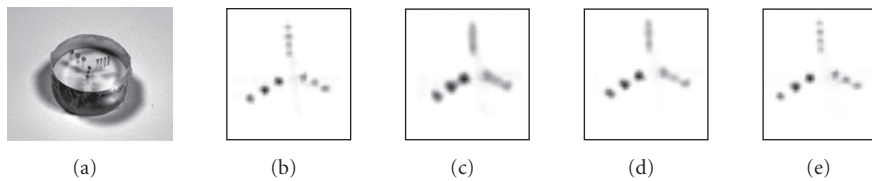


FIGURE 5: Photo of the phantom with 3 types of cavities (diameters 1 mm, 1.5 mm, and 2 mm separated by the same distance) which can be filled with a radioactive tracer (a). Transaxial slices of the reconstructed phantom with 3 iterations of FA-SART and  $\rho = 1$  (b), 3 iterations of SART (c), and 10 iterations of SART (d). Figure (a) shows significant improvements even when compared with 10 iterations of SART. Figure (e) shows the result obtained from an interesting combination of the two algorithms: 3 iterations of FA-SART ( $\rho = 1$ ) followed by 2 iterations of SART.

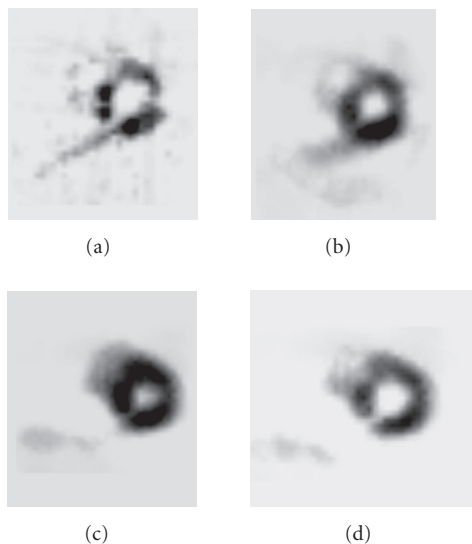


FIGURE 6: Normal mouse heart perfusion. Reconstruction with 3 iterations of FA-SART,  $\rho = 1$  (a), 3 iterations of FA-SART,  $\rho = 0.8$  (b), 3 iterations of SART (c), and 10 iterations of SART (d).

is not due to an inadequacy of the matrix  $A$  that models the system. Thus, the method only applies to a class of problems with large PSF, that is, involving an important step of deconvolution like SPECT or optical tomography. It would make no sense, for those applications where the PSF is close to a Dirac function like in computed tomography scanning, to contract the backprojection cone since this cone is already almost a line. It should also be recalled that the gain obtained on highly detailed structures is balanced by a loss in large and homogeneous structures, for which the smoothing properties of the SART algorithm reduce the noise. On the contrary, using the FA-SART algorithm with a high threshold  $\rho$  would increase the noise by emphasizing the high frequencies in the reconstruction.

This leads to the major difficulty of such an algorithm: how it should be used. We have shown results with a same value for  $\rho$  for all the voxels and all the iterations. This is a first way to accommodate to the FA-SART: the context of SPECT is that of functional imaging, in which in general only one structure is considered interesting. Thus, even if several structures appear in the same image, the parameter  $\rho$  can be

set to a value corresponding to a given organ or a type of examination (myocardial perfusion produces a sharper image of the heart than blood-pool imaging so these two explorations of the same organ would require different values of  $\rho$ ). This has been for the most part our way to proceed thus far, although other uses can be considered.

A use in preconditioning of the system (1) with two or three iterations of FA-SART followed by a solving with the SART algorithm seems to combine the best of these two algorithms by providing both a fast reconstruction of the high frequencies and an adequate rendering of the bigger structures. Also a value of  $\rho$  adapted to the local frequencies of the projection images might successfully change the local properties of the reconstruction, with a high value of  $\rho$  only when high-frequencies are detected. We started to investigate this way by creating local frequencies maps of the projection images composed of wavelets coefficients and this will constitute the base of our further works.

A noticeable positive point of the FA-SART algorithm is that it requires very few adaptations when SART has already been implemented. On a programming point of view, certain loops are just partially executed, which also means that one iteration of FA-SART is slightly faster than one of SART.

Since the backprojection operation significantly differs from other studied algorithms, it is by no means obvious to deduce that the FA-SART algorithm converges from an analysis of SART or of the general Landweber scheme. Results concerning the convergence have nevertheless been greatly improved by the suggestion of an anonymous referee and a paper dedicated to a mathematical analysis will be presented elsewhere for publication. This theoretical work will support the experimental evidences shown here, with a study of the convergence of the algorithm but also of its behavior in function of the main frequency.

## 5. CONCLUSION

The FA-SART algorithm has been designed to be able to change the usual rate of convergence of iterative algorithms. While low frequencies are generally the first reconstructed, we permitted to invert this phenomenon in order to have the details appear in the image after very few iterations. We evidenced this behavior of the FA-SART algorithm by showing applications and proposed several possible ways to use

it. Theoretical questions will be discussed in a forthcoming paper.

## ACKNOWLEDGMENTS

This work has been permitted by a very profitable collaboration between the Institute of Advanced Research in Mathematics and the Service of Biophysics and Nuclear Medicine in Strasbourg, thanks to Cyrille Blondet, Eric Sonnendrücker, and Stéphanie Salmon. All of our thanks and acknowledgement to Ariel Bardi from Bard College, NY, USA, for assistance in English.

## REFERENCES

- [1] R. Gordon, R. Bender, and G. T. Herman, "Algebraic reconstruction techniques (ART) for three-dimensional electron microscopy and X-ray photography," *Journal of Theoretical Biology*, vol. 29, no. 3, pp. 471–481, 1970.
- [2] A. H. Andersen and A. C. Kak, "Simultaneous algebraic reconstruction technique (SART): a superior implementation of the art algorithm," *Ultrasonic Imaging*, vol. 6, no. 1, pp. 81–94, 1984.
- [3] A. Dempster, N. Laird, and D. Rubin, "Maximum likelihood from incomplete data via the EM algorithm," *Journal of the Royal Statistical Society, Series B*, vol. 39, no. 1, pp. 1–38, 1977.
- [4] Y. Censor and S. A. Zenios, *Parallel Optimization: Theory, Algorithm, and Optimization*, Oxford University Press, New York, NY, USA, 1997.
- [5] S. J. Norton, "Iterative reconstruction algorithms: convergence as a function of spatial frequency," *Journal of the Optical Society of America A*, vol. 2, no. 1, pp. 6–13, 1985.
- [6] S. D. Metzler, J. E. Bowsher, K. L. Greer, and R. J. Jaszczak, "Analytic determination of the pinhole collimator's point-spread function and RMS resolution with penetration," *IEEE Transactions on Medical Imaging*, vol. 21, no. 8, pp. 878–887, 2002.
- [7] M. Jiang and G. Wang, "Convergence studies on iterative algorithms for image reconstruction," *IEEE Transactions on Medical Imaging*, vol. 22, no. 5, pp. 569–579, 2003.
- [8] Y. Censor and T. Elfving, "Block-iterative algorithms with diagonally scaled oblique projections for the linear feasibility problem," *SIAM Journal on Matrix Analysis and Applications*, vol. 24, no. 1, pp. 40–58, 2003.
- [9] A. Constantinesco, P. Choquet, L. Monassier, V. Israel-Jost, and L. Mertz, "Assessment of left ventricular perfusion, volumes, and motion in mice using pinhole gated SPECT," *Journal of Nuclear Medicine*, vol. 46, no. 6, pp. 1005–1011, 2005.
- [10] K. Ogawa, T. Kawade, J. Jolkkonen, K. Nakamura, A. Kubo, and T. Ichihara, "Ultra high resolution pinhole SPECT for small animal study," *IEEE Transactions on Nuclear Science*, vol. 45, no. 6, part 2, pp. 3122–3126, 1998.

**Vincent Israel-Jost** received his M.S. degree in applied mathematics in 2002 and his Engineer degree from Ecole Nationale Supérieure de Physique de Strasbourg, France. Currently, he is a doctorate student in applied mathematics at the Biophysics and Nuclear Medicine Department of CHU Hautepierre, and the Institute of Research in Advanced Mathematics at Université Louis Pasteur, both in Strasbourg, France.



His work concerns the production or improvement of iterative algorithms in cone-beam SPECT. His research interests include iterative algorithms and image processing, as well as philosophy of science and image depiction. He is now pursuing a second Master's degree in the philosophy of science from the University of Paris I - La Sorbonne.

**Philippe Choquet**, veterinary since 1988, got a predoctoral degree in medical imaging and signal processing in 1991, and a Ph.D. degree dissertation in 1996. Since 2001, he has been an Associate Professor in the Biophysics and Nuclear Medicine Department, CHU Hautepierre, Strasbourg. He is the author and coauthor of 29 papers in peer-reviewed journals as well as 76 oral and poster communications in national and international meetings in the field of low field MRI, NMR, and MRI of hyperpolarized gases and small animal scintigraphy.



**André Constantinesco** got the Master's degree in physics (1969), Ph.D. degree in physics (1976). He has been an MD since 1977 and a Nuclear Medicine Specialist since 1980 from Université Louis Pasteur of Strasbourg, France. He has been a Professor of biophysics and nuclear medicine since 1981 and Director of the Service de Biophysique et Médecine Nucléaire at Hautepierre University Hospital in Strasbourg since 1997. He is the author and coauthor of 176 publications and 277 oral or poster presentations in the fields of blood haemodynamics, biomechanics, medical instrumentation, nuclear medicine, low field MRI, hyperpolarized xenon MRI, and molecular imaging.



# Assessment of Left Ventricular Function in Cardiac MSCT Imaging by a 4D Hierarchical Surface-Volume Matching Process

Mireille Garreau,<sup>1</sup> Antoine Simon,<sup>1</sup> Dominique Boulmier,<sup>2</sup> Jean-Louis Coatrieux,<sup>1</sup> and Hervé Le Breton<sup>1,2</sup>

<sup>1</sup>Laboratoire Traitement du Signal et de l'Image, INSERM U642, Université de Rennes 1, Campus de Beaulieu, 35042 Rennes, France

<sup>2</sup>Service d'Hémodynamique et de Cardiologie Interventionnelle, Centre Cardio-Pneumologique, CHU Pontchaillou, 35033 Rennes, France

Received 1 December 2005; Revised 16 March 2006; Accepted 9 April 2006

Multislice computed tomography (MSCT) scanners offer new perspectives for cardiac kinetics evaluation with 4D dynamic sequences of high contrast and spatiotemporal resolutions. A new method is proposed for cardiac motion extraction in multislice CT. Based on a 4D hierarchical surface-volume matching process, it provides the detection of the heart left cavities along the acquired sequence and the estimation of their 3D surface velocity fields. A Markov random field model is defined to find, according to topological descriptors, the best correspondences between a 3D mesh describing the left endocardium at one time and the 3D acquired volume at the following time. The global optimization of the correspondences is realized with a multiresolution process. Results obtained on simulated and real data show the capabilities to extract clinically relevant global and local motion parameters and highlight new perspectives in cardiac computed tomography imaging.

Copyright © 2006 Mireille Garreau et al. This is an open access article distributed under the Creative Commons Attribution License, which permits unrestricted use, distribution, and reproduction in any medium, provided the original work is properly cited.

## 1. INTRODUCTION

Cardiovascular diseases cause the death of 17 million people every year, representing the major cause of mortality in industrialized countries. Various cardiac functional parameters are used to guide diagnosis, treatment, and followup of these diseases. The most used indicators (left ventricle volume (LVV), left ventricular mass (LVM), ejection fraction (EF)) provide information about the heart global function, but the detection and the treatment of some pathologies, such as atherosclerosis, would need the precise quantification of cardiac motion and deformation. Technological improvements in cardiac imaging provide rich opportunities for such a progress.

The minimally invasive assessment of heart motion has therefore been studied from modalities providing four-dimensional (4D) data sets. Magnetic resonance imaging (MRI), with cine MRI [1] and especially tagged MRI [2–4] and phase contrast MRI [5], has been extensively used, giving access to mid-wall deformations. However, its limited spatial resolution and long acquisition time prevent MRI

to image both cardiac motion and coronary arteries. Ultrasound images [6, 7] providing, with high availability, cardiac sequences of high temporal resolution, are still limited by their low signal-to-noise ratio in spite of the recent advances of real-time 3D echocardiography. ECG-gated single photon emission computed tomography (SPECT) and positron emission tomography (PET) in spite of lower spatial and temporal resolutions have also been used in order to combine perfusion and contractility informations [8, 9]. The emergence of electron-beam computed tomography and of the dynamic spatial reconstructor (DSR) has provided opportunities for cardiac motion estimation [10–12], but their availability is still very limited. See [13] for an exhaustive review of cardiac image functional analysis methods.

The recent significant advances of multislice computed tomography (MSCT), with the introduction of ultra-fast rotating gantries (0.5 s/tr), multirows detectors, and retrospective ECG-gated reconstructions, provide high contrast and spatiotemporal resolutions and allow a huge progress towards the imaging of moving organs. These advances allow the observation of all cardiac structures simultaneously,

for successive instants of the cardiac cycle, under one single breathhold. Some studies have been conducted in MSCT for the detection of coronary diseases [14, 15], but very few works have been realized for the quantitative 3D cardiac motion estimation [16].

The issue of nonrigid motion estimation from 3D images is one of the most important challenges of computer vision. Methods which have been proposed for this purpose can be classified into three kinds of approaches. In geometric model-based approaches, parametric models [3, 17, 18] involve the parametric formulation of the object and/or of the movement. This kind of methods is interesting to extract global motion and to represent it with few parameters. Non-parametric models [10, 19, 20], using mainly mass-spring and finite element methods, extract local motion using differential constraints. Optical flow methods [2, 11, 21, 22] are mostly based on intensity conservation and motion smoothing constraints. That constraint of intensity conservation with time is difficult to advance with MSCT data because of the contrast agent diffusion combined with the retrospective reconstruction of the sequence. Furthermore, these methods providing dense motion fields are difficult to handle with big data volumes in which the study deals with only few objects. Feature matching methods [1, 23, 24] are based on the search of correspondences between entities (considered at following times) according to descriptive parameters. These methods enable focusing the study on the objects of interest and extracting local motion. However, most of them are highly dependent from the segmentation quality because they need an accurate segmentation for each instant of the studied sequence.

We propose a new method to jointly extract ventricular shapes and their motion from cardiac MSCT images in one unique process. This problem of dual 3D shape and motion estimation is handled by a statistical approach provided by a Markov random field (MRF) [25], associated to a multiresolution process. The MRF theory has been extensively used in computer vision [26, 27]. Its application to motion analysis has mostly been done with optical flow estimation [28] and deformable models [29, 30].

In this paper, the 3D sparse nonrigid motion field to estimate at each time instant is formulated, in a Bayesian framework, as a Markov random field model under spatiotemporal regularity hypotheses. This motion field is provided by a matching method based on features of different types which are surface 3D mesh nodes at a first time instant and image voxels at the following time instant. These extracted motion fields can then be used for global and local motion quantification and interpretation. Results obtained on simulated and real data give satisfying results.

In the remainder of this paper, we describe in Section 2 the hierarchical surface-volume matching method we have developed including the preprocessing step, the definition of the Markov random field model and its application in a multiscale process, and the optimization stage. In Section 3 we present the results obtained on simulated and real data before concluding in Section 4.

## 2. A 4D HIERARCHICAL MOTION ESTIMATION METHOD

From a time sequence of 3D MSCT cardiac images, our approach allows the spatiotemporal detection of the left heart cavities and the quantification of their deformations. This is achieved by a multiscale matching method which provides, along the whole sequence, the correspondences between a 3D surface mesh extracted at one time instant and the 3D volume available at the next time instant. The overall method includes the following steps:

- (a) a 3D segmentation step and a surface reconstruction process are first applied to only one 3D image of the time sequence (at time  $t_0$ ) to provide the first surface of the sequence;
- (b) a hierarchical surface-volume matching process is applied to estimate a 3D motion field between the surface at time  $t_0$  and the next volume at time  $t_1$ ;
- (c) from the surface at time  $t_0$  and the estimated motion field, a new 3D surface can be estimated at time  $t_1$ ;
- (d) steps (b) and (c) are repeated until all images of the sequence are processed.

In order to obtain the mesh corresponding to the first considered time of the sequence, step (a) is decomposed in this way: a segmentation tool, based on a 3D region growing process bounded by a gradient information, is applied [31]. The segmented surface is then reconstructed using the marching cubes algorithm. Finally, in order to prepare the matching process, the resulting surface mesh is regularized in such a manner that each node coordinates correspond to one volume voxel coordinates.

Surface estimation (step (c)) relies on the deformation of the surface corresponding to time  $t_0$  with the motion estimated between times  $t_0$  and  $t_1$ . A regularization step is then performed in order to fill mesh holes and to suppress redundant nodes.

The 3D motion field estimation (step (b)) is performed by a matching process applied between the surface representing the endocardium at time  $t_0$  and the original volume corresponding to the next time  $t_1$ . A hierarchical process is used to gain both in terms of result quality and of computational efficiency. The matching process will firstly be described at one resolution, then the multiresolution scheme will be detailed.

### 2.1. A surface-volume matching process

In order to estimate the motion between one surface corresponding to time  $t_0$  and a volume corresponding to the following time  $t_1$ , a surface-volume matching method has been developed.

A feature matching problem implies choosing the entities to match and to define local energies which can be combined to provide a distance measure between entities. As in almost all motion estimation issues, this measure is not sufficient to deal with a well-posed problem. It is therefore necessary to add contextual constraints. The best correspondences of

selected entities can finally be obtained from the minimization of global energy.

One original contribution of this method is to establish correspondences between spatial entities which are not of the same nature: the matching process is conducted between 3D mesh nodes on the one hand and image voxels on the other hand.

The 3D motion field to compute between two successive instants is considered as a realization  $f = \{f_i/i = 1, \dots, N_S\}$  of a 3D random field  $F$  ( $N_S$  being the number of considered sites in the field). The set of sites  $S$  of the field  $F$  is given by all the 3D mesh nodes at time  $t_0$ . The labels assigned to these sites, expressed by the  $f_i$  estimations, are given by the voxels found (at time  $t_1$ ) in best correspondence with the 3D nodes.

According to Bayes' theory, the posterior probability of the realization  $f$  according to the observation  $d$  (the mesh nodes at time  $t_0$  and the voxels at time  $t_1$ ) is given by

$$p(f | d) = \frac{p(f)p(d | f)}{p(d)}, \quad (1)$$

with  $p(f)$  the prior probability,  $p(d | f)$  the conditional probability of the observation process  $d$ , and  $p(d)$  the observation probability which is considered independent of  $f$ . According to the maximum a posteriori (MAP) estimator, the most probable realization  $f$  is provided by the maximization of the a posteriori probability  $p(f | d)$ , with  $p(f | d) \propto p(f)p(d | f)$ .

The mechanical properties of the heart induce a spatiotemporal regularity of the motion field. To capture the spatial regularity of this motion,  $p(f)$ , used to model an a priori of the considered random field, is defined considering  $F$  as a Markov random field.

This Markov random field (MRF) is defined in relation to a neighborhood system  $\mu$ . According to this definition, the neighborhood associated to one node  $s$ , noted  $\mu_s$ , is given by all nodes which share a common edge with the node  $s$ .

The MRF conditional probability models the local properties of the field according to this neighborhood. It is given by

$$p(f_s | f_{S-\{s\}}) = p(f_s | f_{\mu_s}). \quad (2)$$

From the neighborhood  $\mu$ , a set of cliques  $C$  is defined as including all pairs of neighboring nodes:

$$C = \{\{s, t\} \in S^2, t \in \mu_s\}. \quad (3)$$

According to the Hammersley-Clifford theorem [32], the Markov random field  $F$  in relation to the neighborhood system  $\mu$  is also a Gibbs random field in relation to  $\mu$ . The prior probability distribution function is then given by

$$p(f) = \frac{1}{Z} \exp \{-U_R(f)\}, \quad (4)$$

with  $Z$  a normalization constant and  $U_R(f)$  a global energy function defining the interactions between the sites.  $U_R(f)$  represents the internal energy of the random field and has a regularization effect. It is defined as

$$U_R(f) = \sum_{c \in C} V_R(c, f^c), \quad (5)$$

$V_R(c, f^c)$  being the local interaction potential defined for each clique  $c$  and its associated labels  $f^c = \{f_s, s \in c\}$ . More precisely, we define  $V_R$  by

$$V_R(c, f^c) = \alpha_R \frac{\|\vec{f}_s - \vec{f}_t\|}{\text{dist}(s, t)} \quad \forall c = \{s, t\} \in C, \quad (6)$$

where  $\alpha_R$  is a weighting factor, constant for every clique,  $\vec{f}_s$  (resp.,  $\vec{f}_t$ ) is the motion vector estimated at site  $s$  (resp.,  $t$ ), and  $\text{dist}(s, t)$  is the Euclidean distance between nodes  $s$  and  $t$ .

The conditional probability density function  $p(d | f)$  is given by the definition of a global data fidelity term which models the error between the realization  $f$  and the observation  $d$ . It is defined by

$$p(d | f) = \exp \{-U_I(f, d)\}, \quad (7)$$

where  $U_I(f, d)$  models the global estimation error. It is defined by

$$U_I(f, d) = \sum_{s \in S} V_I(s, f_s), \quad (8)$$

$V_I(s, f_s)$  being a local correspondence measure to evaluate the matching between one node  $s$  at time  $t_0$  ( $s \in S$ ) and its corresponding voxel  $f_s$  at time  $t_1$ . It provides a data conformity term and, in such a way, a distance between the observation  $d$  (surface at time  $t_0$  and 3D image at time  $t_1$ ) and the estimated motion field given by  $f$ . For the analysis of correspondence between one node  $s$  and one voxel  $v$ , this term is defined by the following equation:

$$V_I(s, v) = \alpha_d \cdot E_{\text{dist}}(s, v) + \alpha_c \cdot E_{\text{contour}}(v) + \alpha_t \cdot E_{\text{topol}}(s, v), \quad (9)$$

where

$$\begin{aligned} E_{\text{dist}}(s, v) &= \text{dist}(s, v), \\ E_{\text{contour}}(v) &= C(v) = \begin{cases} 1 & \text{if } v \text{ belongs to a contour,} \\ 0 & \text{otherwise,} \end{cases} \end{aligned} \quad (10)$$

$$\begin{aligned} E_{\text{topol}}(s, v) &= \frac{1}{|\mu_s|} \sum_{i \in \mu_s} C((v_x, v_y, v_z)^t + (s_x, s_y, s_z)^t - (i_x, i_y, i_z)^t), \end{aligned} \quad (11)$$

with  $s$  is the considered node (of coordinates  $(s_x, s_y, s_z)^t$ );  $v$  is the considered voxel (of coordinates  $(v_x, v_y, v_z)^t$ );  $\text{dist}(\cdot)$  is the Euclidean distance function;  $C(\cdot)$  is the contour detection function (implemented by a Canny filtering);  $\mu_s$  is the neighborhood of the node  $s$ ;  $i$  is a neighboring node of  $s$  (of coordinates  $(i_x, i_y, i_z)^t$ ); and  $\alpha_c, \alpha_t, \alpha_d$  are weighting factors.

From (1), (4), and (7), we have

$$p(f | d) \propto \exp \{-U(f, d)\}, \quad (12)$$

with

$$U(f, d) = \sum_{s \in S} V_I(s, f_s) + \sum_{c \in C} V_R(c, f^c) \quad (13)$$

a global energy which is to minimize to obtain the most probable correspondences.

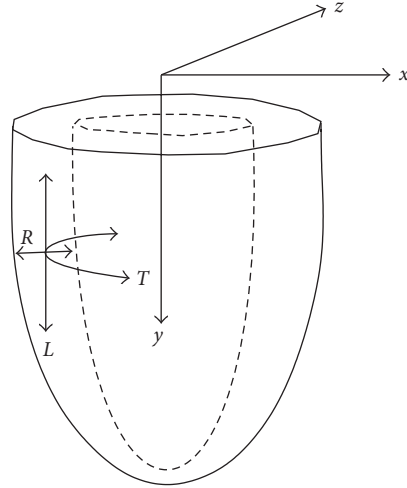


FIGURE 1: Cardiac motion components ( $L$ : longitudinal contraction,  $R$ : radial contraction,  $T$ : twisting).

## 2.2. Hierarchical scheme and optimization stage

The previously described motion extraction process is applied according to a hierarchical scheme which allows focusing the correspondence research area and reducing computing needs. This multiresolution scheme is considered to preserve local Markov property according to the high spatial resolution provided by MSCT data.

The surface mesh at time  $t_0$  and the volume at next time  $t_1$  are defined with decreasing scales as follows: each data set from upper resolution  $R_i$  ( $i = 1, \dots, n_l$ ,  $n_l$  being the number of used resolution levels) is restricted in space at a lower level scale  $R_{i-1}$  by the application of a mean filtering (or Gaussian filtering for the volume) and of a subsampling process in order to provide a regular mesh corresponding to volume voxel coordinates at the same level.

The matching process is first applied at the lowest resolution (with an initialization to a null motion) to guide the motion estimation with the coarsest details. The result of that first estimation is used as an initialization, after an interpolation step, for the correspondences computation at the next finer resolution. This motion extraction process is applied iteratively, with an adaptation of energy weighting coefficients, until the estimation is obtained at the desired resolution.

The global optimization of the correspondences is performed with a stochastic relaxation Metropolis algorithm combined with a simulated annealing process at the first lower-resolution level and with an iterated conditional mode (ICM) algorithm at the upper-resolution levels.

## 3. RESULTS

In a first part, the method has been applied on simulated data resulting from realistic deformations of a real ventricular shape. This first stage has provided the means to control and define the different parameters included in our approach. In a second part, the method has been applied on real

human cardiac data acquired with MSCT. Finally, the means to extract global and local parameters in association to informative visual representation modes have been developed.

### 3.1. Tests on simulated data

Numerical simulations have been used to test the motion extraction process between two successive instants. In the absence of translation motion induced by patient respiration (the MSCT acquisition is realized under one single breath-hold) the heart is submitted to three main kinds of motion: radial and longitudinal contraction/expansion and twisting (cf. Figure 1). To simulate data, these three kinds of motion are applied to a previously 3D extracted mesh (corresponding to the first instant of the sequence). These deformations result in the mesh corresponding to the second instant. Then, this deformed mesh is inserted into a volume preprocessed by a Canny filter followed by an endocardial suppression step. The hierarchical matching process is finally applied between the surface before deformation and this volume at three increasing scales.

Using this simulation process, the real correspondences are known. It enables measuring the error of matching of the proposed method and to study the evolution of the matching process along iterations and at each stage of the hierarchical process. The impact of the different parameters involved in the computation of the energies or in the optimization process, as well as meaningful information provided by scale refinement, can also be evaluated.

Different tests have been conducted and combined to find the optimal value for each parameter involved in the matching process. These values have shown a good unicity (tests running with these values on data generated with varied motion parameters have provided optimal results) and a good stability (moderate variations of these values do not affect the quality of the result).

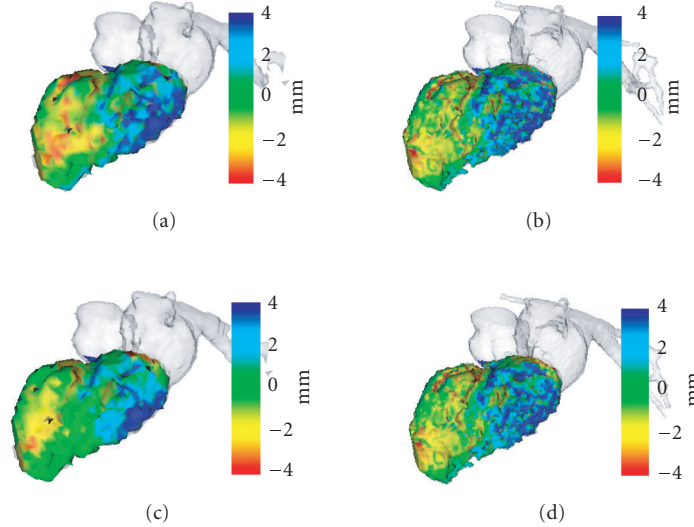


FIGURE 2: Simulated (a, b) and estimated (c, d) motion amplitudes with a left oblique anterior view at two resolutions (levels  $64^3$  (a, c) and  $128^3$  (b, d)) (colours: in blue (resp., red), motion directed outside (resp., inside) the cavity corresponding to positive (resp., negative) displacements), measures in millimeters.

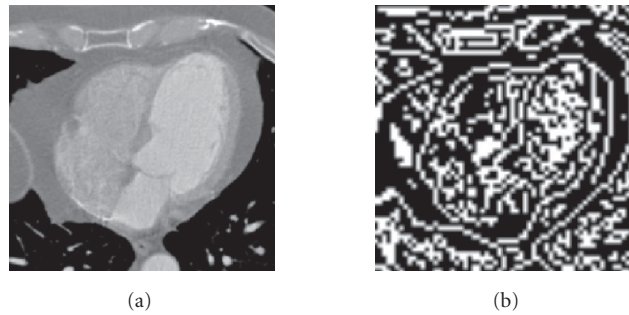


FIGURE 3: (a) One axial slice of one data volume of the sequence, (b) corresponding axial slice (at a lower resolution) after the Canny filtering process.

Figure 2 illustrates an example of results obtained at the two lowest-resolution levels ( $R_1$  with volume size  $64^3$  and  $R_2$  ( $128^3$ )). In color are represented the applied (a, b) and estimated (c, d) motion amplitudes. In red are represented the displacements directed inside the cavity, and in blue the displacements directed outside the cavity. With an initial mean matching error of 6.7 mm at  $R_1$  level, the process converges to a final mean error of 0.8 mm at  $R_3$  level. We have observed that this hierarchical process enables gaining in precision and error deviation.

These results have been confirmed by tests running with different simulated motion parameters.

### 3.2. Results on real data

The algorithm has been applied on real human heart data with a temporal database acquired by a Siemens SOMATOM Sensation 16 with ten volume images representing a whole

cardiac cycle. Each volume contains about 300 slices of  $512 \times 512$  pixels, giving a resolution for each voxel of  $0.35 \times 0.35 \times 0.5$  mm (cf. Figure 3(a) illustrating one CT axial slice).

The segmentation preprocess has been applied to the first volume of the sequence resulting in the extraction of the heart left cavities and of the beginning of the aorta. To obtain the surface mesh corresponding to time  $t_0$ , the segmented volume has been processed by the marching cubes algorithm (cf. Figure 4).

Using the optimal set of parameters found with the numerical simulations, the motion extraction process has been applied between this mesh (corresponding to time  $t_0$ ) and the volume corresponding to time  $t_1$  after a Canny operator application (cf. Figure 3(b) for an example of the Canny filter output). The algorithm has been iteratively applied to this dynamic sequence considering three resolution levels (from  $64^3$  to  $256^3$ ), providing a set of estimated surfaces and motion fields for each instant of the sequence.

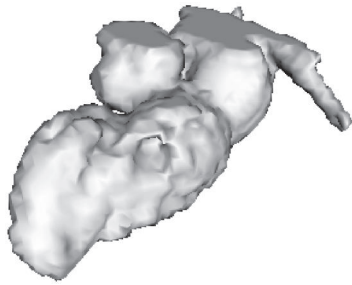


FIGURE 4: 3D surface of the extracted shape, corresponding to time  $t_0$ , represented at a lower resolution to highlight main structures.

Figure 5 illustrates results obtained at the two lowest levels at end-diastolic (a, b) and end-systolic (c, d) instants. The contraction movements (represented with red color or by negative displacements), characteristic of systole, are as well identified as the expansion movements (represented with blue color or by positive displacements) and are coherent with cardiac phases. We can see that the lowest level representation is meaningful and that the displacements obtained at upper levels provide the means to extract local clinical parameters at various scales.

Figure 6 shows the estimated motion amplitude during the whole cardiac cycle and using the highest resolution. We can observe that movements extracted on the whole sequence are coherent with cardiac phases. We can particularly remark the progressive expansion of the ventricle, from its basis to the apex, during the ventricle diastole (Figures 6(b)–6(f)), the important expansion occurring during the end-diastolic phase (Figure 6(f)), and the spatial evolution of contraction during the ventricle systole (Figures 6(g), 6(h)).

This kind of representations enables to highlight functional abnormalities. For instance, Figure 6 highlights the pathological situation where the antero-apical area (bottom left part of the visualized shape) suffers from akinesia.

### 3.3. Extraction of clinical parameters

Firstly, the extraction of global parameters of the ventricular function has been researched. After the interactive selection of three points determining the valvular plane, the 3D detected structure is limited to the left endocardium. Then, the ventricular volume can be computed for each instant, providing the curve of 3D volume variations along the entire temporal sequence analyzed. These measures give access to clinical functional features such as systolic volume or ejection fraction (EF). However, because the proposed method subtracts trabeculas from the cavity volume, the measured volumes are lower than the volumes measured by a rough approximation of the endocardium. Obtained ejection fraction is therefore overestimated compared to those obtained by more classical methods (for one case, e.g., 55% was measured with echocardiography against 66% with our method).

Secondly, the extraction and representation of local parameters have been conducted. The anatomical system of reference, defined according to the great axis of the left ventricle, is computed from the patient specific 3D estimated surfaces. In this reference system, the detected movement is then decomposed in longitudinal, radial, and rotational motion components (cf. Figure 1). Cranial/caudal motion as well as inward and outward motion or wall twisting can therefore be measured. These motion components can then be analyzed along the temporal sequence, for a set of points selected on different anatomical parts of the ventricle (cf. Figures 7, 8). For this database, the extraction of radial movements show for example that the base of the heart verifies the largest motion amplitude (in contraction (negative values) and in expansion (positive values)) compared to the mid-cavity and to the apex. By the same way, movements of torsion can be locally enhanced and compared between different parts of the muscle. This kind of representation is of great interest for the clinical part because it allows to quantify how each type of movement (radial, longitudinal, torsion) is affected by specific pathologies.

A synthetic representation of local parameters has been also developed, based on the bull-eye representation, commonly used in echocardiography and MRI [33]. This kind of visualization is based on the anatomical segmentation of the 3D left ventricle in longitudinal and radial sectors and on their integration in a bull-eye scheme. The anatomical segmentation of the 3D surface is here conducted from the interactive selection of three points corresponding to the aortic and tricuspid valves and of the apex. For illustration, Figure 9 shows this anatomical segmentation and the motion amplitude estimated on the overall temporal sequence represented on the bull-eye scheme. This visual representation gives access to the dynamic behavior of each anatomical segment (on the whole sequence or between successive times). It allows to enhance and quantify pathological situations such as akinesia or asynchronism. The results observed on these real data show, for example, a reduced motion in apical septal segments (numbered 7, 8, 13, 14, and 17) which corresponds to the real pathological situation.

## 4. CONCLUSION

A new solution of motion extraction combined with surface estimation has been introduced and applied to the left ventricle in 4D cardiac MSCT imaging. It is based on a hierarchical surface-volume feature matching method formulated with a Markov random field and provides, with one unique process, the left cavity surfaces and associated 3D motion vector fields. The algorithm has been tested with simulated and real MSCT dynamic data, highlighting the great potential of MSCT imaging for quantitative clinical measure assessment in cardiac applications. Moreover these performances might be increased with new MSCT systems, combining more detectors (64 rows, or even 128 rows systems) and faster rotations. Indeed, with shorter acquisitions, the acquired data will be less submitted to artefacts, enabling to reconstruct more data volume by retrospective ECG-gating, providing

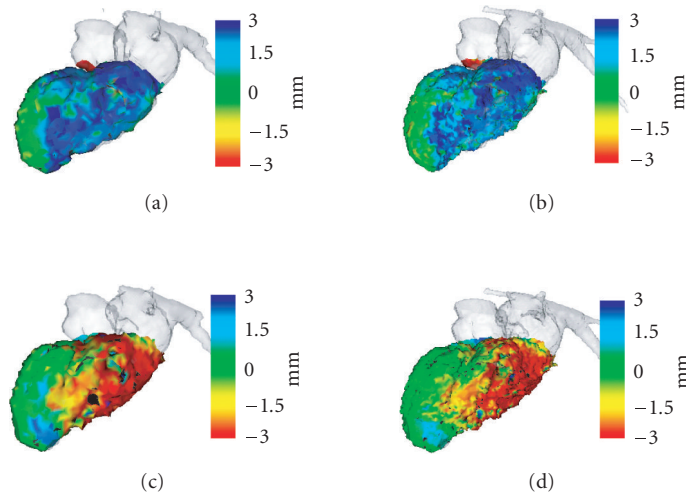


FIGURE 5: Estimated motion amplitude at end-diastolic (a, b) and end-systolic (c, d) instants, at two resolutions (levels  $64^3$  (a, c) and  $128^3$  (b, d)) (colours: in blue (resp., red), motion directed outside (resp., inside) the cavity corresponding to positive (resp., negative) displacements).

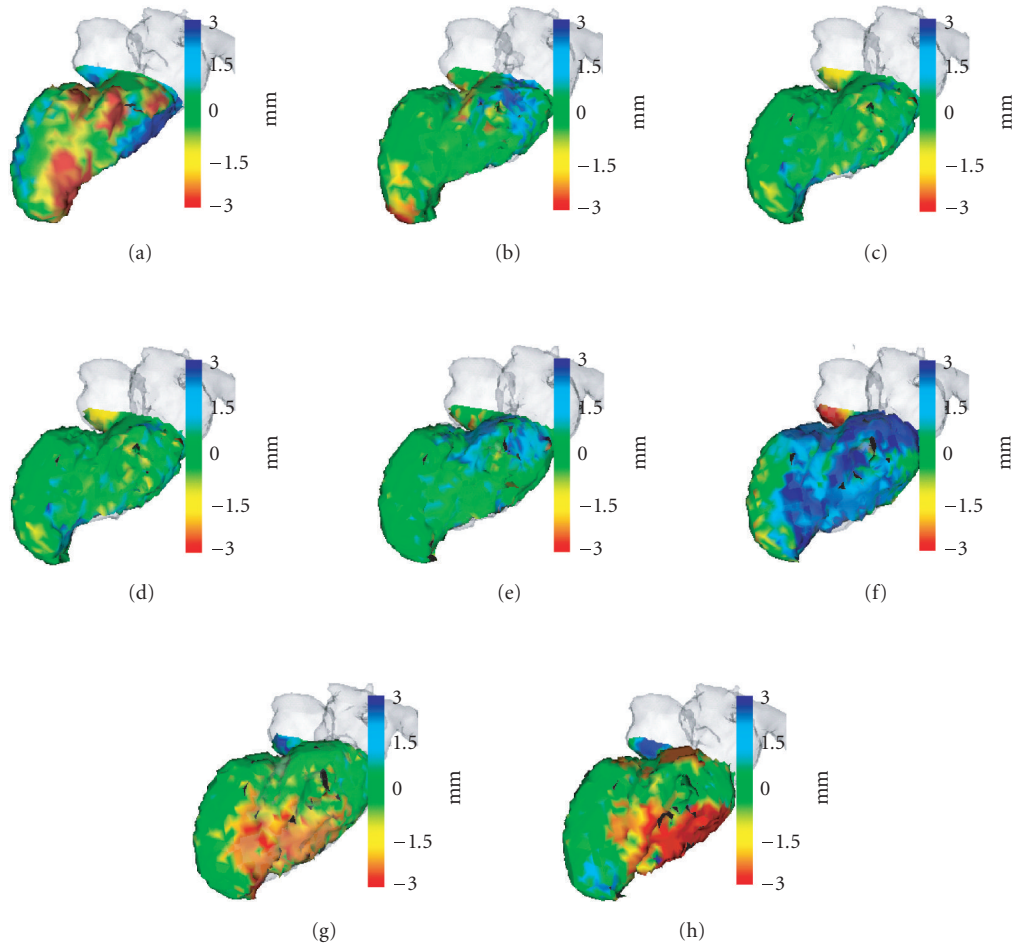


FIGURE 6: Estimated motion amplitude during the whole cardiac cycle. Time instants illustrated from (b)–(f) correspond to the ventricle diastole, while time instants from (g)–(a) correspond to the ventricle systole (colours: in blue (resp., red), motion directed outside (resp., inside) the cavity corresponding to positive (resp., negative) displacements).

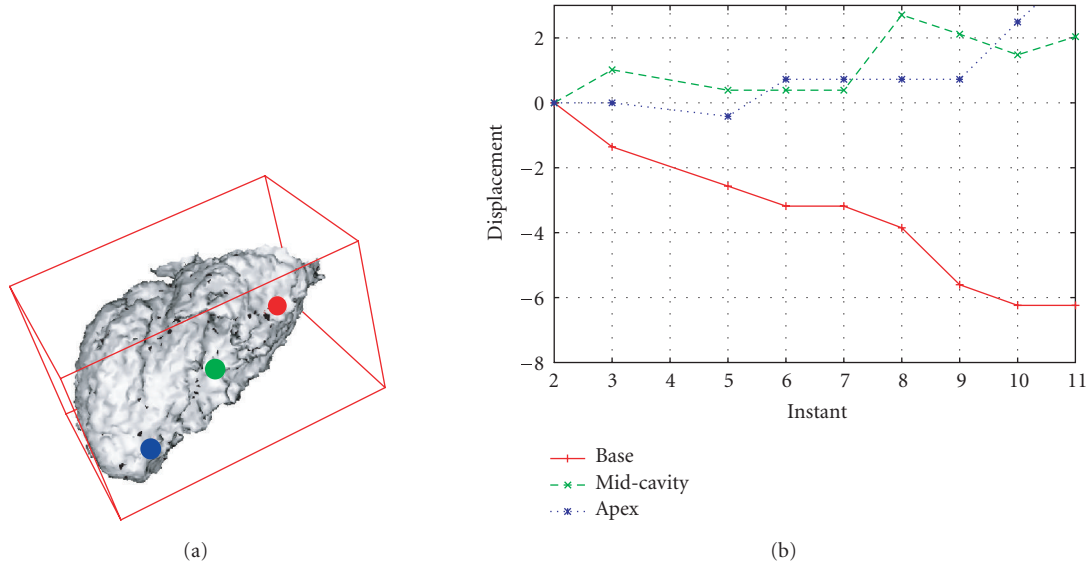


FIGURE 7: Longitudinal motion of three points interactively selected (base, mid-cavity, apex).

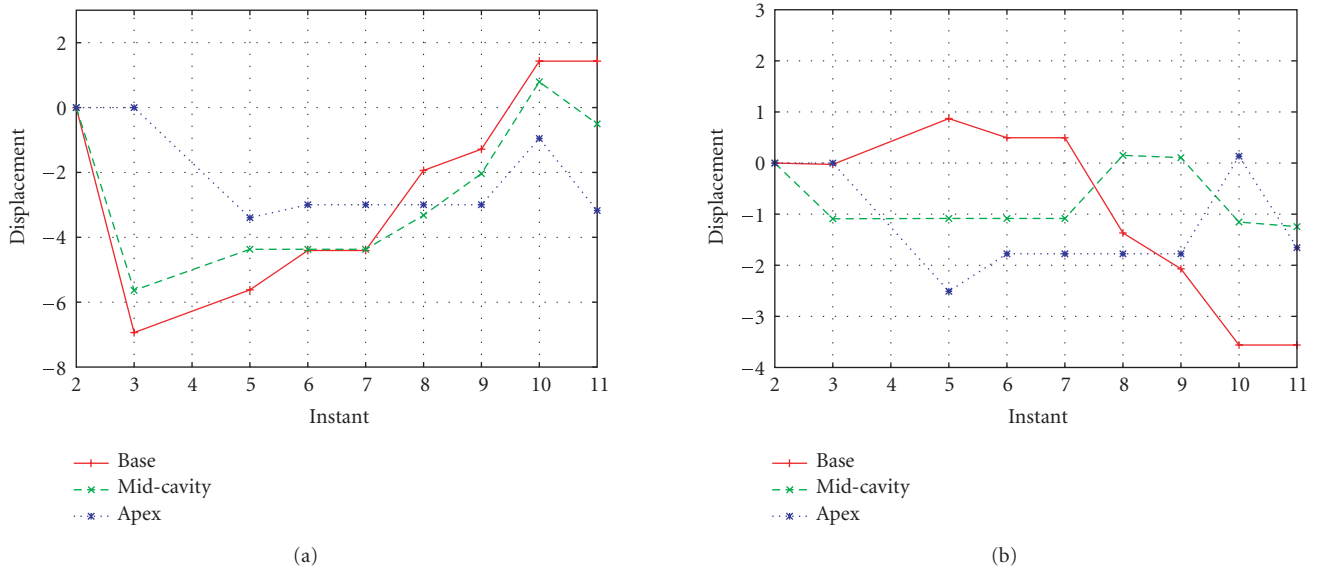


FIGURE 8: Radial and tangent motions of the three points represented in Figure 7.

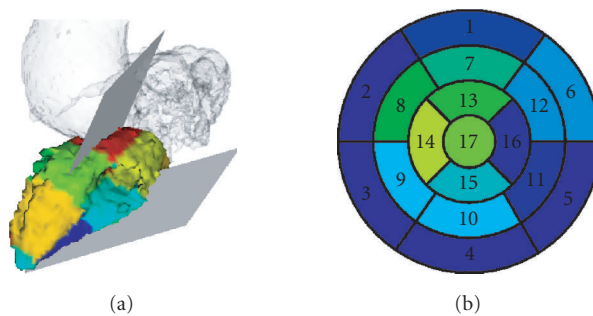


FIGURE 9: (a) Anatomical segmentation; (b) bull-eye representation of the estimated motion amplitude.

sequences of higher temporal resolution. Also, these new systems will be less sensitive to irregular heart rates. Further works will carry on extensive evaluation with normal and pathological real data, including especially a comparison with motion estimated with other imaging modalities.

## ACKNOWLEDGMENTS

This work is supported by Brittany region and the French Medical Research and Health National Institute (INSERM). The authors express their thanks to Siemens Medical Division, France, for having provided us real MSCT image data.

## REFERENCES

- [1] P. Shi, A. J. Sinusas, R. T. Constable, E. T. Ritman, and J. S. Duncan, "Point-tracked quantitative analysis of left ventricular surface motion from 3-D image sequences," *IEEE Transactions on Medical Imaging*, vol. 19, no. 1, pp. 36–50, 2000.
- [2] J. L. Prince and E. R. McVeigh, "Motion estimation from tagged MR image sequences," *IEEE Transactions on Medical Imaging*, vol. 11, no. 2, pp. 238–249, 1992.
- [3] J. Park, D. Metaxas, and L. Axel, "Analysis of left ventricular wall motion based on volumetric deformable models and MRI-SPAMM," *Medical Image Analysis*, vol. 1, no. 1, pp. 53–71, 1996.
- [4] P. Clarysse, M. Han, P. Croisille, and I. E. Magnin, "Exploratory analysis of the spatio-temporal deformation of the myocardium during systole from tagged MRI," *IEEE Transactions on Biomedical Engineering*, vol. 49, no. 11, pp. 1328–1339, 2002.
- [5] F. G. Meyer, R. T. Constable, A. J. Sinusas, and J. S. Duncan, "Tracking myocardial deformation using phase contrast MR velocity fields: a stochastic approach," *IEEE Transactions on Medical Imaging*, vol. 15, no. 4, pp. 453–465, 1996.
- [6] X. Papademetris, A. J. Sinusas, D. P. Dione, and J. S. Duncan, "Estimation of 3D left ventricular deformation from echocardiography," *Medical Image Analysis*, vol. 5, no. 1, pp. 17–28, 2001.
- [7] W. Yu, N. Lin, P. Yan, et al., "Motion analysis of 3D ultrasound texture patterns," in *Proceedings of 2nd International Workshop on Functional Imaging and Modeling of the Heart (FIMH '03)*, pp. 252–261, Lyon, France, June 2003.
- [8] G. Germano, J. Erel, H. Lewin, P. B. Kavanagh, and D. S. Berman, "Automatic quantitation of regional myocardial wall motion and thickening from gated technetium-99m sestamibi myocardial perfusion single-photon emission computed tomography," *Journal of the American College of Cardiology*, vol. 30, no. 5, pp. 1360–1367, 1997.
- [9] T. R. Miller, J. W. Wallis, B. R. Landy, R. J. Gropler, and C. L. Sabharwal, "Measurement of global and regional left ventricular function by cardiac PET," *Journal of Nuclear Medicine*, vol. 35, no. 6, pp. 999–1005, 1994.
- [10] S. Benayoun and N. Ayache, "Dense non-rigid motion estimation in sequences of medical images using differential constraints," *International Journal of Computer Vision*, vol. 26, no. 1, pp. 25–40, 1998.
- [11] J.-M. Gorce, D. Friboulet, and I. E. Magnin, "Estimation of three-dimensional cardiac velocity fields: assessment of a differential method and application to three-dimensional CT data," *Medical Image Analysis*, vol. 1, no. 3, pp. 245–261, 1997.
- [12] C. D. Eusemann, E. L. Ritman, and R. A. Robb, "Parametric visualization methods for the quantitative assessment of myocardial motion," *Academic Radiology*, vol. 10, no. 1, pp. 66–76, 2003.
- [13] A. F. Frangi, W. J. Niessen, and M. A. Viergever, "Three-dimensional modeling for functional analysis of cardiac images: a review," *IEEE Transactions on Medical Imaging*, vol. 20, no. 1, pp. 2–25, 2001.
- [14] S. Schroeder, A. F. Kopp, B. Ohnesorge, et al., "Accuracy and reliability of quantitative measurements in coronary arteries by multi-slice computed tomography: experimental and initial clinical results," *Clinical Radiology*, vol. 56, no. 6, pp. 466–474, 2001.
- [15] A. Larralde, C. Boldak, M. Garreau, C. Toumoulin, D. Boulmier, and Y. Rolland, "Evaluation of a 3D segmentation software for the coronary characterization in multi-slice computed tomography," in *Proceedings of 2nd International Workshop on Functional Imaging and Modeling of the Heart (FIMH '03)*, vol. 2674 of *Lecture Notes in Computer Science*, pp. 39–51, Lyon, France, June 2003.
- [16] M. Garreau, A. Simon, D. Boulmier, and H. Guillaume, "Cardiac motion extraction in multislice computed tomography by using a 3D hierarchical surface matching process," in *Proceedings of IEEE Computers in Cardiology (CinC '04)*, pp. 549–552, Chicago, Ill, USA, September 2004.
- [17] C. W. Chen, T. S. Huang, and M. Arrott, "Modeling, analysis, and visualization of left ventricle shape and motion by hierarchical decomposition," *IEEE Transactions on Pattern Analysis and Machine Intelligence*, vol. 16, no. 4, pp. 342–356, 1994.
- [18] E. Bardinet, L. D. Cohen, and N. Ayache, "A parametric deformable model to fit unstructured 3D data," *Computer Vision and Image Understanding*, vol. 71, no. 1, pp. 39–54, 1998.
- [19] W.-C. Huang and D. B. Goldgof, "Adaptive-size meshes for rigid and nonrigid shape analysis and synthesis," *IEEE Transactions on Pattern Analysis and Machine Intelligence*, vol. 15, no. 6, pp. 611–616, 1993.
- [20] I. Cohen, N. Ayache, and P. Sulger, "Tracking points on deformable objects using curvature information," in *Proceedings of the 2nd European Conference on Computer Vision (ECCV '92)*, pp. 458–466, Santa Margherita Ligure, Italy, May 1992.
- [21] S. M. Song and R. M. Leahy, "Computation of 3-D velocity fields from 3-D cine CT images of a human heart," *IEEE Transactions on Medical Imaging*, vol. 10, no. 3, pp. 295–306, 1991.
- [22] P. Hellier, C. Barillot, E. Mémin, and P. Pérez, "Hierarchical estimation of a dense deformation field for 3-D robust registration," *IEEE Transactions on Medical Imaging*, vol. 20, no. 5, pp. 388–402, 2001.
- [23] A. A. Amini and J. S. Duncan, "Bending and stretching models for LV wall motion analysis from curves and surfaces," *Image and Vision Computing*, vol. 10, no. 6, pp. 418–430, 1992.
- [24] C. Kambhamettu, D. B. Goldgof, M. He, and P. Laskov, "3D nonrigid motion analysis under small deformations," *Image and Vision Computing*, vol. 21, no. 3, pp. 229–245, 2003.
- [25] A. Simon, M. Garreau, D. Boulmier, J.-L. Coatrieux, and H. Le Breton, "A surface-volume matching process using a Markov random field model for cardiac motion extraction in MSCT imaging," in *Proceedings of 3rd International Workshop on Functional Imaging and Modeling of the Heart (FIMH '05)*, pp. 457–466, Barcelona, Spain, June 2005.
- [26] S. Z. Li, *Markov Random Field Modeling in Computer Vision*, Springer Computer Science Workbench Series, Springer, London, UK, 1995.

- [27] P. Pérez, "Markov random fields and images," *CWI Quarterly*, vol. 11, no. 4, pp. 413–437, 1998.
- [28] R. Fablet and P. Boutheymy, "Motion recognition using non-parametric image motion models estimated from temporal and multiscale co-occurrence statistics," *IEEE Transactions on Pattern Analysis and Machine Intelligence*, vol. 25, no. 12, pp. 1619–1624, 2003.
- [29] C. Kervrann and F. Heitz, "Statistical deformable model-based segmentation of image motion," *IEEE Transactions on Image Processing*, vol. 8, no. 4, pp. 583–588, 1999.
- [30] M. Mignotte, J. Meunier, and J.-C. Tardif, "Endocardial boundary estimation and tracking in echocardiographic images using deformable templates and Markov random fields," *Pattern Analysis & Applications*, vol. 4, no. 4, pp. 256–271, 2001.
- [31] H. Guillaume and M. Garreau, "Segmentation de cavités cardiaques en imagerie scanner multi-barettes," in *Forum des Jeunes Chercheurs en Génie Biologique et Médical*, pp. 92–93, Nantes, France, May 2003.
- [32] J. Besag, "Spatial interaction and the statistical analysis of lattice systems," *Journal of the Royal Statistical Society. Series B*, vol. 36, no. 2, pp. 192–236, 1974.
- [33] M. D. Cerqueira, N. J. Weissman, V. Dilsizian, et al., "Standardized myocardial segmentation and nomenclature for tomographic imaging of the heart," *Circulation*, vol. 105, no. 4, pp. 539–542, 2002.

**Mireille Garreau** was born in 1962. She received her M.S. degree in signal processing and telecommunications from the University of Rennes 1 in 1985. She obtained a Ph.D. degree in signal and image processing and telecommunications from the University of Rennes1 in 1988. She has been working as an Associate Professor since 1989 and as a Professor since 2004. She has been involved in biomedical engineering for about



15 years. Her main research topics are related to the joint use of biomedical knowledge engineering (or artificial intelligence in medicine) and image analysis (generic methods going from calibration to segmentation, from 3D reconstruction to motion estimation and image understanding) with applications to vascular and cardiac imaging. She is the Head of the ACTIVE project (tissue analysis and characterization in vascular imaging) in the LTSI (joint research laboratory of INSERM and University of Rennes1, France).

**Antoine Simon** was born in 1978 in Brest, France. He graduated from the Ecole Supérieure de l'Ouest (ESEO) in 2002 and received the M.S. degree in image and signal processing in biology and medicine from the Faculty of Medicine, Angers. He then joined the Laboratory of Signal and Image Processing (LTSI, U642 INSERM, University of Rennes1, France) where he obtained a Ph.D. degree in 2005. His main research interests are related to cardiac imaging, motion extraction, characterization and representation, and multiresolution image processing.



**Dominique Boulmier** was born in 1968. He joined the Rennes University of Medicine between 1986 and 1994. He was a Fellow in cardiology between 1994 and 2000 and an Assistant Professor between 2000 and 2003. He has been working since then as an interventional cardiologist at the Rennes University Hospital (Bretagne). He is involved in clinical research on cardiac imaging with computed tomography.



**Jean-Louis Coatrieux** received the degree in electrical engineering from the Polytechnic Institute, Grenoble, France, in 1970 and the Ph.D. and State Doctorate degrees in sciences in 1973 and 1983, respectively, from the University of Rennes 1, France. He was an Assistant Professor from 1970 to 1975 and an Associate Professor from 1976 to 1986 at the Institute of Technology of Rennes. Since 1986, he has been the Director of Research at the National Institute for Health and Medical Research (INSERM), France, and since 1993 has been a Professor at the New Jersey Institute of Technology, Newark. He has been the Head of the Laboratoire Traitement du Signal et de l'Image, INSERM, up to 2003 and in charge of the National Research Program in Health Technology at the Ministry of Research (1998–2001), France. He was President of the joint Committee CNRS-INSERM in this area (2001–2003). His experience is related to 3D images, signal processing, computational modeling, and complex systems with applications in integrative biomedicine. He has served as the Editor-in-Chief of the *IEEE Transactions on Biomedical Engineering* (1996–2000). He has received several awards from IEEE (EMBS Service Award, 1999, and the Third Millennium Award, 2000) and he is Doctor Honoris Causa from the University of Nanjing, China.



**Hervé Le Breton** was born in 1959. He went to the Rouen University of Medicine between 1978 and 1984. He was a Fellow in cardiology from 1984 to 1988 and has been working as an interventional cardiologist from 1989 at the Rennes University Hospital (Bretagne). He spent one year at the Cleveland Clinic Foundation in 1994–1995 doing animal research (role of antiplatelet agents in restenosis post PTCA). He was nominated Professor of Medicine in 1999. His main research concerns are in coronary artery disease and the field of interventional cardiology.

